Demonstration of a CNOT Gate using Electromagnetically Induced Transparency

Katie McDonnell

Abstract

This thesis demonstrates a CNOT gate realised using electromagnetically induced transparency (EIT) which relies on the strong long-range interactions between Rydberg atoms. The CNOT gate is achieved on a microsecond time scale and robustly implements a conditional transfer between the two qubit states of a target atom that is solely dependent on the initial qubit state of a control atom. This method has the potential to be scaled to a target ensemble without typical $\sqrt{N}$ scaling.

The experiment presented is a cold atom system with two caesium atoms trapped in optical tweezers at a separation of 5 μm. The hyperfine ground states of the caesium atoms are utilised as qubit states with optical pumping ensuring the atoms are prepared in the correct state $|F = 4, m_F = 0\rangle$. Coherent control between the hyperfine ground states is achieved using microwaves and excitation lasers, and excitation to the Rydberg state $\left|81D_{5/2}, m_j = 5/2\right\rangle$ is achieved by two-photon excitation from lasers locked to a high-finesse ultra-low-expansion (ULE) cavity.

This thesis details the optimisation steps taken in the experiment to demonstrate the CNOT gate, including experiment upgrades, and how the CNOT gate is used to prepare the maximally entangled Bell state $|\Phi^+\rangle$. We detail how the Bell state is probed using parity oscillations to verify the quantum nature of the CNOT gate. We achieve a loss corrected CNOT gate fidelity of $\mathcal{F}_{\text{CNOT}} \geq 0.82(2)$, measure the Bell state fidelity $\mathcal{F}_{|\Phi^+\rangle} \geq 0.66(3)$ and finally present a number of technical improvements to advance this to a level required for fault-tolerant scaling.

Demonstration of a CNOT Gate using Electromagnetically Induced Transparency

Katie McDonnell

A thesis submitted in partial fulfilment
of the requirements for the degree of
Doctor of Philosophy

Department of Physics
University of Strathclyde

October 6, 2021

Contents

List of Figures

List of Tables

Declaration

I confirm that no part of the material offered has previously been submitted by myself for a degree in this or any other University. Where material has been generated through joint work, the work of others has been indicated.

Katie McDonnell
Glasgow, October 6, 2021

The copyright of this thesis rests with the author. No quotation from it should be published without their prior written consent and information derived from it should be acknowledged.

Acknowledgements

I would like to start by thanking my supervisors Jonathan Pritchard and John Jeffers for giving me the opportunity to participate in the project. They have provided me with the opportunities and support to explore realms beyond the lab for which I am very grateful. In particular I would like the thank Jonathan for guiding me through this ambitious project and his support in the experiement. His feedback, encouragement and seemingly endless knowledge have been invaluable.

Thanks also go to Craig Picken and Rémy Legaie for introducing me to all the lab quirks before they left and for guiding me through the first year of my PhD. Thanks also to Lindsey Keary for sharing the lab, the frustrations when things go wrong and celebrating when things go well and, to Hao (Jack) Yang for laughing with me when things seemed so ridiculous. Many thanks go to the EQOP group whose collective love of plants and eggs will be remembered fondly. I have truly enjoyed the time I have spent working as part of this group and will miss working here.

Finally, I would like to thank my Mum and Dad for always supporting and encouraging me in all that I do, Kevin for always being there to listen and to keep me grounded and, Chris for your endless support, encouragement and sense of adventure. Thank you for reminding me to smile and just keep swimming.

Part I

Introduction

Chapter 1

Introduction

The computer and its processing capabilities have given us technological advancements beyond measure, and yet there are limitations to what even the best supercomputers of the day can achieve. Since quantum mechanics came to light in the early twentieth century many proposals have been made to utilise quantum systems to develop technologies based on phenomena at the quantum level. Over the last twenty years tremendous progress has been made in developing quantum technologies in both academic settings and in industry, with programmes such as the UK National Quantum Technologies programme [1] providing a route between the two. One area of significant interest is quantum information processing (QIP) with large investment from companies like IMB [2], Google [3] and Honeywell [4].

There are limitations to what a classical computer can do, for example simulating a system of interacting molecules or materials, optimisation problems ranging from logistics (e.g. route planning and traffic management) to recommendations made to a user by a streaming service, and factorisation for cryptography are all hard problems which classical computers struggle to solve optimally [5]. The problem is the algorithms needed to simulate these types of systems require an exponential scaling of resources and take an increasingly long time to solve. This is where quantum computing offers an advantage [6–10], where proposals like Grover's search algorithm [11] reduce the average number of checks a computer would need to make

from $N/2$ to $\sqrt{N}$, thus reducing the time taken to find the solution, whilst exponentially large Hilbert spaces on quantum computers are ideal for combinatoric optimisation problems [12].

Another proposal made by Richard Feynman [13] says that to simulate a complex quantum mechanical system a quantum system should be used. In other words, to simulate an unknown quantum system we can use a controllable quantum system with well-known parameters to model the complex dynamics of the system of interest. One such example is using trapped atoms addressed by lasers to explore topological quantum matter [14]. In general quantum simulation would find applications in the field of advanced material science and pharmaceuticals [15, 16].

There are many parties developing quantum technologies, including quantum simulation and quantum computing. The main focus of this thesis is on developing hardware for use in neutral atom quantum information processing.

1.1 Quantum Information Processing

The idea behind quantum information processing (QIP) is to prepare a set of quantum objects in a well-defined quantum state and transform the state through controlled interactions, to overcome the limitations of classical devices. There are two main types of quantum computing: *analog* quantum computing where a physical system is used to mimic another quantum system of interest by reproducing its Hamiltonian as closely as possible, and *digital* quantum computing where the quantum state of the target system is encoded in a quantum register and a sequence of programmable quantum gates is applied to simulate the time evolution of the system [17].

Examples of quantum objects are atoms, ions, photons and superconductors that can each be used to define a quantum bit or *qubit* which is the primary building block of a quantum computer. A sequence of operations or gates can be applied to the qubits using lasers, microwaves or electrical signals to transform the quantum

state of the qubit. Qubits and quantum gates will be discussed in detail in Chapter 2. In order to quantify the requirements for achieving quantum computation, DiVincenzo [18] outlined a list of conditions that need to be satisfied. These are

- a scalable physical system with well-characterised qubits,
- the ability to initialise the qubit in a given quantum state,
- long coherence times - much longer than the gate operation time,
- a universal set of quantum gates, and
- there must exist a method to measure the state of each individual qubit.

This list is used as a check list when considering physical approaches to quantum computation [19].

There are many proposals and indeed implementations of quantum computation based on platforms such as NMR [20, 21], trapped ions [22, 23], superconductors [24], photonic systems [25, 26], and neutral atoms [17, 27]. Each platform has its benefits and limitations, for example trapped ions have long coherence times but slow gates, superconducting qubits have fast gates but short coherence times and neutral atoms offer long coherence times but relatively slow gates [28, 29]. Currently the best high-fidelity quantum logic gates have been achieved using trapped ions and superconducting qubits, with two-qubit gate fidelities $F > 0.999$ for ions [22, 23] and $F > 0.997$ for superconducting systems [24]. The focus of this thesis is on neutral atoms which is an attractive platform for ease of control and scaling with recent results demonstrated on neutral atoms being competitive with the ion and superconducting systems [30].

1.2 Neutral Atom QIP

Neutral atoms are an exciting platform for quantum computing and were first proposed by Jaksch *et al.* [31] and Lukin *et al.* [32]. It was proposed to encode

quantum information on the long-lived hyperfine ground states of single atoms or in collective excitations of atomic ensembles and use highly excited Rydberg states to mediate interactions between the them. The advantage of atoms over other platforms is scalability as many identical qubits are guaranteed as there is no fabrication processes involved and, there are well established techniques to trap and manipulate large numbers of atomic qubits [33].

Microscopic arrays of dipole traps or optical lattices are used to trap atomic qubits. The limitation of trapping atoms in this way is that they are stochastically loaded so that the arrangement of the atoms is random. This limitation has been overcome by using reconfigurable arrays of atoms that use an acousto-optic deflector (AOD) or a spatial light modulator (SLM) to give dynamical control of the atoms so that arbitrary geometries can be realised in 1D [34], 2D [35] and 3D [36]. Recently arrays of > 200 qubits have been realised and manipulated to demonstrate the potential use in quantum simulation [14, 37–39].

Interactions between neutral atoms in the ground state separated by ~ 1 μm are weak and cannot be used directly to perform quantum gates without intervention [40]. One method that has been demonstrated is exploiting spin-exchange by overlapping pairs of optical tweezers to generate entanglement [41]. Another approach is the one relevant to this thesis which is to use neutral atoms excited to Rydberg states [5, 17, 19, 33, 40].

1.3 Rydberg Atom QIP

Rydberg atoms are atoms that have been excited to a state with a high principal quantum number n [42]. The result of this is an atom with a large orbital radius which leads to exaggerated properties such as a dipole moment that scales $\propto n^2$. The large dipole moment gives rise to an effect called dipole blockade causing atoms in a Rydberg state to experience an energy shift that prevents the excitation of more than one atom to the Rydberg state. The Rydberg blockade only effects

atoms within a distance known as the blockade radius which is typically ~ 10 μm allowing deterministic quantum operations to be performed over these distances. Rydberg atoms also have long radiative lifetimes on the order of 100's μs which far exceeds the typical timescale of gate operations [5].

For N atoms within the Rydberg blockade radius, each atom is equally likely to be excited to the Rydberg state such that an entangled symmetric state can be created between the ground and singly excited Rydberg state, which exhibits a collectively enhanced Rabi frequency $\Omega_N = \sqrt{N}\Omega$ [32]. Generating an entangled state using Rydberg blockade has been demonstrated by many groups using alkali atoms [30, 43–46], including our own [47]. Early experiments were limited to $F \sim 0.82$ due to technical noise, with the dominant error arising from laser phase noise [45, 48] despite Rydberg systems offering intrinsic fidelities of $F \sim 0.999$ [19, 40].

Recent results have demonstrated suppression of this technical laser noise to enable significant improvements in fidelity, reaching single and two-qubit fidelities of $F \geq 0.97$ [45] and demonstrating a three-qubit Toffoli gate with $F \geq 0.87$ [30]. Further improvements have been obtained using alkali-earth atoms, which offer long-lived optical qubit states to reach $F \geq 0.991$ [49]. These gate fidelities are competitive against typical superconducting systems, and combined with the scalability of neutral atoms make them a highly attractive candidate for developing quantum computers able to tackle real-world problems.

For blockaded gates of $N > 2$ atoms, collective effects lead to a $\sqrt{N}$ scaling in pulse area for creating a single collective excitation [50]. If N is unknown or fluctuates (e.g. Poisson loading of an atomic ensemble) high fidelity gates are challenging [32, 51]. One method to circumvent the $\sqrt{N}$ scaling was proposed by Müller *et al.* [52] using electromagnetically induced transparency (EIT).

This protocol provides a scalable approach to performing entanglement of large atomic ensembles using a single control atom whilst circumventing the challenges of the collective Rabi frequency. The resulting CNOT^N gate is robust against number

fluctuations and acts as a single-atom transistor to amplify the quantum state of an atom onto an atomic ensemble. This approach provides, a route to creating useful entangled states for quantum information processing (QIP), high precision measurements beyond the standard quantum limit [53], and to demonstrate the crucial gate scheme for implementing surface codes in atomic arrays [54].

1.4 Hybrid System

Achieving a high-fidelity universal set of gates on a scalable platform is a real challenge as each qubit technology has its own strengths and weaknesses. One solution is to create a hybrid system that benefits from the strengths of one platform while overcoming the weaknesses of another. An example of this is to combine neutral atoms and superconducting circuits to gain the long coherence and lifetimes offered by the neutral atoms in their ground states and the fast gates offered by superconductor qubits [55–57].

Using the atoms as a quantum memory allows us to take advantage of the long coherence times of the hyperfine ground states. Then utilising Rydberg states where interactions between atoms and between neighbouring Rydberg states occur in the microwave regime, facilitates strong coupling to superconducting circuits [55, 58]. Combining these means that long-range entanglement could be achieved over mm length scales by entangling atoms trapped at different anti-nodes with the microwave cavity field [59].

Pioneering work by S. Haroche has shown that is is possible to couple beams of Rydberg atoms to high-Q microwave cavities [60, 61]. Further to this hybrid systems composed of Rydberg atoms and a co-planar microwave waveguide (CPW) have demonstrated cavity driven Rabi oscillations between between a pair of Rydberg states driven by the microwave field of the CPW [56, 62]. A hybrid device of this type could be used for applications such as microwave-to-optical conversion [63], cavity cooling [64] and scalable long-range interactions between atomic

ensembles [59].

1.5 Thesis Outline

This thesis is separated into five parts: Part I introduces the concept of quantum information processing using neutral atoms and introduces Rydberg states discussing how these can be used to demonstrate quantum gates. Part II covers the theory of atom-light interactions, highlights the main properties of Rydberg atoms and outlines a method to realise a CNOT gate. Part III details the main experimental set-up for trapping and detecting two caesium atoms in a well-prepared state. Part IV presents the experimental demonstration of single qubit and two-qubit gates and Part V forms a conclusion of the presented work and outlines future upgrades to the experiment.

The chapter breakdown is as follows;

Part I: Introduction

- Chapter 2 extends the discussion in this introduction to describe in detail qubits and quantum logic gates, and ways to measure the quantum nature of the qubit states.

Part II: Atom-Light Interactions

- Chapter 3 considers the case of a two-level atom interacting with mono-chromatic light and introduces key results that will be used throughout the thesis.
- Chapter 4 extends the discussion to a three-level atom, describing the different configurations for the interaction with a mono-chromatic light source and discuss how electromagnetically induced transparency (EIT) arises from the interaction.

- Chapter 5 gives a brief introduction to Rydberg atoms and their properties. In particular we discuss the dipole-dipole interactions between Rydberg atoms and how this leads to dipole blockade.

- Chapter 6 outlines a protocol to perform a scalable CNOT^N gate detailing the process and presents simulations to optimise the experimental implementation with expected fidelity.

Part III: Experiment

- Chapter 7 describes the main experiment set-up used to perform the quantum gates. This includes laser cooling and trapping and single trapping and imaging.

- Chapter 8 describes the procedure for hyperfine state discrimination and optical pumping. It also gives a comparison of the effectiveness of optical pumping using the D_1 and D_2 lines of caesium.

- Chapter 9 describes the laser systems used to perform rotations on the atoms, including the experimental upgrades of an optical phase-lock between two lasers, the installation of a new Rydberg laser and the installation of a microwave antenna.

Part IV: Single and Two-Qubit Operations

- Chapter 10 describes the optimisation of single qubit rotations between the hyperfine ground states using both laser and microwave pulses, and a comparison of Rydberg excitations driven using the new and previous Rydberg lasers is made.

- Chapter 11 describes the experiment optimisation that enabled us to perform a CNOT gate. Firstly, EIT is demonstrated, then two state preparation techniques are discussed and compared to find the optimal experimental setting for performing the CNOT gate. The novel protocol is used to demonstrate

a CNOT gate in the experiment and then used prepare and measure a Bell state.

Part V: Conclusions and Outlook

- Chapter 12 summarises the main results of the thesis and discusses the limitations on the experiment in its current state and details the future direction of the experiment.

1.5.1 Publications

Publications arising from this work

- K. McDonnell, *et al.*, *Demonstration of a CNOT gate based on electromagnetically induced transparency*, (In preparation)

Publications relating to this work

- C. J. Picken, *et al.*, *Entanglement of neutral-atom qubits with long ground-Rydberg coherence times*, Quantum Sci. Technol., **4**, 015011 (2019)

Chapter 2

Qubit Rotations and Quantum Gates

Quantum information processing, quantum computing and quantum simulation rely on the ability on initialise a qubit in a known quantum state and manipulate its quantum state by performing single or multi-qubit gates. In this chapter we outline the fundamental building blocks of quantum information processing, formally defining qubits and their rotations to realise quantum gates. We introduce the Bloch sphere to help visualise qubit gates and motivate the implementation of quantum information processing on a physical system.

2.1 Qubits

The fundamental building block for quantum information processing (QIP) is the quantum bit or *qubit* which is analogous to a *bit* in classical (digital) computing. In classical computing, the bit has two logical values 0 or 1 whereas the qubit is a quantum mechanical two-level system which can take the values $|0\rangle$, $|1\rangle$ or a superposition of the two given in Dirac notation by,

$$|\psi\rangle = c_0 |0\rangle + c_1 |1\rangle \equiv \begin{pmatrix} c_0 \\ c_1 \end{pmatrix}, \tag{2.1}$$

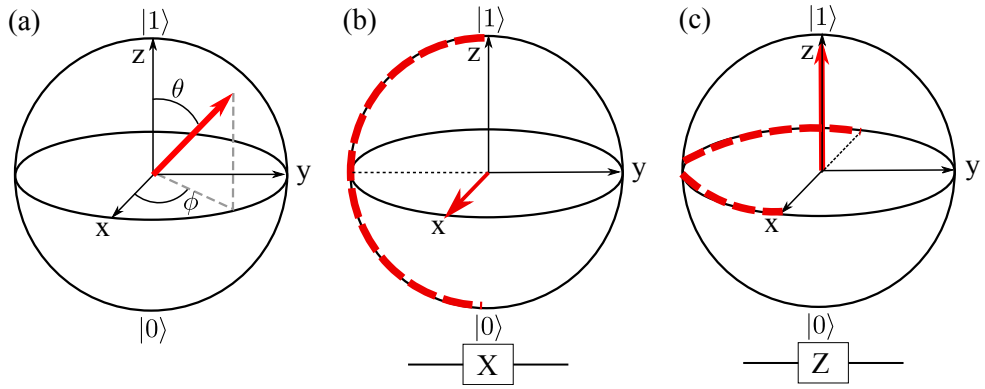

Figure 2.1: Bloch sphere representation of a qubit state for (a) a general qubit state define by polar angles θ and ϕ, (b) a NOT or X gate showing a rotation of $R_x(\pi)$ around the x axis and (c) a Z or phase gate showing a rotation ϕ around the z axis.

for complex coefficients c_0 and c_1 with the normalisation condition requiring

$$|c_0|^2 + |c_1|^2 = 1. \tag{2.2}$$

In general a n-qubit register has 2^n mutually orthogonal states of the form $|x_1 x_2 \dots x_n\rangle$, where $x_k \in \{0, 1\}$ for $1 \leq k \leq n$. Any state of the system can then be specified by 2^n complex amplitudes c_x as [65]

$$|\psi_n\rangle = \sum_x c_x |x\rangle , \tag{2.3}$$

and normalised as $\sum_x |c_x|^2 = 1$. Therefore, as the number of qubits increases the number of amplitudes specifying the state of the quantum system becomes very large which makes simulating quantum systems very difficult on classical computers.

The quantum state of a qubit can be represented graphically using the *Bloch sphere* which is a sphere of unit radius mapped out by the Bloch vector. By writing Eq. 2.1 in a general from

$$|\psi\rangle = \cos\left(\frac{\theta}{2}\right)|0\rangle + e^{i\phi}\sin\left(\frac{\theta}{2}\right)|1\rangle , \tag{2.4}$$

the polar angles (θ, ϕ) can be used to specify the qubit state on the Bloch sphere. The Bloch sphere representation of the qubit state is illustrated in Fig. 2.1(a) with the poles of the Bloch sphere representing the pure states $|0\rangle$ $(\theta = 0)$ and

$|1\rangle$ ($\theta = \pi$) and the equatorial positions on the outer surface of the Bloch sphere representing equally weighted superpositions of $|0\rangle$ and $|1\rangle$ with varying degrees of relative phase ϕ.

2.2 Quantum Logic Gates

A classical computer is made up of a memory and a processor that store and carry out operations on the bits. The processing operations are carried out as a circuit of binary logic gates such as the NOT and NAND gates, that perform operations on one or two bits at a time. The gates take the input bit(s) and perform the operation on the bit(s) to give a new output such as those shown in the truth tables for the classical NOT and NAND gates in Tables 2.1 and 2.2 respectively. The program then determines how the logical circuit will carry out the gates and in what order. The power of the NAND gate is that it is a universal gate meaning that any other classical gate can be represented as a combination of NAND gates.

Quantum computing takes a similar approach to the classical case. A series of quantum logic gates are carried out on the qubits which are stored in a quantum register and specific processing tasks are carried out by a quantum circuit. Typically a quantum circuit is represented by a block diagram as shown in Fig. 2.2 as this is an easy way to represent the qubits and gates, especially as the number of each increases.

Input bit	Output Bit
0	1
1	0

Table 2.1: Truth table for the single-bit NOT gate.

Input bit A	Input bit B	Output Bit
0	0	1
1	0	1
0	1	1
1	1	0

Table 2.2: Truth table for the two-bit NAND gate.

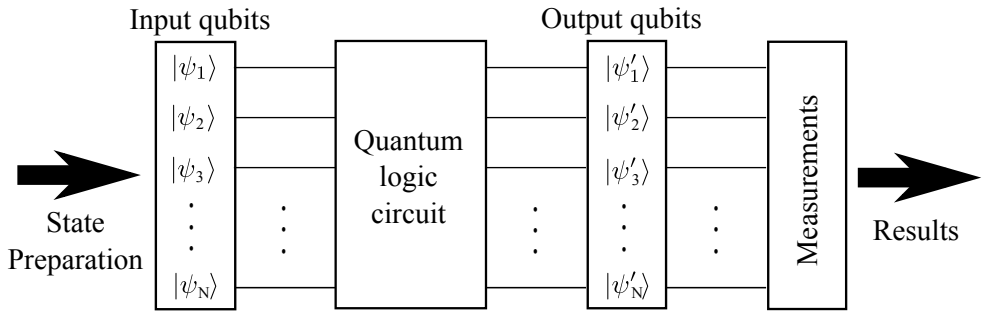

Figure 2.2: Block diagram used to represent the workings of a quantum computer. The input qubits $\{|\psi_1\rangle, |\psi_2\rangle, \ldots, |\psi_N\rangle\}$ are initialised and fed into the quantum logic circuit. The quantum logic circuit implements the gate operations and outputs a new set of qubits $\{|\psi'_1\rangle, |\psi'_2\rangle, \ldots, |\psi'_N\rangle\}$ which are then measured and read out.

In order to discuss quantum information processing in detail, we need to define single and two-qubit gates.

2.2.1 Single Qubit Gates

A single-qubit gate is one that takes a single qubit input state $|\psi\rangle$, and applies the gate operation U to output another qubit state $|\psi'\rangle$ i.e. $\mathrm{U}|\psi\rangle = |\psi'\rangle$. The normalisation condition on the qubit state given in Eq. 2.2 must hold true for the final qubit state after the gate has been applied, this means that the gate matrix U should be unitary

$$\mathrm{U}^\dagger \mathrm{U} = \mathrm{I}, \tag{2.5}$$

where $\mathrm{U}^\dagger$ is the adjoint of matrix U, and I is the identity matrix. In the circuit model of quantum computing, this condition implies that all single qubit quantum gates are reversible [12, 66].

To relate the gate matrix operations of qubits as rotations on the Bloch sphere, it is convenient to consider the density matrix $\hat{\rho} = |\psi\rangle\langle\psi|$. Expressing the density matrix in terms of the Pauli matrices gives the relation

$$\begin{aligned} \hat{\rho} &= \frac{1}{2}(I + X\cos\phi\cos\theta + Y\sin\phi\sin\theta + Z\cos\theta) \\ &= \frac{1}{2}(I + \hat{\mathbf{r}}_\rho \cdot \hat{\sigma}), \end{aligned} \tag{2.6}$$

where $\hat{\mathbf{r}}_\rho = (r_x, r_y, r_z)$ is the unit Bloch vector and $\hat{\sigma}$ is the Pauli matrix vector elements. The Pauli matrices are [12]

$$X = \begin{pmatrix} 0 & 1 \\ 1 & 0 \end{pmatrix}, \qquad Y = \begin{pmatrix} 0 & -i \\ i & 0 \end{pmatrix}, \qquad Z = \begin{pmatrix} 1 & 0 \\ 0 & -1 \end{pmatrix}, \tag{2.7}$$

and, when exponentiated give rise to the rotation operators [12]

$$\hat{R}_x(\theta) = -ie^{\frac{\theta}{2}X} = \begin{pmatrix} \cos\frac{\theta}{2} & -i\sin\frac{\theta}{2} \\ -i\sin\frac{\theta}{2} & \cos\frac{\theta}{2} \end{pmatrix}, \tag{2.8a}$$

$$\hat{R}_y(\theta) = ie^{\frac{\theta}{2}Y} = \begin{pmatrix} \cos\frac{\theta}{2} & -\sin\frac{\theta}{2} \\ \sin\frac{\theta}{2} & \cos\frac{\theta}{2} \end{pmatrix}, \tag{2.8b}$$

$$\hat{R}_z(\theta) = -ie^{\frac{\theta}{2}Z} = \begin{pmatrix} e^{-i\theta/2} & 0 \\ 0 & e^{i\theta/2} \end{pmatrix}, \tag{2.8c}$$

which rotate the Bloch vector by an angle θ about the $\hat{x}, \hat{y}$ and $\hat{z}$ axes respectively. The rotation matrices $\hat{R}_x(\theta)$ and $\hat{R}_z(\theta)$ are of particular interest as they are used to represent the single qubit quantum NOT and phase gates respectively, which will be demonstrated experimentally later in this thesis.

The quantum NOT gate acts in a similar manner to the classical equivalent by flipping the amplitude coefficients of the qubits as shown in Fig 2.1(b). Note that in the case of the quantum NOT gate there is an arbitrary phase associated with the rotation which enables different qubit states to be reached other than just a complete flip of the qubit from $|1\rangle \leftrightarrow |0\rangle$. The phase gate is often called the Z gate as it performs a rotation of angle $\phi = \pi$ around the z-axis as shown in Fig. 2.1(c). The Z-gate results in a sign change of the coefficients of the qubit state as result of the phase change. The quantum NOT and phase gates are typically represented by the symbols X and Z respectively as a result of the rotations on the Bloch sphere.

The final single-qubit gate of interest is the Hadamard gate,

$$H = \frac{1}{\sqrt{2}} \begin{pmatrix} 1 & 1 \\ 1 & -1 \end{pmatrix}, \tag{2.9}$$

Input qubits		Output qubits	
Control	Target	Control	Target
$\|0\rangle$	$\|0\rangle$	$\|0\rangle$	$\|0\rangle$
$\|0\rangle$	$\|1\rangle$	$\|0\rangle$	$\|1\rangle$
$\|1\rangle$	$\|0\rangle$	$\|1\rangle$	$\|1\rangle$
$\|1\rangle$	$\|1\rangle$	$\|1\rangle$	$\|0\rangle$

Table 2.3: Truth table for the controlled-NOT gate which takes two input qubits labelled the control and target qubits, and flips the state of the target qubit if the value of the control input is $|1\rangle$.

which turns the basis state into a superposition state. For example the states $|0\rangle$ and $|1\rangle$ under the Hadamard gate become $(|0\rangle + |1\rangle)/\sqrt{2}$ with equal probability that the measured qubit state will be $|0\rangle$ or $|1\rangle$. The Hadamard gate is extremely useful when generating quantum gates as it enables superpositions of qubits to be easily formed. Further quantum gate operations can then be performed on the superposition state leading to maximal entanglement, a purely quantum phenomenon.

2.2.2 Two-Qubit Gates

The two-qubit gate discussed in this thesis is the *controlled-NOT gate* (*CNOT gate*) which has two input qubits called the *control* and *target* qubits. The CNOT gate acts on the qubits by changing the state of the input target qubit if and only if the control qubit is in state $|1\rangle$ as shown in Table 2.3.

The unitary matrix for the CNOT operation is

$$\mathrm{U_{CNOT}} = \begin{pmatrix} 1 & 0 & 0 & 0 \\ 0 & 1 & 0 & 0 \\ 0 & 0 & 0 & 1 \\ 0 & 0 & 1 & 0 \end{pmatrix}, \tag{2.10}$$

where the state vector is $(|00\rangle, |01\rangle, |10\rangle, |11\rangle)^{\mathrm{T}}$ with the control qubit written first. This matrix has the effect of swapping the amplitude of the coefficients for the $|10\rangle$ and $|11\rangle$ states, whilst leaving the coefficient for the $|00\rangle$ and $|01\rangle$ states unchanged.

The CNOT gate can be coupled with an appropriate single qubit gate to realise a universal set of quantum gates [12]. A common combination of gates is the Hadamard applied to the control qubit followed by the CNOT applied to both qubits as these combined operations generate maximally entangled states.

2.3 Entanglement

If we consider two qubits A and B in states $|\psi\rangle_A$ and $|\psi\rangle_B$, either qubit has the possibility to be in state $|0\rangle$ or $|1\rangle$ or a superposition of the two. A pair of qubits can exist in any state of the form

$$|\psi\rangle = c_{00}|00\rangle + c_{01}|01\rangle + c_{10}|10\rangle + c_{11}|11\rangle, \tag{2.11}$$

where the complex coefficients c_x for $x = \{00, 01, 10, 11\}$, are normalised as $\sum_x |c_x|^2 = 1$. A superposition can be understood classically but entanglement has no classical equivalent and is a purely quantum phenomenon.

A pair of qubits is said to be in an entangled state if it's wavefunction cannot be written as a product of the wavefunction of the individual qubits i.e. $|\psi\rangle \neq |\psi\rangle_A \otimes |\psi\rangle_B$ [67]. This means that a measurement on one qubit will be correlated to the outcome of the measurement of the other qubit which was described by Einstein as 'spooky action at a distance' [68].

In the two-atom basis a maximally entangled state can be created by applying a Hadamard gate to the control qubit followed by a CNOT gate to both qubits, generating one of the maximally entangled Bell states [69]

$$|\Phi^{\pm}\rangle = \frac{1}{\sqrt{2}}(|00\rangle \pm |11\rangle), \tag{2.12a}$$

$$|\Psi^{\pm}\rangle = \frac{1}{\sqrt{2}}(|01\rangle \pm |10\rangle), \tag{2.12b}$$

named after John Bell who formally reviewed the paper written by Einstein, Podolsky and Rosen [68].

2.3.1 Measuring Entanglement

There are two main ways in which entanglement is measured: these are parity oscillations and quantum state tomography. Quantum state tomography involves reconstructing the whole density matrix by taking measurements in the x and y basis and is a lengthy process requiring many measurements to verify entanglement [70, 71]. The more common approach is observing parity oscillations [72].

To map out a parity oscillation we consider the state overlap fidelity which is defined as [72]

$$\mathcal{F} = |\langle\psi_i|\psi\rangle|^2 = \langle\psi_i|\,\rho\,|\psi\rangle = [\mathrm{Tr}(\sigma\sqrt{\rho}\sigma)]^2, \tag{2.13}$$

where $|\psi_i\rangle$ is the ideal target state, $\sigma = |\psi_i\rangle\langle\psi_i|$ and $\rho = |\psi\rangle\langle\psi|$ is the density matrix. A general two-qubit density matrix has the form

$$\rho = \begin{pmatrix} P_{00} & a & b & c \\ a^* & P_{01} & d & f \\ b^* & d^* & P_{10} & g \\ c^* & f^* & g^* & P_{11} \end{pmatrix}, \tag{2.14}$$

where the diagonal elements represent the real populations and the off-diagonal elements are the complex coherences.

For the two-qubit density matrix given by Eq. 2.14, the Bell state preparation fidelities are

$$\mathcal{F}_{|\Phi^\pm\rangle} = \left\langle\Phi^\pm\right|\rho\left|\Phi^\pm\right\rangle = (\rho_{00} + \rho_{11})/2 + |c|, \tag{2.15a}$$

$$\mathcal{F}_{|\Psi^\pm\rangle} = \left\langle\Psi^\pm\right|\rho\left|\Psi^\pm\right\rangle = (\rho_{01} + \rho_{10})/2 + |d|, \tag{2.15b}$$

which shows that we need to measure the Bell state populations and the off-diagonal coherence terms c and d. By measuring the coherence terms we are able to distinguish between a phase-coherent entangled state and an incoherence statistical

mixture. We measure the coherence terms by mapping a parity oscillation. The parity of the state is defined as [72],

$$\Pi \equiv \sum_{j=0}^{N} (-1)^j P_j = P_{00} + P_{11} - P_{01} - P_{10}, \tag{2.16}$$

where N is the number of qubits in the system. The parity oscillates under an analysis pulse dependent on the prepared state from which different off-diagonal elements can be accessed.

To measure the coherence terms the choice of analysis pulse is crucial as this determines the off-diagonal elements that will oscillate in the parity. For example an analysis pulse comprised of a global phase $Z(\phi)$ followed by global rotation $X(\pi/2)$ can be used to map out a parity oscillation for the Bell states $|\Phi^{\pm}\rangle$ but no oscillation will be observed for the Bell states $|\Psi^{\pm}\rangle$ and, crucially, a mixed state such as $(|10\rangle + |00\rangle)/\sqrt{2}$ under this rotation. This particular choice of analysis pulse is one that we used to measure the coherence of the Bell state $|\Phi^{+}\rangle$ and will be discussed in Sec. 11.6.

2.4 Practical Implementation using atoms

The results presented in this thesis are concerned with neutral caesium atoms excited to the high-lying Rydberg state $|r\rangle = \left|81D_{5/2}, m_j = 5/2\right\rangle$. We use the hyperfine ground states of the caesium atom as qubits with

$$\begin{aligned} |0\rangle &\equiv |F = 3, m_F = 0\rangle\,, \\ |1\rangle &\equiv |F = 4, m_F = 0\rangle\,, \end{aligned}$$

where the magnetic sub-level $m_F = 0$ is chosen as it is insensitive to magnetic fields. Single qubit gates are performed using microwave and laser pulses to drive rotations between the qubit states $|1\rangle \rightarrow |0\rangle$. To perform two-qubit gates, we exploit the strong dipole-dipole interaction between the atoms and use the property of Rydberg blockade as a way to entangle the states of two neighbouring atoms [31],

as has been demonstrated by many groups [47, 73, 74]. Using atoms as qubits offer long coherence times, a scalable system on which to perform gates [32] and well-established methods for manipulating and measuring the atoms

Part II

Atom-Light Interactions

Chapter 3

Two-level Atom

The two-level atom is the simplest case in which to consider the interaction between an atom and a coherent light field. Suppose we have a two-level atom with energy levels $|g\rangle$ and $|e\rangle$ separated in energy by $\hbar(\omega_e - \omega_g) = \hbar\omega_0$, which interacts with a monochromatic electromagnetic field, ω, detuned from the atomic resonance $|g\rangle \rightarrow |e\rangle$ by $\Delta = \omega_0 - \omega$, as shown in Fig. 3.1(a). We can write the Hamiltonian for the system as

$$\mathcal{H} = \mathcal{H}_{\mathrm{A}} + \mathcal{H}_{\mathrm{AL}}(t), \tag{3.1}$$

where $\mathcal{H}_{\mathrm{A}} = \hbar\omega_0 |e\rangle\langle e|$ is the Hamiltonian for the bare atom and $\mathcal{H}_{\mathrm{AL}}(\mathrm{t}) = -\mathbf{d}\cdot\boldsymbol{E}(t)$ is the Hamiltonian describing the atom-light interaction in the dipole approximation, with electric field $\boldsymbol{E}(t) = \boldsymbol{\varepsilon} E_0 \cos(\omega t)$ and electric dipole $\mathbf{d} = -e\hat{\mathbf{r}}$.

The atomic wavefunction at any time t is given by

$$|\psi(t)\rangle = c_g(t)e^{-i\omega_g t}|g\rangle + c_e(t)e^{-i\omega_e t}|e\rangle\,, \tag{3.2}$$

where $c_i(t)$ are the complex amplitudes normalised as $\sum_i |c_i(t)|^2 = 1$. The evolution of the system is governed by the the time-dependent Schrödinger equation (TDSE),

$$i\hbar\frac{\partial|\psi(t)\rangle}{\partial t} = \hat{\mathcal{H}}|\psi(t)\rangle\,. \tag{3.3}$$

Solving the TDSE using Eqs. 3.1 and 3.2, and using the exponential form of

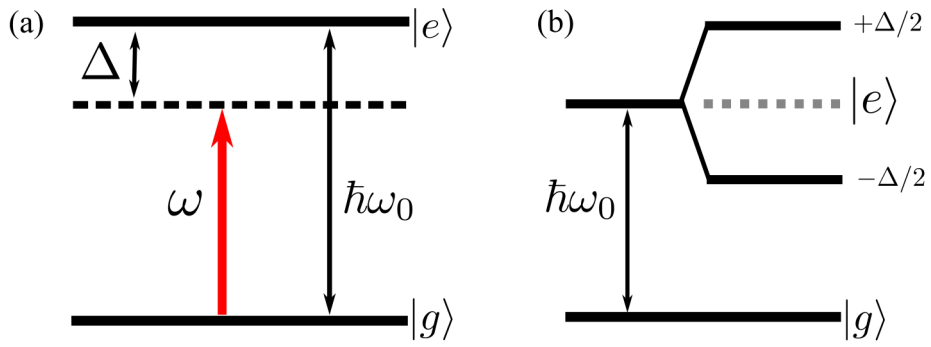

Figure 3.1: A schematic of (a) a two-level atom with states $|g\rangle$ and $|e\rangle$ separated in energy by $\hbar\omega_0$ interacting with an electromagnetic field characterised by ω and detuned from the atomic resonance by Δ. (b) Energy shifts created by the electromagnetic field.

$\cos(\omega t)$, we obtain a coupled set of equations

$$\dot{c}_g(t) = i\frac{\Omega^*}{2}\left[e^{i(\omega-\omega_0)t} + e^{-i(\omega+\omega_0)t}\right]c_e(t), \tag{3.4a}$$

$$\dot{c}_e(t) = i\frac{\Omega}{2}\left[e^{i(\omega+\omega_0)t} + e^{-i(\omega-\omega_0)t}\right]c_g(t), \tag{3.4b}$$

where we have introduced the Rabi frequency $\Omega = -\frac{\boldsymbol{d}\cdot\boldsymbol{E}}{\hbar}$ which describes the coupling strength between the atom and the electric field.

We can employ the *rotating wave approximation* (RWA) to remove the counter-rotating terms $(\omega+\omega_0)$ which oscillate at roughly twice the frequency of the driving field when $|\omega - \omega_0| \ll \omega_0$ so that they average to zero [75]. This leads to

$$\dot{c}_g(t) = i\frac{\Omega^*}{2}e^{i\Delta t}c_e(t), \tag{3.5a}$$

$$\dot{c}_e(t) = i\frac{\Omega}{2}e^{-i\Delta t}c_g(t), \tag{3.5b}$$

where $\Delta = \omega - \omega_0$ is the detuning.

To remove the time dependence $e^{-i\Delta t}$ we use the transformations [76]:

$$\tilde{c}_g(t) = c_g(t)e^{-i\Delta t/2}, \tag{3.6a}$$

$$\tilde{c}_e(t) = c_e(t)e^{i\Delta t/2}, \tag{3.6b}$$

to obtain a new set of coupled equations

$$\dot{\tilde{c}}_g(t) = -i\frac{\Delta}{2}\tilde{c}_g(t) - i\frac{\Omega^*}{2}\tilde{c}_e(t), \tag{3.7a}$$

$$\dot{\tilde{c}}_e(t) = -i\frac{\Omega}{2}\tilde{c}_g(t) + i\frac{\Delta}{2}\tilde{c}_e(t), \tag{3.7b}$$

describing the evolution of the two-level system under the influence of an oscillating E.M. field, with an effective Hamiltonian

$$\mathcal{H}_{\text{eff}} = \frac{\hbar}{2}\begin{pmatrix} \Delta & \Omega^* \\ \Omega & -\Delta \end{pmatrix}. \tag{3.8}$$

3.1 Rabi Oscillations

If we assume that at $t = 0$ the total population is in state $|g\rangle$ i.e. $c_g = 1$ and $c_e = 0$, then Eqs. 3.7 can be solved to give the probability that the atom is in the excited state at a given time t:

$$P_e(t) = |c_e(t)|^2 = \frac{\Omega^2}{\Omega'^2}\sin^2\left(\frac{\Omega' t}{2}\right), \tag{3.9}$$

where $\Omega' = \sqrt{|\Omega|^2 + \Delta^2}$. On resonance, $\Delta = 0$, the probability for the atom to be in state $|e\rangle$ reduces to

$$P_e(t) = \sin^2\left(\frac{\Omega t}{2}\right), \tag{3.10}$$

from which we can see that when $\Omega t = \pi$, the entire atomic population has been transferred $|e\rangle$. Similarly, when $\Omega t = 2\pi$, the population is returns to $|g\rangle$ and so on. This process repeats with odd integer multiples of π transferring the atomic population to $|e\rangle$ and even integer multiples of π returning the population to $|g\rangle$, thus mapping out an oscillation between $|g\rangle$ and $|e\rangle$ with frequency Ω. This oscillatory response is called *Rabi flopping* or Rabi oscillations. Fig. 3.2(a) shows Rabi oscillations when $\Delta = 0$ and $\Delta' = 0.8\Omega$ in blue and red respectively, both with the same Rabi frequency $\Omega/2\pi = 1$ MHz. This shows how significantly the detuning changes the population transfer between $|g\rangle$ and $|e\rangle$.

The solution $\Omega t = \pi$ is known as a π-*pulse* and is an example of a single qubit operation. In terms of the rotation matrices given by Eq. 2.8, a π-pulse is equivalent to

$$\hat{R}_x(\theta = \pi) = \begin{pmatrix} 0 & -i \\ -i & 0 \end{pmatrix}. \tag{3.11}$$

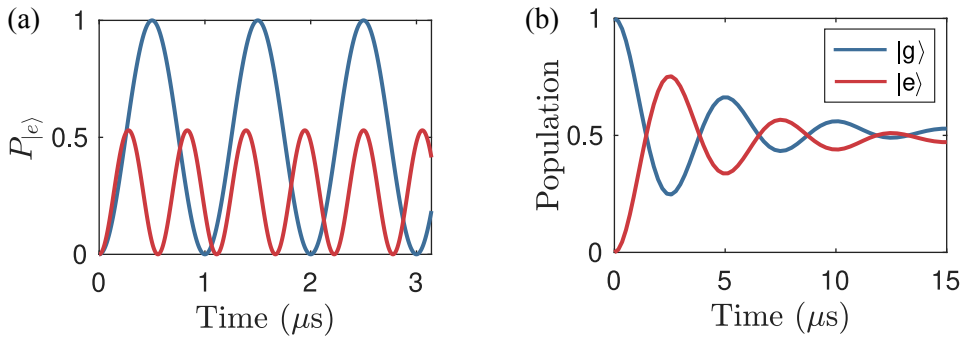

Figure 3.2: (a) Rabi oscillations showing the effect of detuning on the population in $|e\rangle$. The blue plot is for $\Delta = 0$ and the red is $\Delta' = 0.8\Delta$ which has significantly lower amplitude than the case with no detuning. (b) Rabi oscillations including decay from $|e\rangle$ by spontaneous emission showing damping of both excited and ground state populations to a steady state.

Similarly, a $\pi/2$-pulse, which is used to generate a superposition of the atomic states $|g\rangle$ and $|e\rangle$, is equivalent to the rotation

$$\hat{R}_x(\pi/2) = \frac{1}{\sqrt{2}} \begin{pmatrix} 1 & i \\ i & -1 \end{pmatrix}. \tag{3.12}$$

Both π and $\pi/2$-pulses will be used extensively in this thesis when demonstrating single and two-qubit gates.

3.2 AC Stark Shifts

The Hamiltonian given in Eq. 3.8 can be diagonalised to find the eigenvalues by solving the equation $\mathcal{H}\mathbf{x} = \lambda\mathbf{x}$. Taking the determinant gives

$$\begin{vmatrix} \hbar\Delta/2 - \lambda & \hbar\Omega/2 \\ \hbar\Omega/2 & -\hbar\Delta/2 - \lambda \end{vmatrix} = (\hbar\Delta/2 - \lambda)(-\hbar\Delta/2 - \lambda) - (\hbar\Omega/2)^2 = 0, \tag{3.13}$$

which has eigenenergies $\lambda_\pm = \pm\hbar\sqrt{\Delta^2 + \Omega^2}/2$.

For large detunings $|\Delta| \gg \Omega$, this results in an energy shift of the ground and excited states by $E = \pm\hbar\Omega^2/4\Delta$ which is known as the *AC Stark shift* or light

shift. The AC Stark shift depends on the intensity of the laser and on the sign of the detuning, and can be used to trap atoms in optical fields. For $\Delta < 0$ the light shift is attractive such that atoms will be trapped in regions of high intensity, whereas for $\Delta > 0$ the light shift is repulsive and atoms will be expelled from regions of high intensity. The experimental implementation of trapping atoms using a laser with negative detuning will be discussed in Sec. 7.3.

For a resonant interaction $\Delta = 0$, the energies are unperturbed with $E_\pm = \pm\hbar\Omega/2$. This leads to two new eigenstates for the system $|\pm\rangle = (|g\rangle \pm |e\rangle)/\sqrt{2}$ which are known as the dressed states [77] with the energy splitting $E_\pm$ called the Autler-Townes splitting [78].

3.3 Optical Bloch Equations

So far we have described the evolution of the system in terms of state vectors solved using the TDSE, but this description is not suitable for describing the effects of spontaneous emission or dephasing. To include these effects we use the density matrix, $\hat{\rho}$, and the optical Bloch equations to calculate the time evolution of the density matrix. We start by representing the system described by the state vector $|\psi\rangle$ in the analogous density matrix form.

The density operator $\hat{\rho}$, for a pure state represented by the state vector $|\psi\rangle = \sum c_n |n\rangle$, is defined as

$$\hat{\rho} = |\psi\rangle\langle\psi| \,, \tag{3.14}$$

which is written in density matrix form for the two-level atom as

$$\hat{\rho} = \begin{pmatrix} \rho_{gg} & \rho_{ge} \\ \rho_{eg} & \rho_{ee} \end{pmatrix} = \begin{pmatrix} c_g c_g^* & c_g c_e^* \\ c_e c_g^* & c_e c_e^* \end{pmatrix} \tag{3.15}$$

The diagonal elements of the density matrix are known as *populations* and represent the probability of finding the system in a particular state. The off-diagonal elements are known as *coherences* that depend on the relative phase between the states $|g\rangle$ and $|e\rangle$ and have the property $\rho_{eg} = \rho_{eg}^*$.

The density matrix can also be used to describe a statistical mixture of states $\{|\psi_i\rangle\}$ which has density matrix

$$\hat{\rho} = \sum_i P_i \left|\psi_i\right\rangle \left\langle\psi_i\right|, \tag{3.16}$$

where P_i is the probability of the system being in state $|\psi_i\rangle$ and $\mathrm{Tr}(\rho) = \sum_i P_i \leq 1$. Representing the system as a statistical mixture allows us to include the effects of spontaneous emission and dephasing because the state vector changes irreversibly as these effects are included.

Since the time evolution can be described in terms of the Hamiltonian, the time evolution of the density matrix is described by the equation

$$\frac{d\hat{\rho}}{dt} = -\frac{i}{\hbar}[\hat{\mathcal{H}}, \hat{\rho}], \tag{3.17}$$

involving the commutation between Hamiltonian of the system and the density operator [79]. This equation is called the Liouville's equation and is equivalent to the Schrödinger equation.

To include the effect of processes such as spontaneous emission, the effect of decay is added at a rate Γ. In the two-level system suppose the state $|e\rangle$ decays at a rate Γ_e, then the time evolution of the populations due to spontaneous emission is [79]

$$\frac{d\rho_{ee}}{dt} = -\frac{d\rho_{gg}}{dt} = -\Gamma_e \rho_{ee}, \tag{3.18}$$

and for the coherences,

$$\frac{d\rho_{eg}}{dt} = -\frac{\Gamma_e}{2}\rho_{eg}, \qquad -\frac{d\rho_{ge}}{dt} = -\frac{\Gamma_e}{2}\rho_{ge}. \tag{3.19}$$

The full equation governing the evolution of the density matrix is now [80]

$$\frac{d\hat{\rho}}{dt} = -\frac{i}{\hbar}[\hat{\mathcal{H}}, \hat{\rho}] - \begin{pmatrix} -\Gamma_e \rho_{ee} & \frac{\Gamma_e}{2}\rho_{ge} \\ \frac{\Gamma_e}{2}\rho_{eg} & \Gamma_e \rho_{ee} \end{pmatrix}. \tag{3.20}$$

Using the Hamiltonian given by Eq. 3.8, we expand the commutator to obtain the

coupled equations,

$$\dot{\rho}_{gg} = \frac{i}{2}(\Omega\tilde{\rho}_{ge} - \Omega^*\tilde{\rho}_{eg}) + \Gamma_e\rho_{ee}, \tag{3.21a}$$

$$\dot{\rho}_{ge} = -(i\Delta + \Gamma_e/2)\tilde{\rho}_{ge} - \frac{i\Omega^*}{2}(\rho_{ee} - \rho_{gg}), \tag{3.21b}$$

$$\dot{\rho}_{eg} = (i\Delta - \Gamma_e/2)\tilde{\rho}_{eg} + \frac{i\Omega}{2}(\rho_{ee} - \rho_{gg}), \tag{3.21c}$$

$$\dot{\rho}_{ee} = -\frac{i}{2}(\Omega\tilde{\rho}_{ge} - \Omega^*\tilde{\rho}_{eg}) - \Gamma_e\rho_{ee}, \tag{3.21d}$$

which are the *optical Bloch equations* (OBE) describing the time evolution of the density matrix that includes the damping of the Rabi oscillations due to spontaneous emission [79, 80].

The probability of finding the atom in the state $|e\rangle$ which includes the effect of damping is now given by [79],

$$P_{|e\rangle} = \frac{\Omega^2}{2\Omega^2 + \Gamma_e^2}\left[1 + e^{-3\Gamma_e t/4}\left(\cos\left(\tilde{\Omega}t\right) + \frac{3\Gamma_e}{4\tilde{\Omega}}\sin\left(\tilde{\Omega}t\right)\right)\right], \tag{3.22}$$

where $\tilde{\Omega} = \sqrt{\Omega^2 + \Gamma_e^2/4}$ and we have assumed a resonant excitation. The damping of the Rabi oscillations converge to a steady state when the time derivate vanishes, with solutions

$$\rho_{ee}^{ss} = \frac{|\Omega|^2/4}{|\Omega|^2/2 + \Gamma_e^2/4 + \Delta^2}, \tag{3.23a}$$

$$\rho_{eg}^{ss} = \frac{\Omega}{2}\frac{\Delta - i\Gamma_e/2}{|\Omega|^2/2 + \Gamma_e^2/4 + \Delta^2}, \tag{3.23b}$$

for the populations and coherences respectively. The effect damping has on the populations of the states $|g\rangle$ and $|e\rangle$ is shown in Fig. 3.2(b) as the Rabi oscillations damp to a steady state with equal atomic population in each state.

3.4 Bloch Sphere

To better understand the effect of coupling the system to the environment, it is useful to use the Bloch sphere where the density matrix elements are represented by vectors on a sphere of unit radius. The Bloch vector is represented by $\boldsymbol{R} =$

$u\hat{\boldsymbol{x}} + v\hat{\boldsymbol{y}} + w\hat{\boldsymbol{z}}$ with the density operator written in the Bloch basis as

$$u = \tilde{\rho}_{ge} + \tilde{\rho}_{eg}, \tag{3.24a}$$

$$v = -i(\tilde{\rho}_{ge} - \tilde{\rho}_{eg}), \tag{3.24b}$$

$$w = \rho_{ee} - \rho_{gg}, \tag{3.24c}$$

where w represents population inversion of the system. In the Bloch sphere picture, the states $|g\rangle$ and $|e\rangle$ lie at the poles of the sphere while an atom in the superposition state $(|g\rangle + |e\rangle)/\sqrt{2}$ lies in the equatorial plane with time evolution leading to precession of the vector around the $x-y$ plane. For a statistical mixture of states $|\boldsymbol{R}| < 1$ and corresponds to a point inside the Bloch sphere whereas a superposition state has $|\boldsymbol{R}| = 1$ corresponding to a position on the surface of the Bloch sphere [67]. The Bloch sphere is thus a useful tool for describing decoherence - the evolution of a pure quantum state into a statistical mixture of states - serving as a boundary between quantum and classical physics [81].

Fig. 3.3(a) shows a π-pulse with $\Delta = 0$ demonstrating population transfer from $|g\rangle$ to $|e\rangle$ and Fig. 3.3(b) shows the same π-pulse when $\Delta \neq 0$, such that the population does not transfer between the states $|g\rangle$ and $|e\rangle$. The effect of spontaneous emission in the Bloch sphere picture is illustrated in Fig. 3.3(c) showing the transfer of the atomic population decaying to a steady state. Figs. 3.3(a)-(c) show equivalent results to Figs. 3.2(a)-(b) with the atomic population transfer illustrated on the Bloch sphere.

Expressing the OBE (Eq. 3.21) in terms of the Bloch vector we get [75]

$$\dot{u} = \Delta v - \frac{u}{T_2}, \tag{3.25a}$$

$$\dot{v} = -\Delta u + \Omega w - \frac{v}{T_2}, \tag{3.25b}$$

$$\dot{w} = -\Omega v - \frac{w - w_{\mathrm{st}}}{T_1}, \tag{3.25c}$$

where the decay rate Γ_e has been substituted with the decay times T_1 and T_2. The decay times are governed by two decay types: homogeneous effects, which are irreversible, and inhomogeneous effects which are reversible.

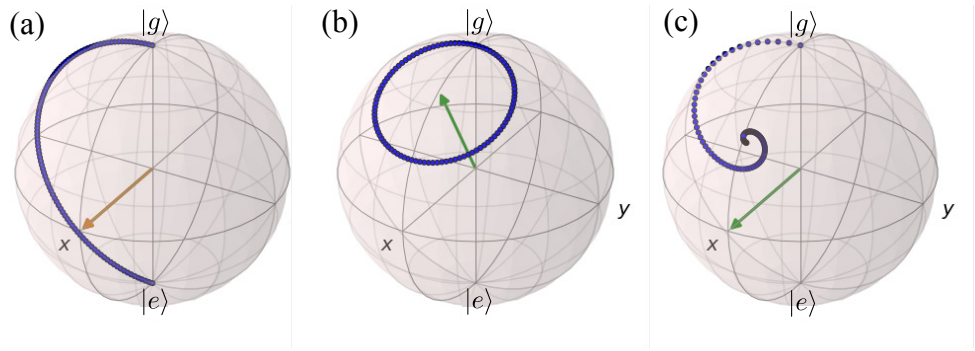

Figure 3.3: Bloch sphere representation of Rabi oscillations between $|g\rangle \rightarrow |e\rangle$ showing (a) a perfect π-pulse with $\Delta = \Gamma_e = 0$, (b) the effect of detuning and (c) the effect of spontaneous emission.

The easiest effect to understand is the longitudinal decay time T_1, which describes the effect of spontaneous emission. This results in population decay to the steady state w_{st} due to random changes of the phase of the coherences which irreversibly damp the Rabi oscillations. The rate of longitudinal relaxation is determined by the lifetime of $|e\rangle$ which includes transitions to the ground state and other non-resonant levels that have been neglected in the two-level approximation.

The transverse decay time T_2 is related to the homogeneous transverse decay time T_2' and the inhomogeneous transverse decay time T_2^* by the relation [82]

$$\frac{1}{T_2} = \frac{1}{T_2'} + \frac{1}{T_2^*}. \tag{3.26}$$

T_2' is related to dephasing processes that do not change the population of the system but do have an effect on the phase of the wavefunction describing the state. Examples of such a process are trapping laser intensity fluctuations or fluctuating magnetic fields. T_2' is particularly prominent in trapping experiments as data are acquired by averaging over many repetitions of the same experiment. The reversible dephasing T_2^* is caused by the precession of atoms around the Bloch sphere occurring at different rates, which in turn causes a loss of phase-coherence. This process can be reversed experimentally using Ramsey spectroscopy and spin-echo techniques which are extensively used in many experiments, especially in the atomic clock community [83, 84].

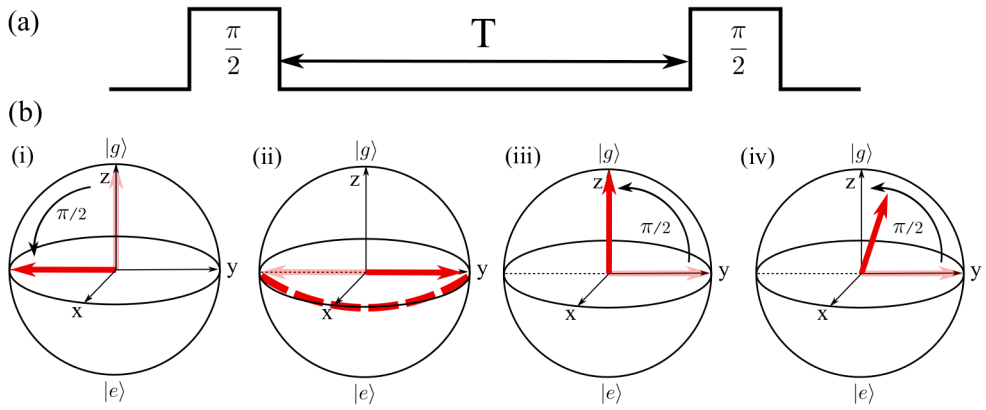

Figure 3.4: (a) The sequence of pulses for Ramsey spectroscopy, (b) the evolution of the Bloch vector for the atomic population: (i) the initial $R_x(\pi/2)$ rotation places the Bloch vector on the $x-y$ plane, (ii) the population progression around the $x-y$ plane during the free-evolution time T, the final $R_x(\pi/2)$ rotation (iii) returns the population to $|g\rangle$ for a resonant Ramsey sequence or (iv) the population is left in a superposition of the states $|g\rangle$ and $|e\rangle$ for a non-resonant Ramsey sequence.

3.5 Ramsey Spectroscopy

Ramsey spectroscopy is well suited to study the decoherence effects which occur in atomic systems [85]. The idea behind Ramsey spectroscopy is to apply two coherent pulses (typically microwave or optical) separated in time. The method is sensitive to phase shifts between the atomic resonance and the driving field which is why the Bloch sphere is a good way to visualise the system. Ramsey spectroscopy produces fringes, the frequency of which correspond to the differential shift the atoms experience during the free evolution time and the detuning from resonance. The visibility of the fringes reduces as atoms lose their phase relationship, i.e. they decohere. The application of Ramsey fringes to experiments related to this thesis are discussed in detail Sec. 10.3, for now we give an overview of the typical method used.

Ramsey fringes are performed using two $R_x(\pi/2)$ rotations of duration τ, separated by a free evolution time T as illustrated in Fig. 3.4(a). If the atoms are prepared in state $|g\rangle$ with Bloch vector $u = (0, 0, -1)$, then applying a $R_x(\pi/2)$ rotation

rotates the atoms into the $x-y$ plane with Bloch vector $u=(0,-1,0)$ as shown in Fig. 3.4(i). During the free evolution time, the atoms freely precess around the z-axis with angular frequency Δ such that after T the rotation angle of the Bloch vector in the $x-y$ plane is

$$\boldsymbol{R}(T)=\begin{pmatrix}-\sin(\Delta T)\\-\cos(\Delta T)\\0\end{pmatrix}. \tag{3.27}$$

The second $R_x(\pi/2)$ pulse is then applied to the atoms which produces one of the following outcomes:

1. If $\Delta=0$, there is no precession of the Bloch vector between the $R_x(\pi/2)$ rotations and the atoms are transferred to state $|e\rangle$ by the second $R_x(\pi/2)$ rotation.

2. If $\Delta T=\pi$, the Bloch vector has undergone a rotation equal to π in the $x-y$ plane between the $R_x(\pi/2)$ pulses and the atoms are transferred back to the state $|g\rangle$ with the application of the second $R_x(\pi/2)$ pulse, as is the case shown in Fig. 3.4(iii).

3. In any other case, the atom is left in a superposition state $\left(|e\rangle+i\,|g\rangle\right)/\sqrt{2}$ after the second $R_x(\pi/2)$ pulse as illustrated in Fig. 3.4(iv), for small detuning.

The probability to find the atom in the state $|e\rangle$ after the second pulse is [86]

$$P_e(t)=4\frac{\Omega^2}{\Omega'^2}\sin^2\left(\frac{\Omega'\tau}{2}\right)\left[\cos\left(\frac{\Delta T}{2}\right)\cos\left(\frac{\Omega' T}{2}\right)-\frac{\Delta}{\Omega'}\sin\left(\frac{\Delta T}{2}\right)\sin\left(\frac{\Omega' T}{2}\right)\right]^2. \tag{3.28}$$

For the atoms excited by two pulses the excitation probability drops from the maximum at $\omega=\omega_0$ to zero when $\Delta T/2=\pi/2$ so that the FWHM is

$$\Delta f=\frac{1}{2T}. \tag{3.29}$$

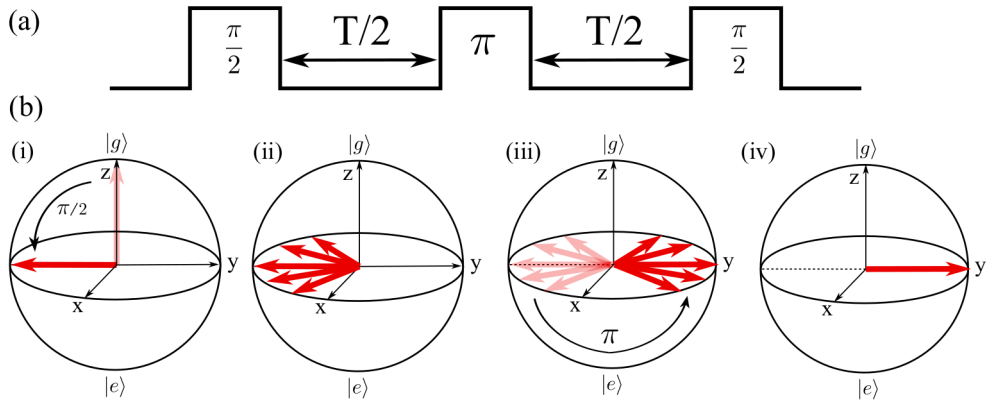

Figure 3.5: (a) The sequence for Ramsey spectroscopy with a spin-echo pulse that can be applied to reverse the inhomogeneous dephasing T_2^*. (b) The evolution of the Bloch vector during the spin-echo sequence (i) A $\pi/2$ pulse is applied to rotate the Bloch vector to the $x-y$ plane, (ii) the Bloch vectors precess with different angular frequencies, which is corrected by (iii) applying a spin echo (π-pulse) to reverse the dephasing process, such that (iv) the Bloch vectors converge. The final $\pi/2$ pulse returns the Bloch vector to $|g\rangle$ if T_1 is negligible, otherwise the Bloch vector decays from $|g\rangle$ proportional to T_1.

From this we can see that the longer the time T that the atoms spend evolving freely, the narrower the the FWHM thus improving the sensitivity of the measurement [75]. In practice the limit on T is often determined by factors such as heating from the atomic trapping beams or background collisions within a vacuum chamber.

To reverse the effect of the dephasing time T_2^*, a spin-echo pulse can be applied between the $R_x(\pi/2)$ pulses of the Ramsey sequence at a time $T/2$, illustrated in Fig. 3.5(a). The sequence influences the evolution of the population in the following way: (i) the initial $R_x(\pi/2)$ rotation, rotates the Bloch vector of the atoms to the $x-y$ plane, then (ii) as the atoms freely precess, they do so with different angular frequencies. If uncorrected this leads to decay of the observed Ramsey fringes as the fringes are an average of many oscillations of slightly different frequencies. To correct this, (iii) a spin-echo pulse is applied which reverses the angular frequencies, such that the faster and slower frequencies are in the reverse

order and (iv) converge again. The final $R_x(\pi/2)$ rotation returns the Bloch vector to $|g\rangle$ if T_1 is negligible, otherwise spontaneous emission occurs, resulting in the Bloch vector pointing off-axis by an amount proportional to T_1.

The spin-echo pulse is a $R_z(\pi)$ rotation which reverses the rotation of the atoms around the $x-y$ plane of the Bloch sphere, allowing the different precession rates to unify and restore phase coherence during the free evolution time. Such a technique has been successfully used to increase the coherence of quantum gates [30].

3.6 Summary

Studying the the two-level atom is an excellent way to derive the underlying physics of atom-light interactions. The model encapsulates atomic population transfer between states and includes the effects of decay and damping, described by the optical Bloch equations. This chapter has also covered the Bloch sphere representation of the two-level system and associated results such as Ramsey spectroscopy, which will be demonstrated in later chapters.

Chapter 4

Three Level Atom

The two-level system captures most of the physics behind atom-light interactions, but we also need to discuss a three-level atomic system to accurately describe the experiment and understand the effect of electromagnetically induced transparency. There are three configurations that a three-level system can take: the Λ-, ladder- and V-configurations. In this thesis, we will focus on the Λ-configuration as this describes the Raman transitions between the hyperfine ground states of the caesium atoms in our experiment. However we include a brief discussion of the ladder configuration as this is used to drive two-photon excitations to the Rydberg state.

4.1 Three-level Λ-configuration

In the three-level Λ-configuration the states are $|0\rangle$, $|1\rangle$ and $|P\rangle$ separated in energy by $\hbar\omega_{0p}$ and $\hbar\omega_{p1}$ as shown in Fig. 4.1(a). Coupling between the states is driven by fields ω_p, coupling states $|0\rangle$ and $|P\rangle$, and ω_c which couples states $|P\rangle$ and $|1\rangle$ with detunings $\Delta_1 = \omega_p - \omega_{0p}$ and $\Delta_2 = \omega_c - \omega_{p1}$ respectively. The magnitude of the electric dipole coupling is described by the Rabi frequencies $\Omega_p = -\boldsymbol{d}_{0p} \cdot \boldsymbol{\mathcal{E}}_1/\hbar$ and $\Omega_c = -\boldsymbol{d}_{1p} \cdot \boldsymbol{\mathcal{E}}_2/\hbar$.

To describe the three-level system, we utilise the same approach as the two-level

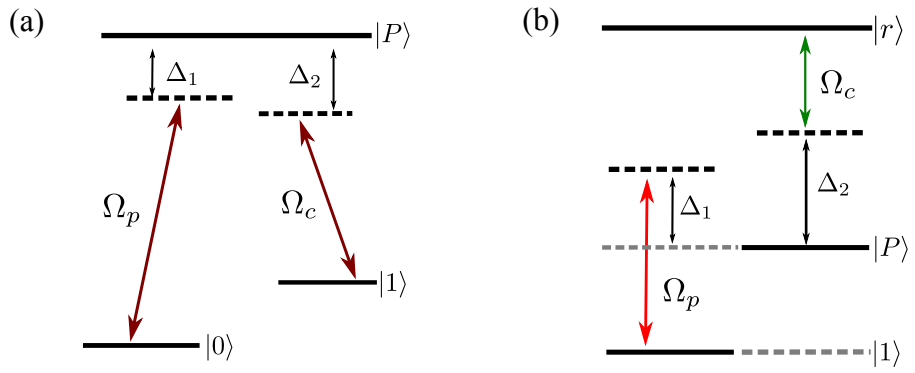

Figure 4.1: Three-level atom schematic for (a) the Λ-configuration and (b) the ladder-configuration.

description by constructing a Hamiltonian using the rotating wave approximation (RWA) for the Λ-configuration [87] and solve it using the time-dependent Schrödinger equation (Eq. 3.3). The total Hamiltonian for the Λ-system is

$$\mathcal{H}_\Lambda = \mathcal{H}_\mathrm{A} + \mathcal{H}_\mathrm{AL}, \tag{4.1}$$

where the unperturbed Hamiltonian $\mathcal{H}_\mathrm{A}$ is given by

$$\mathcal{H}_\mathrm{A} = \hbar\omega_0 \left|0\right\rangle\!\left\langle 0\right| + \hbar\omega_1 \left|1\right\rangle\!\left\langle 1\right| + \hbar\omega_e \left|P\right\rangle\!\left\langle P\right|, \tag{4.2}$$

and the Hamiltonian for the atom-light interaction is given by

$$\mathcal{H}_\mathrm{AL} = \frac{\hbar\Omega_p}{2}\left[e^{-i\omega_p t}\left|1\right\rangle\!\left\langle 0\right| + e^{i\omega_p t}\left|0\right\rangle\!\left\langle 1\right|\right] + \frac{\hbar\Omega_c}{2}\left[e^{-i\omega_c t}\left|1\right\rangle\!\left\langle P\right| + e^{i\omega_c t}\left|1\right\rangle\!\left\langle P\right|\right]. \tag{4.3}$$

By using the rotating wave approximation, the Hamiltonian of the three-level Λ-system is written [87]

$$\mathcal{H}_\Lambda = \frac{\hbar}{2}\begin{pmatrix} \delta & \Omega_p & 0 \\ \Omega_p & -2\Delta & \Omega_c \\ 0 & \Omega_c & -\delta \end{pmatrix}, \tag{4.4}$$

where $\delta = \Delta_1 - \Delta_2$ and $\Delta = \frac{\Delta_1+\Delta_2}{2}$.

If the detuning with respect to the intermediate state $|P\rangle$ is large then spontaneous emission can be minimised. Assuming the excited state $|P\rangle$ is initially unpopulated and $\Omega_{p,c} \ll |\Delta_{1,2}|$, then $|P\rangle$ will remain unpopulated as the system evolves. This

means the change of population of this state is approximately zero ($(\partial/\partial t)c_p(t) = 0$) and the state can be eliminated [88], resulting in an effective two-level system given by Hamiltonian,

$$\mathcal{H}_\Lambda^{\text{eff}} = \frac{\hbar}{2}\begin{pmatrix} \Delta_{\text{eff}} & \Omega_R \\ \Omega_R & -\Delta_{\text{eff}} \end{pmatrix}, \tag{4.5}$$

where $\Omega_R = \frac{\Omega_1\Omega_2}{2\Delta}$ is the effective Rabi frequency and $\Delta_{\text{eff}} = \delta + \Delta_{AC}^{|0\rangle} + \Delta_{AC}^{|1\rangle}$ is the AC Stark shift due to the light shift induced by the electric dipole interaction with the detuned beam.

The reduced matrix elements can be used to calculate the Rabi frequency (Ω_1, Ω_2) of each laser and hence the total Rabi frequency (Ω_R) of the two-photon process,

$$\Omega_R = \frac{\Omega_1\Omega_2}{2\Delta}, \tag{4.6}$$

and the AC Stark shift of one state caused by the laser field on the other i.e. the off-resonant coupling,

$$\Delta_{AC}^{|0\rangle} = \frac{\Omega_1^2}{4\Delta} + \frac{\Omega_2^2}{4(\Delta - \nu_{\text{hfs}})}, \tag{4.7a}$$

$$\Delta_{AC}^{|1\rangle} = \frac{\Omega_2^2}{4\Delta} + \frac{\Omega_1^2}{4(\Delta + \nu_{\text{hfs}})}, \tag{4.7b}$$

where ν_{hfs} is the ground state hyperfine splitting equal to 9.192 GHz in caesium [89].

To include spontaneous emission in the Λ-configuration we use the same approach as the two-level case by using the density matrix formalism. The density matrix for the three-level system given by,

$$\hat{\rho} = \begin{pmatrix} \rho_{00} & \rho_{01} & \rho_{0p} \\ \rho_{10} & \rho_{11} & \rho_{1p} \\ \rho_{p0} & \rho_{p1} & \rho_{pp} \end{pmatrix}. \tag{4.8}$$

The evolution of the system given by

$$\frac{d\hat{\rho}}{dt} = -\frac{i}{\hbar}\left[\hat{\mathcal{H}}_\Lambda, \hat{\rho}\right] + \mathcal{L}(\rho), \tag{4.9}$$

with $\mathcal{L}(\rho)$ the Lindblad operator describing the decay of the system given by [90]

$$\mathcal{L}(\rho) = \begin{pmatrix} \Gamma_1\rho_{11} & -\frac{1}{2}\Gamma_1\rho_{01} & -\frac{1}{2}\Gamma_p\rho_{1p} \\ -\frac{1}{2}\Gamma_1\rho_{10} & -\Gamma_1\rho_{11} + \Gamma_p\rho_{pp} & -\frac{1}{2}(\Gamma_1 + \Gamma_p)\rho_{1p} \\ -\frac{1}{2}\Gamma_p\rho_{p0} & -\frac{1}{2}(\Gamma_1 + \Gamma_p)\rho_{p1} & -\Gamma_p\rho_{pp} \end{pmatrix}, \tag{4.10}$$

where Γ_p is the decay rate from $|P\rangle$ and Γ_1 is the decay rate from $|1\rangle$, given by operators $c_p = \sqrt{\Gamma_p}\,|0\rangle\langle p|$ and $c_1 = \sqrt{\Gamma_1}\,|p\rangle\langle 1|$ respectively.

4.1.1 Three-level Ladder Configuration

The atomic system in the ladder configuration differs from the Λ-system by the way the energy levels and their detuning's are defined. A schematic for the ladder configuration is given in Fig. 4.1(b) where the states $|1\rangle$, $|P\rangle$ and $|r\rangle$ are addressed by two light fields with frequencies ω_{1p} and ω_{pr} that couple the states $|1\rangle \rightarrow |P\rangle$, and $|P\rangle \rightarrow |r\rangle$ respectively. The Hamiltonian for the ladder configuration is the same as that for the Λ system given by Eq. 4.4 with the total detunings now defined by $\delta = \Delta_1 + \Delta_2$ and $\Delta = \frac{\Delta_1 - \Delta_2}{2}$, to account for the different sign of the detuning Δ_2.

The intermediate state can also be eliminated in the ladder configuration in the same way as the Λ configuration, by assuming the detuning from this state is large enough that it remains unpopulated with time, to approximate an effective two-level system described by Eq. 4.5 with $\Delta_{\text{eff}} = \Delta_1 + \Delta_2 + \Delta_{AC}^{|1\rangle} - \Delta_{AC}^{|r\rangle}$.

Experimentally the two lowest energy levels represented by $|1\rangle$ and $|P\rangle$ in the above notation are the levels $|1\rangle = \left|6S_{1/2}, F = 4\right\rangle$ and $|P\rangle = \left|6P_{3/2}, F' = 5\right\rangle$ where the hyperfine structure is used. The upper energy level given as $|r\rangle = \left|81D_{5/2}, m_j = 5/2\right\rangle$ is the Rydberg state where the fine structure splitting is sufficient as the hyperfine splitting is not resolvable at this principal quantum number.

4.1.2 Cs Model: Multi-level Atom

In our experiments we use a laser detuned from the D_2 line in caesium which requires us to account for the fact that caesium is a multi-level atom thus we must sum over contributions from all possible excitation paths. In a general multi-level system, there is also coupling between the hyperfine splitting of the intermediate state $|F_e, m_{F_e}\rangle$ to the other states $\left|F_{g,s}, m_{F_{g,s}}\right\rangle$. To include this we have to sum

over all dipole coupled states to find the Rabi frequency,

$$\Omega_R = \sum_{F_e, m_{F_e}} \frac{\Omega^A_{F_g, m_{F_g} \to F_e, m_{F_e}} \Omega^B_{F_s, m_{F_s} \to F_e, m_{F_e}}}{2(\Delta - \nu_{\text{hfs}})}, \tag{4.11}$$

the AC Stark shifts,

$$\Delta^g_{AC} = \sum_{F_e, m_{F_e}} \frac{(\Omega^A_{F_g, m_{F_g} \to F_e, m_{F_e}})^2}{4\Delta} + \sum_{F_e, m_{F_e}} \frac{(\Omega^B_{F_g, m_{F_g} \to F_e, m_{F_e}})^2}{4(\Delta - \nu_{\text{hfs}})}, \tag{4.12a}$$

$$\Delta^s_{AC} = \sum_{F_e, m_{F_e}} \frac{(\Omega^B_{F_s, m_{F_s} \to F_e, m_{F_e}})^2}{4\Delta} + \sum_{F_e, m_{F_e}} \frac{(\Omega^A_{F_s, m_{F_s} \to F_e, m_{F_e}})^2}{4(\Delta + \nu_{\text{hfs}})}, \tag{4.12b}$$

and scattering rate

$$\Gamma_{sc} = \gamma t_\pi \Bigg[\sum_{F_e, m_{F_e}} \frac{(\Omega^A_{F_g, m_{F_g} \to F_e, m_{F_e}})^2}{4\Delta} + \sum_{F_e, m_{F_e}} \frac{(\Omega^A_{F_g, m_{F_g} \to F_e, m_{F_e}})^2}{4(\Delta - \nu_{\text{hfs}})^2} - \sum_{F_e, m_{F_e}} \frac{(\Omega^B_{F_s, m_{F_s} \to F_e, m_{F_e}})^2}{4(\Delta + \nu_{\text{hfs}})^2} + \sum_{F_e, m_{F_e}} \frac{(\Omega^B_{F_s, m_{F_s} \to F_e, m_{F_e}})^2}{4\Delta} \Bigg], \tag{4.13}$$

where Δ is the detuning with respect to the centre of mass of the intermediate state, $t_\pi = \pi/\Omega_{F_s, m_{F_s} \to F_s, m_{F_s}}$, ν_{hfs} is the hyperfine splitting and $\Omega^i_{F_{g,s}, m F_{g,s} \to F_e, m_{F_e}}$ are the Rabi frequencies of the lasers $i = \{A, B\}$ for the transitions between hyperfine levels.

Based on simulations carried out using MATLAB, we set the detuning $\Delta/2\pi = -88$ GHz as this value of Δ is far detuned from the intermediate state $|e\rangle$ with a low scattering rate Γ_e. For Raman transitions driven by a laser with 45 μW of power and beam waist, ω_0= 4.5 μm, the estimated Rabi frequency $\Omega_R/2\pi = 1.91$ MHz and the AC Stark shift $\Delta_{AC}/2\pi = -1.17$ MHz. Fig. 4.2 shows the results of the simulation.

The simulation characterises the strength of the interaction of caesium with the near-resonant laser using the reduced dipole matrix elements with the Wigner 3-j and 6-j symbols [91, 92] to produce a result that is only dependent on the quantum number j and j' for the ground and excited states respectively, summed over all f-levels. We can also set the polarisation of the Raman lasers which we choose to be equal to one another with equal strength. The polarisation is set to σ^+ circular

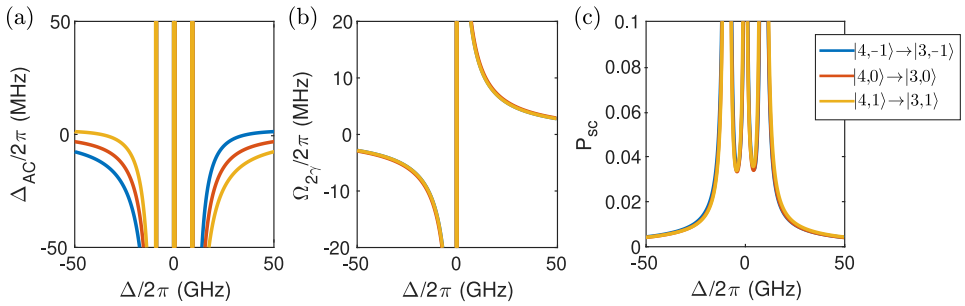

Figure 4.2: Multi-level model of caesium atom showing (a) AC Stark shift (b) Rabi frequency, and (c) excited state scattering rate, as a function of the centre of mass detuning Δ.

polarisation, which gives a possible excitation pathway from $|F = 4, m_F = 0\rangle \rightarrow |F = 3, m_F = 0\rangle$ via the states $|F_e = 4, m_{F_e} = 1\rangle$ and $|F_e = 3, m_{F_e} = 1\rangle$.

4.2 Electromagnetically Induced Transparency (EIT)

In this section we discuss the emergence of *electromagnetically induced transparency* (EIT), using the Λ configuration to do so. The Λ configuration is again illustrated in Fig. 4.3(a) and we introduce the terms probe and coupling to describe the lasers with Rabi frequencies Ω_p and Ω_c respectively. This notation is typically used when discussing the phenomenon of EIT.

The evolution of the Λ system is described by the Hamiltonian given Eq. 4.4. If we consider the case where there are small and equal detunings $\Delta_1 = \Delta_2 = \Delta$, then we have the exact two-photon resonance ($\delta = 0$), and we impose the condition $\Delta \leq \Omega_p, \Omega_c$, the Hamiltonian becomes

$$\mathcal{H} = -\frac{\hbar}{2}\begin{pmatrix} 0 & \Omega_p & 0 \\ \Omega_p & -2\Delta & \Omega_c \\ 0 & \Omega_c & 0 \end{pmatrix}. \tag{4.14}$$

By diagonalising the above Hamiltonian we obtain the eigenvalues

$$\lambda_0 = 0, \qquad \lambda_\pm = \Delta \pm \sqrt{\Omega_p^2 + \Omega_c^2 + \Delta^2}, \tag{4.15}$$

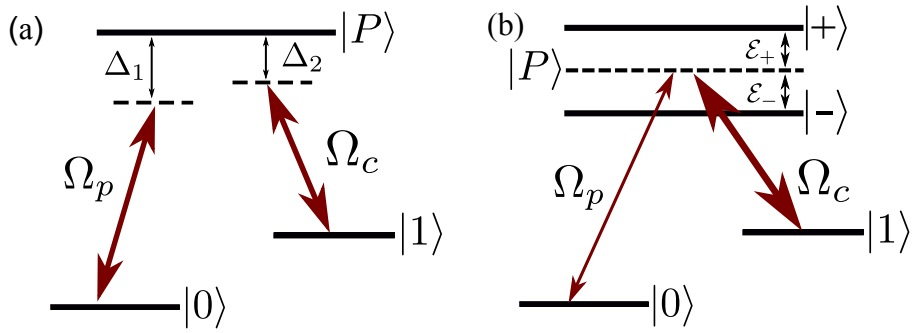

Figure 4.3: (a) The 3-level Λ-system with probe laser Ω_p coupling $|g\rangle$ and $|e\rangle$ detuned by Δ_p, and coupling laser Ω_c coupling $|s\rangle$ and $|e\rangle$ detuned by Δ_c. (b) In the strong coupling limit $\Omega_c \gg \Omega_p$, the energy level $|e\rangle$ is split and shifted by $\mathcal{E}_\pm$ to make the probe laser transparent to the atom.

corresponding to the eigenstates [65]

$$|+\rangle = \sin\theta \sin\phi\,|0\rangle + \cos\phi\,|P\rangle + \cos\theta \sin\phi\,|1\rangle\,, \tag{4.16a}$$

$$|D\rangle = \cos\theta\,|0\rangle - \sin\theta\,|1\rangle\,, \tag{4.16b}$$

$$|-\rangle = \cos\theta \sin\phi\,|0\rangle - \sin\phi\,|P\rangle + \cos\theta \sin\phi\,|1\rangle\,, \tag{4.16c}$$

where the mixing angles are

$$\tan\theta = \frac{\Omega_p}{\Omega_c}, \qquad \phi = \frac{\sqrt{\Omega_p^2 + \Omega_c^2}}{\Delta}. \tag{4.17}$$

We can see from Eqs. 4.16 that the zero energy eigenstate $|D\rangle$ does not contain the intermediate state $|P\rangle$, which decays by emitting a spontaneous photon with rate Γ_p. The state $|D\rangle$ is called the *dark state* as there is no possibility of excitation to the state $|P\rangle$. In contrast the states $|\pm\rangle$ are known as *bright states* as they contain a contribution from the bare atomic states $|0\rangle$, $|1\rangle$ and $|P\rangle$ such that they are shifted in energy by

$$\mathcal{E}_\pm = \frac{\hbar}{2}\left(\Delta \pm \sqrt{\Delta^2 + \Omega_p^2 + \Omega_c^2}\,\right). \tag{4.18}$$

This leads to what is known as Autler-Townes splitting [78] as shown in Fig. 4.3(b). In the strong coupling regime $\Omega_c \gg \Omega_p$, Γ_p, and on resonance ($\Delta = 0$) the eigenstates are

$$|D\rangle = |0\rangle\,, \qquad |\pm\rangle = \frac{|1\rangle \pm |0\rangle}{\sqrt{2}}, \tag{4.19}$$

showing that the dark state is identical to the state $|0\rangle$ and no excitation can occur. Similarly the bright states have excitation probability amplitudes with equal but opposite signs, giving rise to destructive interference of the excitation pathways. This makes the probe laser transparent to the atomic medium and the system stays in the dark state. This coherent phenomenon is known as electromagnetically induced transparency (EIT).

4.3 Summary

The model of the three-level atom and the interaction with two coherent light sources describes the underlying mechanisms used to perform fast optical rotations for the ground state Raman transitions and Rydberg excitations using the Λ and ladder configurations respectively. It also highlighted the way to minimise decoherence mechanisms such as spontaneous emission through adiabatic elimination of the excited state for each system, to achieve large two-photon Rabi frequencies. Studying the three-level system also allowed us to realise the quantum interference effect of electromagnetically induced transparency when the two-photon resonance condition $\Delta_p = \Delta_c = 0$ is satisfied.

Chapter 5

Rydberg Atoms

This chapter highlights the key properties of Rydberg atoms required to interpret the results presented in this thesis. Rydberg atoms are atoms that have been excited to a state with a high principal quantum number n, and as a result exhibit exaggerated properties that make them of interest for quantum information processing. Of particular interest are Rydberg-Rydberg interactions and dipole blockade which are key components in many quantum information processes with Rydberg atoms.

5.1 Rydberg Atom Properties

Alkali Rydberg atoms can be described by the Bohr model of the atom, with a single valence electron orbiting a positive core with a $-1/r$ Coulomb potential at long range [93]. The binding energy of the electron to the core for a Rydberg state with principal quantum number $n \gg 1$, orbital angular momentum l and total angular momentum j is given by [94, 95]

$$E_{n,l,j} = -\frac{\mathrm{Ry}}{n^{*2}}, \tag{5.1}$$

where Ry is the Rydberg constant, $n^* = n - \delta_{n,l,j}$ is the effective principal quantum number, and $\delta_{n,l,j}$ is the quantum defect. The quantum defect accounts for the fact

that an electron with an angular momentum $l \leq 3$ can penetrate into the electronic core, thus increasing the effective charge seen by the electron and lowering the binding energy. The quantum defect is given by the expansion,

$$\delta_{n,l,j} = \delta_0 + \frac{\delta_2}{n^{*2}} + \frac{\delta_4}{n^{*4}} + \dots \ . \tag{5.2}$$

The value of the quantum defect is species and quantum number dependent, and has been measured for caesium using precision spectroscopy [96–99]. Typically, for heavy alkali metals $\delta_{l\geq 3} \approx 0$ [94].

The Rydberg constant for caesium is Ry $=$ 109 736.862 7339 cm^{-1} [99] and the most recently determined values for the quantum defects of the $nD_{5/2}$ Rydberg state used in this thesis are $\delta_0 = 2.4663144(6)$ and $\delta_2 = 0.001381(15)$ [99].

Atoms excited to Rydberg states have interesting features that make them useful for study. The features of particular interest to this thesis come from the large orbital radius which scales as $\langle r \rangle \propto n^{*2}a_0$, with a_0 the Bohr radius, causing a strong overlap between the wavefunctions and electric dipole moment ($\boldsymbol{\mu} = -e\mathbf{r}$) of the Rydberg states. The resulting dipole matrix elements $d = \langle n, l, j, m_j | \, \boldsymbol{\mu} \, | n', l', j', m_j' \rangle \propto n^{*2}$ coupling neighbouring Rydberg states are large making the Rydberg states very sensitive to electric fields, with a polarisability, $\alpha \propto n^{*7}$ [94]. A summary of the main Rydberg features and their scaling laws with respect to the effective principal quantum number is given in Table 5.1.

Additionally, Rydberg states have very long radiative lifetimes, $\tau \propto n^{*3}$, making them useful for performing quantum gates. The Rydberg state lifetime is dependent on the radiative decay due to spontaneous emission to low-lying states (τ_0), and black-body radiation (BBR) due to finite temperature T:

$$\tau_{\mathrm{BBR}} = \frac{3\hbar n^2}{4\alpha^3 k_B T} \tag{5.3}$$

where α is the fine structure constant. The BBR dominates decay to close-lying states with strong electric dipole transitions. This results in a total decay rate [100],

$$\Gamma = \frac{1}{\tau_0} + \frac{1}{\tau_{\mathrm{BBR}}}, \tag{5.4}$$

Property	Scaling
Binding Energy	n^{*-2}
Level Spacing	n^{*-3}
Orbital Radius	n^{*2}
Radiative Lifetime	n^{*3}
Polarisability	n^{*7}
Van der Waals coefficient	n^{*11}

Table 5.1: Scaling laws for properties of the Rydberg states with respect to the effective principal quantum number n^* [42].

with the effective lifetime $\tau_{\text{eff}} = 1/\Gamma$.

In the experiments presented in his thesis, the Rydberg state of interest is the $81D_{5/2}$ state which has an effective lifetime of 163 μs at 300 K [101], an increase of four orders of magnitude over the lifetime of 30 ns of $6P_{3/2}$ state used for cooling [89].

5.2 Rydberg Atom Interactions

The large dipole moment exhibited by Rydberg atoms leads to a strong interaction between them. Consider two atoms A and B prepared in the Rydberg state $|r\rangle = |n, l, j, m_j\rangle$, separated by a distance $\mathbf{R}$ as illustrated in Fig. 5.1(a). The atoms have dipole moments $\boldsymbol{\mu}_{A,B}$ associated with the transitions between $|r\rangle$ and $|r'\rangle$ and $|r''\rangle$ respectively. As Rydberg atoms are neutral, they interact via dipole-dipole coupling, described in atomic units by [95],

$$V(\mathbf{R}) = \frac{\boldsymbol{\mu}_A \cdot \boldsymbol{\mu}_B}{R^3} - \frac{3(\boldsymbol{\mu}_A \cdot \mathbf{R})(\boldsymbol{\mu}_B \cdot \mathbf{R})}{R^5}. \tag{5.5}$$

If we take $\mathbf{R}$ along the z-axis ($\theta = 0$), the dipole-dipole interaction reduces to

$$V(R) = \frac{\mu_{A-}\mu_{B+} + \mu_{A+}\mu_{B-} - 2\mu_{Az}\mu_{Bz}}{R^3}, \tag{5.6}$$

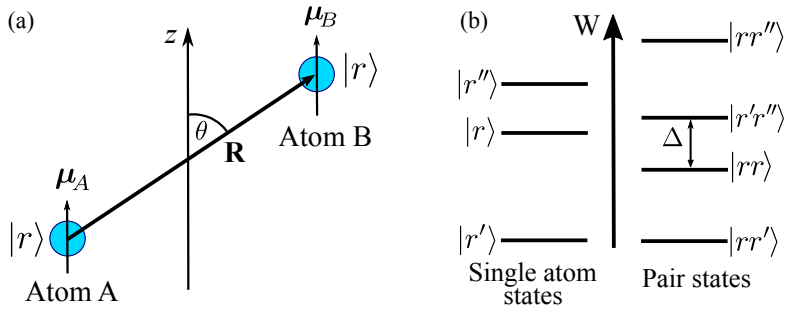

Figure 5.1: (a) Two Rydberg atoms A and B with dipoles $\boldsymbol{\mu}_A$ and $\boldsymbol{\mu}_B$ respectively, separated by $\mathbf{R}$ with angle θ w.r.t. the quantisation axis z. (b) Transformation from the single atom basis with Rydberg states $|r\rangle$, $|r'\rangle$ and $|r''\rangle$ to the pair basis shows near-resonant states coupled by the dipole-dipole interaction with an energy defect Δ between $|rr\rangle$ and $|r'r''\rangle$.

where $\mu_{i,q}$ is the dipole operator for atom $i = \{A, B\}$ with transitions $q = \{-, z, +\}$. These transitions describe the change in the magnetic quantum number with $\Delta m_j = \pm 1$ for $\sigma^{\pm}$ - polarisation pathways and $\Delta m_j = 0$ for a π - polarisation pathway. The total angular moment along the z-axis is conserved $M = m_A + m_B$ in this geometry, despite the individual atoms' quantum number changing by ± 1 or 0 [102].

To understand the energy shift that arises as a result of the dipole-dipole interaction we require a basis shift from single atom to pair states, as illustrated in Fig. 5.1(b). The initial pair state $|rr\rangle$ is coupled to a state $|r'r''\rangle$ by $V(R)$ which has an energy defect given by,

$$\Delta = W_{|r'\rangle} + W_{|r''\rangle} - 2W_{|r\rangle}, \tag{5.7}$$

representing the energy difference of the pair states at infinite separation. In the basis $\{|rr\rangle, |r'r''\rangle\}$, the Hamiltonian describing the dipole-dipole interaction is

$$\mathcal{H} = \begin{pmatrix} 0 & V(R) \\ V(R) & \Delta \end{pmatrix}, \tag{5.8}$$

which has eigenvalues,

$$\lambda_{\pm} = \frac{\Delta \pm \sqrt{\Delta^2 + 4V(R)^2}}{2}, \tag{5.9}$$

showing that the energy of the pair state is dependent on the separation of the two atoms.

Two cases of interest arise from the spatial dependence of the atoms:

1. $V(R) \ll \Delta$: this limit is the long-range van der Waals (vdW) regime with the interaction scaling as
$$\Delta W = -\frac{V(R)^2}{\Delta} = -\frac{C_6}{R^6}. \tag{5.10}$$
The interaction here is dependent on the coefficient C_6 which scales proportional to n^{*11} as $V(R) \propto \mu^2 \propto n^{*4}$ and the energy defect $\Delta \propto n^{*-3}$. Note that in this van der Waals regime the sign of the interaction is determined by the sign of the energy defect.

2. $V(R) \gg \Delta$: this limit is the short-range resonant dipole-dipole regime. The strength of the interaction is given by
$$\Delta W = \pm V(R) = \pm\frac{C_3}{R^3}. \tag{5.11}$$
In this regime the interaction depends on the coefficient C_3 which scales $\propto n^{*4}$. Using an external electric field it is possible to tune $\Delta \approx 0$ and a Förster resonance is realised [94, 103].

The transition between the dipole and van der Waals regimes occurs at the van der Waals radius, occurring when $V(R_{\text{vdW}}) = \Delta$, where $R_{\text{vdW}} = \sqrt[6]{|C_6/\Delta|} \propto n^{*7/3}$.

5.2.1 Angular Dependence

Above we assumed that the dipoles were aligned with the z-axis ($\theta = 0$), however, in practice this is generally not the case. Accounting for this the dipole-dipole coupling written as a function of both θ and R is [104]

$$\begin{aligned} V(R,\theta) = &\frac{\mu_{A-}\mu_{B+} + \mu_{A+}\mu_{B-} + (1 - 3\cos^2\theta)\mu_{Az}\mu_{Bz}}{R^3} \\ &+ \frac{3/2\sin^2\theta(\mu_{A+}\mu_{B+} + \mu_{A+}\mu_{B-} + \mu_{A-}\mu_{B+} + \mu_{A-}\mu_{B-})}{R^3} \\ &+ \frac{3/\sqrt{2}\sin\theta\cos\theta(\mu_{Az}\mu_{B+} + \mu_{Az}\mu_{B-} + \mu_{A+}\mu_{Bz} + \mu_{A-}\mu_{Bz})}{R^3}. \end{aligned} \tag{5.12}$$

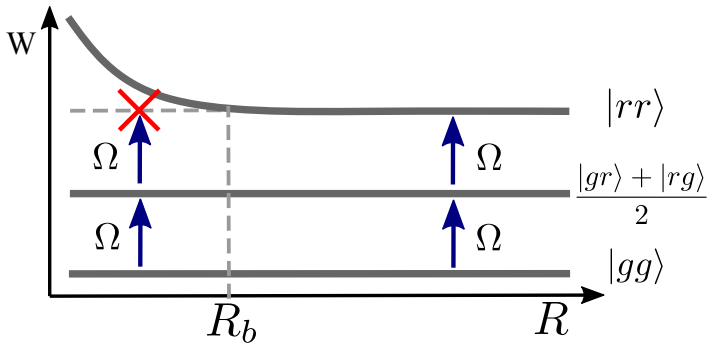

Figure 5.2: Rydberg dipole blockade. For two atoms at a large separation R both can be excited to the Rydberg pair state $|rr\rangle$ by pulse Ω. At a separation $R < R_b$ the blockade radius, the blockade effect prevents the excitation of the pair state.

For $\theta \neq 0$ the total angular momentum M of the initial pair state is no longer conserved allowing states of different M to be coupled together.

5.3 Dipole Blockade

To further explore the effect that atom separation plays in excitations to Rydberg states, we consider an excitation laser with Rabi frequency Ω which drives a transition between $|g\rangle \rightarrow |r\rangle$. As illustrated in Fig. 5.2, this can cause excitation to the singly excited Rydberg states $|gr\rangle$ or $|rg\rangle$, that is independent of the atoms' separation.

In the case of double excitation, if one atom is excited to $|r\rangle$ the energy required to excite the other atom to $|r\rangle$ is dependent on the proximity of this atom to the first. When the atoms are far apart the energy shift is negligible and the atoms can be excited to the doubly excited Rydberg state $|rr\rangle$. When the energy shift is greater than the coupling field $\Delta W \gg \hbar\Omega$ the excitation to the doubly excited state is forbidden. This effect is called *Rydberg blockade* and occurs when both atoms are within the blockade radius which is given by,

$$R_b = \sqrt[6]{\frac{|C_6|}{\Omega}}. \tag{5.13}$$

The Rydberg blockade radius scales as $R_b \propto \sqrt[6]{C_6} \propto n^{*11/6}$, which means using a

higher principal quantum number increases the blockade radius.

Placing the atoms at a separation that is within the blockade radius and applying an excitation pulse Ω that simultaneously addresses both atoms, it is not possible to determine which atom has been excited to the Rydberg state. This means is it equally probable to make the states $|gr\rangle$ and $|rg\rangle$, creating an effective superposition of both states

$$|\mathcal{W}\rangle = \frac{1}{\sqrt{2}}(|gr\rangle + |rg\rangle). \tag{5.14}$$

This can be used to create a maximally entangled symmetric state with a coupling enhanced by a factor of $\sqrt{2}$, resulting in a collective Rabi frequency of $\sqrt{2}\Omega$ compared to the single atom case [73, 74]. This has previously been demonstrated in our experiment with the Rydberg blockade mechanism combined with a two-photon Raman transition to create ground state entanglement [47].

The Rydberg blockade can be extended to the case of N atoms located within the blockade sphere, of volume $V = \frac{4}{3}\pi R_b^3$. The system with N atoms shares a collective oscillation between the collective ground state $|G\rangle = |gg\ldots g\rangle$ and a collective entangled state [94]

$$|\mathcal{W}_c\rangle = \frac{1}{\sqrt{N}} \sum_{j=1}^{N} |gg\ldots r_j \ldots g\rangle\,, \tag{5.15}$$

where only one of the N atoms is excited to the Rydberg state $|r\rangle$. The Rabi frequency of the collective oscillation is $\sqrt{N}\Omega$, demonstrating the accessibility to a high degree of entanglement for a many body system [30, 46, 105, 106].

5.4 Experiment Implementation

In this thesis the Rydberg state of interest is $\left|81D_{5/2}, m_j = 5/2\right\rangle$, with the $m_j = 5/2$ state chosen to give the strongest coupling to the ground state in order to achieve a large Rabi frequency for coherent Rydberg excitation. The configuration of the experiment leads to an angle of $\theta = \pi/2$ leading to a significant anisotropic interaction compared to the value along z ($\theta = 0$).

For the pair state $|rr\rangle = \left|81D_{5/2}\ 81D_{5/2}\right\rangle$ the main contribution to the dipole-dipole interaction comes form the pair state $|r'r''\rangle = \left|85P_{3/2}\ 76F\right\rangle$, which has energy defect $\Delta/2\pi = 0.74$ GHz and coefficient $C_6 = -1626$ GHz.μm^6 [101]. The atom-pair state generates strong repulsive interactions with a van der Waals radius of ~ 3.6 μm. The atoms in the experiment are separated by ~ 5 μm such that we work in the van der Waals regime.

5.5 Summary

Rydberg atoms and their properties are a useful tool for quantum information processing using neutral atoms. They facilitate two or more qubit interactions over relatively long distances through the long-range van der Waals interaction with lifetimes that enable quantum gates to be implemented. Further to this the collective Rydberg excitation shared between atoms in the blockade sphere offers a practical route to generate multi-qubit entanglement.

Chapter 6

CNOT Gate

As discussed in Chapter 5, Rydberg atoms have a high principal quantum number, n, which means they have strong dipole-dipole interactions over length scales of $R \leq 10$ μm. At this separation they are within the Rydberg blockade radius such that the excitation of more than one atom to the Rydberg state is strongly suppressed [45]. For simultaneous excitation of N atoms within a blockade sphere, collective effects lead to a $\sqrt{N}$ scaling in pulse area for creating a single collective excitation [50]. If N is unknown or fluctuates (e.g. Poisson loading of an atomic ensemble) high fidelity gate operations are challenging [32, 51].

An approach to overcome this limit is to implement gates using sequential pulses applied to each qubit [87, 107] however this is limited by the requirement for the control atom to remain in the Rydberg level while operations are performed on all other qubits, limiting the attainable fidelity. One method to circumvent the $\sqrt{N}$ scaling was proposed by Müller *et al.* [52] using electromagnetically induced transparency (EIT) to allow a single control qubit to couple to N neighbouring target qubits.

This protocol provides a scalable approach to performing entanglement of large atomic ensembles using a single control atom whilst circumventing the challenges of the collective Rabi frequency. The resulting gate is therefore robust against number fluctuations and acts as a single-atom transistor to amplify the quantum

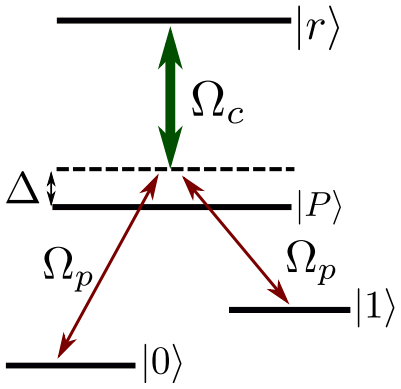

Figure 6.1: Four-level energy level schematic for EIT. The states $|0\rangle$ and $|1\rangle$ are off-resonantly coupled to $|P\rangle$ with detuning Δ and equal Rabi frequencies Ω_p. The state $|r\rangle$ is coupled with Rabi frequency $\Omega_c \gg \Omega_p$ to the state $|P\rangle$ such that $|r\rangle$ is in two-photon resonance with $|0\rangle$ and $|1\rangle$. In this case the Raman transfer between states $|0\rangle$ and $|1\rangle$ is inhibited as the conditions for EIT are satisfied.

state of an atom onto an atomic ensemble. This provides a route to creating useful entangled states for quantum information processing (QIP), high precision measurements beyond the standard quantum limit [53], as well as demonstrating the crucial gate scheme for implementing topological error correction using surface codes in atomic arrays [54].

6.1 EIT in a 4-Level System

In Sec. 4.2 we discussed the emergence of EIT in the three-level Λ-configuration. Here we extend this discussion to include a fourth level in the atomic configuration and will detail how a pair of dark states emerge in this system. We will then describe how the dark states can be used to implement a CNOT^N gate when using Rydberg atoms as was proposed by Müller *et al.* [52].

The four-level configuration is shown in Fig. 6.1 where we have introduced the state $|r\rangle$ which is coupled to the state $|P\rangle$ by a strong coupling field with Rabi frequency Ω_c at a detuning Δ_c from the $|P\rangle \rightarrow |r\rangle$ transition. If we assume the states $|0\rangle$ and $|1\rangle$ are off-resonantly coupled to $|P\rangle$ with equal Rabi frequencies Ω_p

at a single photon detuning from $|P\rangle$ of $\Delta = (\Delta_1 + \Delta_2)/2$, then the Hamiltonian for the four-level system is given by [52],

$$\mathcal{H} = \hbar \begin{pmatrix} 0 & 0 & \Omega_p(t)/2 & 0 \\ 0 & -\delta & \Omega_p(t)/2 & 0 \\ \Omega_p(t)/2 & \Omega_p(t)/2 & -\Delta & \Omega_c/2 \\ 0 & 0 & \Omega_c/2 & -(\Delta + \Delta_c + V) \end{pmatrix}, \tag{6.1}$$

where $\delta = \Delta_1 - \Delta_2$ is the two-photon detuning of $|0\rangle \rightarrow |1\rangle$, and the (van der Waals) interaction energy V describes the interaction between the Rydberg states of the control and target atoms.

In a similar way to the three-level case discussed in Sec. 4.1, the intermediate state $|P\rangle$ can also be eliminated in the four-level system. In this case we work in the limit that $\Delta \gg \Omega_c > \Omega_p$, $\Delta_c = -\Delta$ and $V = 0$ such that the state $|P\rangle$ remains unpopulated as the system evolves, leading to the effective Hamiltonian [52],

$$\mathcal{H}/\epsilon = x(t)^2 \, |+\rangle\langle+| + |r\rangle\langle r| + x(t) \left(|+\rangle\langle r| + |r\rangle\langle+|\right), \tag{6.2}$$

where $\epsilon = \hbar\Omega_c^2/(4\Delta)$ is the AC Stark shift due to the coupling laser Ω_c, $x(t) = \sqrt{2}\Omega_p(t)/\Omega_c$ is the re-scaled, dimensionless Raman laser Rabi frequency and the states $|\pm\rangle = \left(|0\rangle \pm |1\rangle\right)/\sqrt{2}$. As a result of the interaction with the coupling laser Ω_c, the state $|P\rangle$ is shifted in energy by ϵ such that the resonance condition must satisfy $\Delta_{\text{eff}} = \delta + \Delta + \epsilon$ to observe full population transfer between the states $|0\rangle$ (or $|1\rangle$) and $|r\rangle$. This energy scaling is important in the blocking mechanism in the CNOT^N gate protocol as will be discussed below.

Working in the limit of the strong coupling regime, i.e. $x(t) \ll 1$, and assuming the two-photon resonance condition is satisfied ($\delta = \Delta$), the coupling laser causes an energy shift ϵ such that the two-photon resonance condition is broken and the states $|0\rangle$ and $|1\rangle$ are no longer coupled. In this case the Hamiltonian describes the EIT scenario for the four-level system [52] and produces two zero-energy dark states,

$$\begin{aligned} |d_1\rangle &= |-\rangle, \\ |d_2\rangle &= (1 + x(t)^2)^{-1/2}[|+\rangle - x(t)\,|r\rangle]. \end{aligned} \tag{6.3}$$

These dark states are key components of the CNOT^N gate discussed in the next section.

6.2 CNOT^N Gate Protocol

The presence of EIT in the four-level scheme described in the previous section can be combined with the Rydberg blockade effect to realise a CNOT^N gate protocol [52]. This gate protocol is unique as the effect of EIT is independent of the number of atoms present such that a single control atom can be used to influence many target atoms. Whilst this approach was originally proposed in the context of atomic ensembles, the residual interaction between Rydberg states in the target ensemble requires further consideration and judicious choice of Rydberg state to obtain high fidelity performance.

In the following discussion we will consider spatially separated target qubits in an atomic array as it is easy to engineer strong control-target qubits whilst suppressing target-target qubit interactions in this case. Practically this can be achieved through geometric positioning of the atoms to ensure the target-target spacing is larger than the control-target spacing, or through the use of different Rydberg states for the control and target atoms [108].

The CNOT^N gate protocol is illustrated in Fig. 6.2, where an array of atoms are trapped with a spacing such that they are within the Rydberg blockade radius allowing a single control atom to effect multiple target atoms simultaneously. The control atom has qubit states $|1\rangle$ and $|0\rangle$ which is coupled to the Rydberg state $|r\rangle$ with a two-photon Rabi frequency Ω_r. The target atoms have qubit states $\left|0^N\right\rangle \equiv \otimes_{k=1}^{N} |0\rangle_k$ and $\left|1^N\right\rangle \equiv \otimes_{k=1}^{N} |1\rangle_k$, where k is the index for the k-th of N target atoms, which are off-resonantly coupled with to $|P\rangle$ with detuning Δ by the Raman lasers Ω_p. A second laser with Rabi frequency Ω_c couples $|r\rangle$ to $|P\rangle$ such that the qubit states $\left|1^N\right\rangle$ and $\left|0^N\right\rangle$ are in two-photon resonance with $|r\rangle$.

The pulse sequence used to perform the CNOT^N gate is shown in Fig. 6.2(b): first

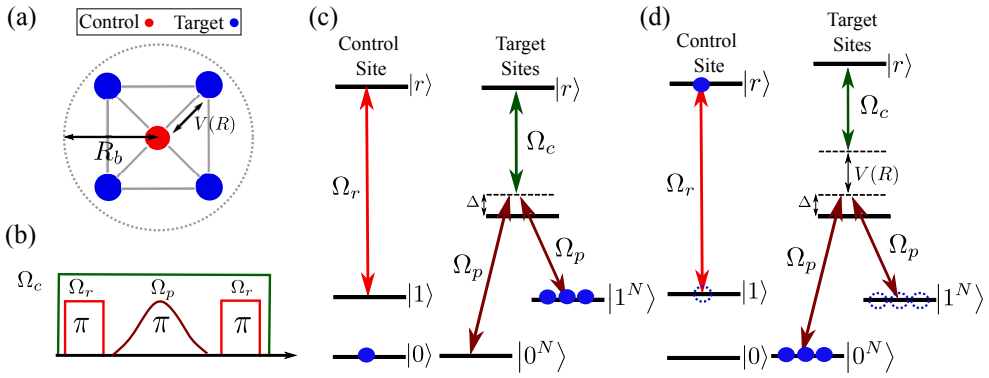

Figure 6.2: The CNOT^N gate protocol. (a) An array of trapped atoms separated such that they are within the Rydberg blockade radius R_b with interaction $V(R) > \epsilon$. A single control atom (red) has the potential to effect multiple target atoms (blue). (b) The sequence of laser pulses acting on the atoms to perform the CNOT^N gate. (c) Energy level structure for the control and target atoms illustrating when the EIT condition is satisfied and (d) when the EIT condition is broken. These operations combine to realise a CNOT^N gate.

there is a π-pulse that acts on the control atom, then a smooth Raman π-pulse $\Omega_p(t)$ with $\int_0^T \Omega_p^2(t)/(2\Delta)\ \mathrm{d}t = \pi$ acts on the target atoms and finally a second π-pulse is applied to the control atom. This pulse sequence is used to block or enable transfer of the target atoms depending on the initial state of the control atom.

Blocked transfer of the target atoms

If the control atom is initially in state $|0\rangle$, as shown in Fig. 6.2(c), the first π-pulse has no effect on the control atom. During the smooth Raman π-pulse, the evolution of the target atoms is described by the four-level EIT scenario described in Sec. 6.1, i.e. the k-th atom of the target array will follow the dark state

$$|D\rangle_k = \frac{1}{\sqrt{2}}\left[|d_1\rangle_k + |d_2\rangle_k\right], \tag{6.4}$$

where $|d_1\rangle_k = |-\rangle$ and $|d_2\rangle_k = (1+x^2)^{-1/2}\left[|+\rangle_k - x\,|r\rangle_k\right]$. For $\Omega_p = 0$, $x(t) = 0$, the dark states at the start and end of the pulse map directly to $|\pm\rangle$. This dark state

evolves adiabatically during the application of the smooth pulse leading to $\left|1^N\right\rangle_k \rightarrow \left|1^N\right\rangle_k$ with no change in the state of the target atoms, creating an effective EIT between the states $\left|1^N\right\rangle_k$ and $|r\rangle_k$. The remaining non-dark states are separated by an energy $\geq \epsilon$ which suppresses non-adiabatic losses proportional to $x(t)^6$ thus enabling high fidelity suppression of transfer from $\left|1^N\right\rangle_k \rightarrow \left|0^N\right\rangle_k$ [52, 109]. If the target atoms are initially in $\left|0^N\right\rangle_k$, the system follows an orthogonal dark state which similarly follows an adiabatic evolution to remain within the state $\left|0^N\right\rangle_k$ at the end of the pulse sequence.

The second π-pulse is then applied to the control atom with no effect, thus performing the step $|0\rangle \left|1^N\right\rangle \rightarrow |0\rangle \left|1^N\right\rangle$.

Enabled transfer of the target atoms

If the control atom is initially in state $|1\rangle$, as shown in Fig. 6.2(d), the application of the first π-pulse excites the control atom to $|r\rangle$. The strong dipole interactions between Rydberg atoms causes the k-th target atom in the array to shift by an energy $V_k > 0$, breaking the two-photon resonance condition between $\left|0^N\right\rangle_k$ and $|r\rangle_k$. This means the Raman beams couple off-resonantly to $|P\rangle_k$ and the smooth pulse drives a two-photon Raman transition from $\left|1^N\right\rangle_k \rightarrow \left|0^N\right\rangle_k$. The final π-pulse on the control atom returns the control atom to $|1\rangle$. This has the net result of $|1\rangle \left|1^N\right\rangle_k \rightarrow |1\rangle \left|0^N\right\rangle_k$.

By preparing the target atoms in qubit states $\left|1^N\right\rangle$ or $\left|0^N\right\rangle$, this method generates a CNOT^N gate with the following operations,

$$\begin{aligned} |0\rangle \left|0^N\right\rangle &\rightarrow |0\rangle \left|0^N\right\rangle, \\ |0\rangle \left|1^N\right\rangle &\rightarrow |0\rangle \left|1^N\right\rangle, \\ |1\rangle \left|0^N\right\rangle &\rightarrow |1\rangle \left|1^N\right\rangle, \\ |1\rangle \left|1^N\right\rangle &\rightarrow |1\rangle \left|0^N\right\rangle. \end{aligned} \tag{6.5}$$

The advantage of this method is the ability to use a single control atom to influence many target atoms without changing the pulse sequence. This arises because

this gate protocol utilises the blockade of the control atom to simply shift the EIT resonance of the target atoms, rather than requiring sequential pulses on each atom [107], or tailored engineering of the collective state evolution [30] to implement multi-qubit gate operations.

6.3 CNOT Gate: Theoretical Fidelity

In our experiment, we consider a single control and target atom only therefore restrict the following discussion to this case. To model the CNOT gate protocol, we simulate the evolution of the four-level system using the T.D.S.E. for the Hamiltonian described by Eq. 6.1 setting $\delta = 0$, $\Delta/2\pi = 1.2$ GHz, $\Delta_c = -\Delta$. The probe pulse shape is defined by

$$\Omega_p(t) = \frac{\Omega_p^{\max}}{2}\left(1 - 2\cos^2(\pi t/\tau)\right), \tag{6.6}$$

where τ is the effective pulse duration, resulting in a pulse area for Raman transfer given by

$$A_\theta = \int_0^\tau \frac{\Omega_p(t)^2}{2\Delta} dt = \frac{3\tau\left|\Omega_p^{\max}\right|^2}{16\Delta}. \tag{6.7}$$

We set, $\Omega_p^{\max}/2\pi = 70$ MHz and $\tau = 0.65$ μs, to obtain a smooth pulse of area $A_\theta = \pi$.

To estimate the fidelity of the gate we initialise the population in state $|1\rangle$ and evaluate the state overlap fidelity $\mathcal{F} = \mathrm{Tr}\left[\sqrt{\sqrt{\rho_t}\rho\sqrt{\rho_t}}\right]^2$, where ρ_t is the ideal density matrix for the target state.

Fidelity on Target Atom

Considering only the target atom so that $V = 0$, we plot the fidelity as a function of Ω_c as shown in Fig. 6.3(a). We see that for $\Omega_c > 2\Omega_p$ the fidelity becomes independent of Ω_c with $\mathcal{F} > 0.98$.

In the limit that $V \neq 0$ the interaction between the Rydberg states of the control and target atoms has to be considered. We plot the fidelity of the transfer between

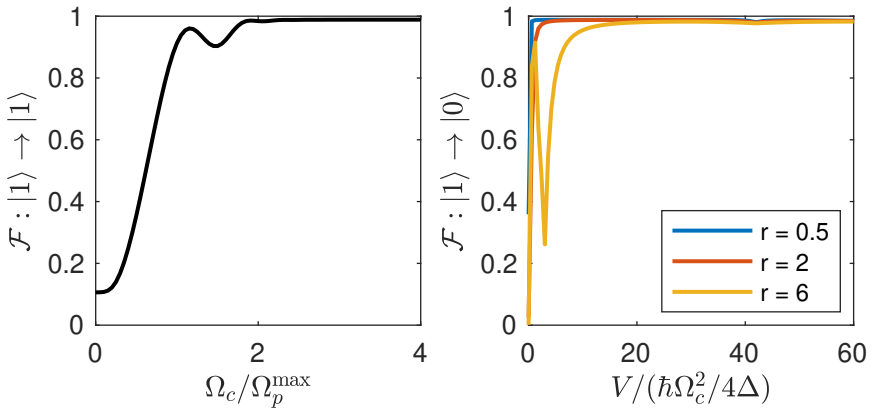

Figure 6.3: (a) The blocking fidelity of EIT for $V = 0$ as a function of Ω_c where we can see for $\Omega_c > 2\Omega_p^{\max}$ the fidelity becomes independent of Ω_c, and (b) the transfer fidelity as a function of the interaction V for $r = \Omega_c/\Omega_p^{\max} = 0.5, 2$ and 6.

$|1\rangle_t \rightarrow |0\rangle_t$ as a function of V in Fig. 6.3(b) for $r = \Omega_c/\Omega_p^{\max} = 0.5$, 2 and 6. This shows that for $V > 20\hbar\Omega_c^2/(4\Delta)$ a fidelity $\mathcal{F} > 0.98$ can be achieved by careful choice of Rydberg state so that the blockade effect will break the resonant EIT condition on the target atom. We use these results to determine the requirements on Ω_c and V to obtain a high-fidelity CNOT gate in Sec. 6.2.

Blocking Fidelity

We now estimate the fidelity of blocking the transfer on the target atom when the control atom is in qubit state $|1\rangle$. Fig. 6.4(a) shows the evolution of the populations of the states $|1\rangle$, $|0\rangle$ and $|r\rangle$ for $V = 0$ where it can be seen that the Raman pulse (illustrated by the grey line) has no effect as this his the case where EIT condition is satisfied. Fig. 6.4(b) shows the case where $V = 40\hbar\Omega_c^2/(4\Delta)$ which shifts the resonance of the state $|r\rangle$ so that the EIT condition is broken and Raman transfer occurs, demonstrated by an exchange of the populations $\rho_{|1\rangle}$ (blue) and $\rho_{|0\rangle}$ (red) while the populations $\rho_{|P\rangle}$ and $\rho_{|r\rangle}$ remain unchanged.

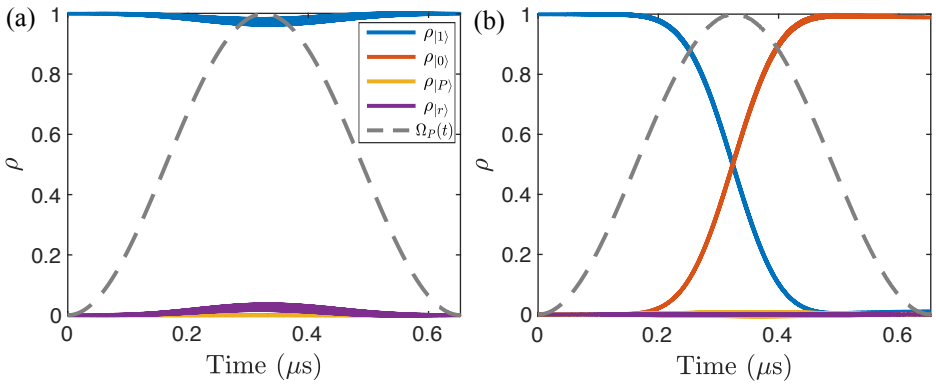

Figure 6.4: Time evolution of the smooth pulse in the 4-level system for (a) $V = 0$ and (b) $V = 40\hbar\Omega_c^2/(4\Delta)$ showing high fidelity blocking and state transfer respectively while leaving the populations of $|P\rangle$ and $|r\rangle$ unchanged. Calculated for $\Delta/2\pi = 1.2$ GHz, $\Omega_p^{\max}/2\pi = 70$ MHz and $\Omega_c = 6\Omega_p$.

6.4 Bell State Preparation Fidelity

As discussed in Sec. 2.3, to verify the quantum nature of the CNOT gate we first need to prepare one of the maximally entangled Bell states $|\Phi^{\pm}\rangle$ or $|\Psi^{\pm}\rangle$, defined in Eqs. 2.12. To do this the control qubit is placed in a superposition $(|0\rangle \pm |1\rangle)/\sqrt{2}$ whilst the target qubit is left in a pure state $|0\rangle$ or $|1\rangle$; the choice of target qubit state determines which Bell state is prepared. Assuming the target qubit is prepared in $|0\rangle$, the two-qubit input state is the mixed state $(|00\rangle \pm |10\rangle)/\sqrt{2}$. The CNOT gate is then applied to the mixed state which prepares one of the Bell states $|\Phi^{\pm}\rangle$. If the target qubit is initially prepared in $|1\rangle$ then the Bell states are $|\Psi^{\pm}\rangle$.

Experimentally we will prepare the Bell state $|\Phi^{+}\rangle$ and we want to estimate the Bell state preparation fidelity that we can achieve with the experimental settings. We can use the Hamiltonian given in Eq. 6.1 to estimate the Bell state preparation fidelity however, we perform Raman and Rydberg excitations using the D_2 line of caesium which has four levels in the intermediate state hyperfine manifold that are not accounted for in Eq. 6.1.

To do this we define the qubit states $|0\rangle = |F = 3, m_F = 0\rangle$, $|1\rangle = |F = 4, m_F = 0\rangle$

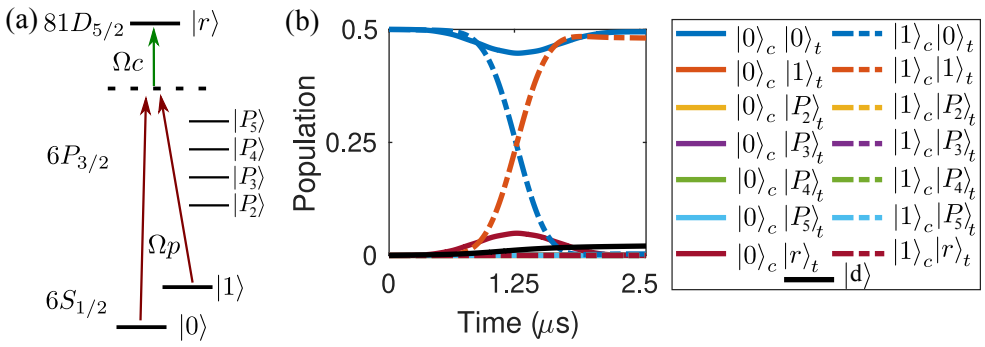

Figure 6.5: (a) Energy level scheme showing the hyperfine structure of the $6P_{3/2}$ intermediate level where $|P_i\rangle$ represent the levels $|F' = i\rangle$ for $i = \{2, 3, 4, 5\}$. (b) Bell state preparation fidelity showing the coupling to all the intermediate levels of the $|6P_{3/2}\rangle$ hyperfine manifold.

and $|r\rangle = |81D_{5/2}, m_j = 5/2\rangle$ which are coupled by Ω_p and Ω_c via the intermediate state using σ^+ circularly polarised light in each case. The accessible hyperfine levels of the intermediate state for σ^+ polarisation are $|P_i\rangle = |F' = i, m_{F'} = +1\rangle$ for $i = \{2, 3, 4, 5\}$. It is important to include these levels as they are only separated by ∼150 - 250 MHz, such that there may be some coupling between them and the excitation pulses Ω_p and Ω_c that can cause spontaneous emission of the qubits from the computational basis. Including the transitions to the intermediate states in the Hamiltonian gives Eq. 6.8 where $\Delta_{F'=i} = \Delta - \delta_{\text{hfs}}$, $\Omega_{p,j}^{F'=i} = \mathcal{E}_p \cdot \mathbf{d}_{j\to F'}/\hbar$ for $j = \{0, 1\}$, and $\Omega_c^{F'=i} = \mathcal{E}_c \cdot \mathbf{d}_{r\to F'}/\hbar$ where $\mathbf{d}$ is the dipole matrix element with $C_6 = -1627.8$ GHz.μm^6 calculated using ARC [101].

We use the Lindblad master equation to solve the Hamiltonian given by Eq. 6.8 to estimate the Bell state preparation fidelity for experiment parameters; $|r\rangle = |81D_{5/2}, m_j - 5/2\rangle$, $\Delta/2\pi = 1.03$ GHz, with a probe beam power of 80 nW with a beam waist $\omega_0 = 3$ μm, a coupling beam power 140 mW with a waist $\omega_0 = 12$ μm and for an atom separation of 5 μm. The finite lifetime of the Rydberg state is included as a decay to the $|P_i\rangle$ levels for the control atom and as a decay to a dark state for the target atom. In the simulation the values associated with spontaneous emission and decay are assumed to fall into a dark state that is outside the computational basis and we assume that the control qubit is prepared

perfectly in the superposition $(|0\rangle + |1\rangle)/\sqrt{2}$, with perfect coupling to the Rydberg state and no coupling to the intermediate hyperfine levels. The results are shown in Fig. 6.5(b) with a predicted Bell state preparation fidelity $\mathcal{F} = 0.973$ when effects of decay are included. This fidelity is limited by the experimentally attainable Rydberg laser power which limits Ω_c, however for a larger Rydberg power and increased intermediate state detuning $\mathcal{F} > 0.99$ is achievable.

$$
\mathcal{H} = \frac{\hbar}{2}
\begin{pmatrix}
0 & 0 & \Omega_{p,0}^{F'=2}(t) & \Omega_{p,0}^{F'=3}(t) & \Omega_{p,0}^{F'=4}(t) & \Omega_{p,0}^{F'=5}(t) & 0 & 0 & 0 & 0 & 0 & 0 & 0 & 0 \\
0 & -2\delta & \Omega_{p,1}^{F'=2}(t) & \Omega_{p,1}^{F'=3}(t) & \Omega_{p,1}^{F'=4}(t) & \Omega_{p,1}^{F'=5}(t) & 0 & 0 & 0 & 0 & 0 & 0 & 0 & 0 \\
\Omega_{p,0}^{F'=2}(t) & \Omega_{p,1}^{F'=2}(t) & -2\Delta_{F'=2} & 0 & 0 & 0 & \Omega_c^{F'=2} & 0 & 0 & 0 & 0 & 0 & 0 & 0 \\
\Omega_{p,0}^{F'=3}(t) & \Omega_{p,1}^{F'=3}(t) & 0 & -2\Delta_{F'=3} & 0 & 0 & \Omega_c^{F'=3} & 0 & 0 & 0 & 0 & 0 & 0 & 0 \\
\Omega_{p,0}^{F'=4}(t) & \Omega_{p,1}^{F'=4}(t) & 0 & 0 & -2\Delta_{F'=4} & 0 & \Omega_c^{F'=4} & 0 & 0 & 0 & 0 & 0 & 0 & 0 \\
\Omega_{p,0}^{F'=5}(t) & \Omega_{p,1}^{F'=5}(t) & 0 & 0 & 0 & -2\Delta_{F'=5} & \Omega_c^{F'=5} & 0 & 0 & 0 & 0 & 0 & 0 & 0 \\
0 & 0 & \Omega_c^{F'=2} & \Omega_c^{F'=3} & \Omega_c^{F'=4} & \Omega_c^{F'=5} & -2\Delta_c & 0 & 0 & 0 & 0 & 0 & 0 & 0 \\
0 & 0 & 0 & 0 & 0 & 0 & 0 & 0 & \Omega_{p,0}^{F'=2}(t) & \Omega_{p,0}^{F'=3}(t) & \Omega_{p,0}^{F'=4}(t) & \Omega_{p,0}^{F'=5}(t) & 0 & 0 \\
0 & 0 & 0 & 0 & 0 & 0 & 0 & 0 & \Omega_{p,1}^{F'=2}(t) & \Omega_{p,1}^{F'=3}(t) & \Omega_{p,1}^{F'=4}(t) & \Omega_{p,1}^{F'=5}(t) & 0 & 0 \\
0 & 0 & 0 & 0 & 0 & 0 & 0 & -2\delta & -2\Delta_{F'=2} & 0 & 0 & 0 & \Omega_c^{F'=2} & 0 \\
0 & 0 & 0 & 0 & 0 & 0 & 0 & \Omega_{p,0}^{F'=2}(t)\ \Omega_{p,1}^{F'=2}(t) & 0 & -2\Delta_{F'=3} & 0 & 0 & \Omega_c^{F'=3} & 0 \\
0 & 0 & 0 & 0 & 0 & 0 & 0 & \Omega_{p,0}^{F'=3}(t)\ \Omega_{p,1}^{F'=3}(t) & 0 & 0 & -2\Delta_{F'=4} & 0 & \Omega_c^{F'=4} & 0 \\
0 & 0 & 0 & 0 & 0 & 0 & 0 & \Omega_{p,0}^{F'=4}(t)\ \Omega_{p,1}^{F'=4}(t) & 0 & 0 & 0 & 0 - 2\Delta_{F'=5} & \Omega_c^{F'=5} & 0 \\
0 & 0 & 0 & 0 & 0 & 0 & 0 & \Omega_{p,0}^{F'=5}(t)\ \Omega_{p,1}^{F'=5}(t) & 0 & \Omega_c^{F'=3} & \Omega_c^{F'=4} & \Omega_c^{F'=5} & -2(\Delta_c + V) & 0
\end{pmatrix}
\tag{6.8}
$$

Part III

Experiment

Chapter 7

Experiment Set-up

The long term goal of this project is to demonstrate a hybrid quantum system between cold atoms and a superconducting microwave resonator. The hybrid system requires cryogenic temperatures which presents a problem as at cryogenic temperatures the caesium atoms stick to the walls of the vacuum chamber, meaning the standard technique of cooling atoms directly from background vapour pressure is not possible. To overcome this challenge we use a dual chamber design where caesium atoms are loaded from background vapour in a non-cryogenic room temperature environment into a magneto-optical trap (MOT), and are then transported ~ 30 cm to a second vacuum chamber, which we call the science chamber, using a mechanical translation stage. A schematic of this design is shown in Fig. 7.1. Note that none of the experiments presented in this thesis are performed at cryogenic temperatures.

The MOT chamber is kept under vacuum with a background pressure of 9.3×10^{-9} mbar using a 3 L/s ion pump that houses two SAES caesium alkali metal dispensers to provide a source of atoms for the experiment. The MOT and science chambers are separated by a narrow differential pumping tube which provides independent pressures in both chambers enabling the science chamber to be kept at an ultra-high vacuum (UHV) pressure of 1.7×10^{-10} mbar using a 70 L/s Gamma Vacuum ion pump. A pair of high numerical aperture (NA) lenses (Geltech

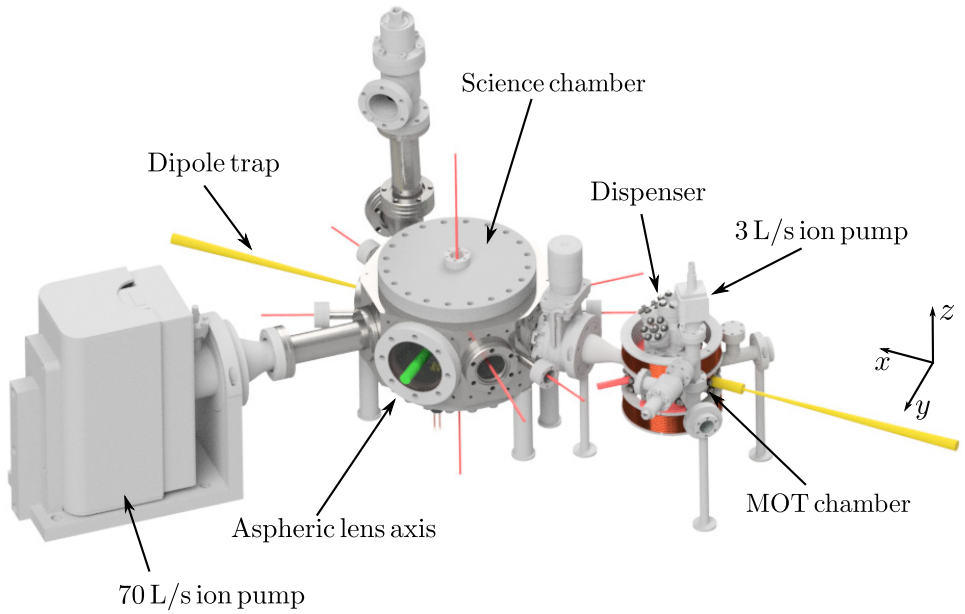

Figure 7.1: Experiment CAD drawing showing the two vacuum chambers with the MOT chamber on the right of the image connected to the science chamber via a differential pumping tube. The MOT chamber is connected to a 3 L/s ion pump with caesium alkali dispensers and the science chamber connected to a 70 L/s ion pump to maintain vacuum. The yellow line illustrates the path of the dipole trapping laser and red lines depict points where light can enter the vacuum chambers.

355561) with NA = 0.45 at 852 nm with a working distance of ∼7 mm, are located inside the science chamber to achieve diffraction limited foci for trapping and site addressability, while three pairs of rectangular shim coils (Helmholtz configuration) control the magnetic field environment. An additional pair of circular bias coils are placed around the science chamber viewport to provide a large bias magnetic field to discriminate the hyperfine magnetic sublevels and define a quantisation axis. For a detailed description of the vacuum chamber design and construction, the reader is referred to Refs. [110, 111].

In this section, we will focus on modifications made to the experiment that have been added to improve the fidelity of quantum gate operations. We will briefly

discuss well-known laser cooling and trapping techniques and their implementation to realise a MOT and optical dipole trap experimentally, and describe the process of single atom trapping and imaging in the experiment.

7.1 Laser Cooling

Laser cooling is an essential tool for the cooling and trapping of atoms in many research laboratories around the world [112–116]. The first step to cool and trap atoms is using a magneto-optical trap (MOT) [117] which consists of a pair of anti-Helmholtz magnetic field coils combined with three orthogonal pairs of counter-propagating laser beams with circular polarisation. The coils create a magnetic quadrupole field with a magnetic field zero at the origin and a uniform linear gradient that perturbs the atomic energy levels (Zeeman effect). The laser beams intersect at the centre of the coils and are red-detuned from the atomic transition, ω_0, such that as the atoms move away from the zero point, the Zeeman shift of the magnetic field brings the atoms closer to the resonance of the beam going in the opposite direction. Thus the atoms are trapped by a position dependent restoring force which returns the atoms to the centre of the beam.

Trapping atoms in a MOT in this way leads to cooling via the Doppler effect. It works on the principal that a moving atom red-detuned from resonance experiences a shift which brings it closer to the laser's resonance frequency, propagating in the opposite direction to the atom's motion, leading to a frictional force which slows the atom down. The MOT cools the atoms to the Doppler limited temperature,

$$T_D = \frac{\hbar\gamma}{2k_B}, \tag{7.1}$$

where γ is the natural linewidth of the cooling transition and k_B is the Boltzman constant. The Doppler temperature for caesium on the D_2 line is $T_D = 125\ \mu$K [89]. Cooling below the Doppler temperature can be achieved using sub-Doppler cooling techniques in atoms with Zeeman substructure which cool the atoms to a few times the recoil-temperature [75, 112, 118].

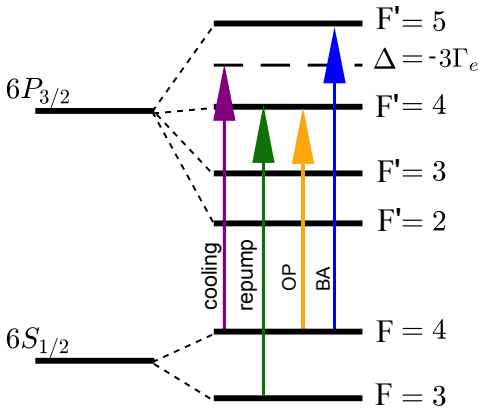

Figure 7.2: Energy levels addressed for cooling and trapping on the D_2 line of caesium. The cooling light (purple) is red-detuned from the $|F = 4\rangle \rightarrow |F' = 5\rangle$ transition by $\Delta = -3\Gamma_e$, the repump light (green) is resonant with $|F = 3\rangle \rightarrow |F' = 4\rangle$, optical pumping (yellow) is resonant with $|F = 4\rangle \rightarrow |F' = 4\rangle$ and the blow away (blue) is resonant with $|F = 4\rangle \rightarrow |F' = 5\rangle$.

7.1.1 Cooling Lasers

To laser cool the atoms experimentally we use two home-built external cavity diode lasers (ECDL) [119] each with an 852 nm diode (Thorlabs L850P150) providing up to 150 mW of power. The main cooling laser is used for cooling, optical pumping on the D_2 line and resonant blow away, and the second laser is the repump laser used to pump atoms out of the $F = 3$ state. The transitions used within the caesium atom for cooling and trapping on the D_2 line of caesium are illustrated in Fig. 7.2. The cooling laser is locked to the $\left|6S_{1/2}, F = 4\right\rangle \rightarrow \left|6P_{3/2}, F' = 5\right\rangle$ transition via polarisation spectroscopy [120] and red-detuned by 400 MHz through a double-pass acousto-optical modulator (AOM) operating at 200 MHz. The cooling light then passes through a tapered amplifier (TA) to increase the available power for trapping and cooling, followed by another double-pass AOM operating at 200 MHz which is used to control the amplitude and detuning of the cooling light. The light is then coupled into a polarisation maintaining (PM) fiber and sent to the experiment.

Before the TA, there are two pick-off's using polarising beam splitters (PBS) to

obtain separate paths for the D_2 optical pumping and blow away light which are described in Sec 8.1. These paths have double pass AOM's to control the detuning of the light giving frequency control for the desired transitions and are recombined on a 50:50 beamsplitter before being coupled into the same PM fiber. It should be noted here that an upgrade to the experiment enabled optical pumping on the D_1 line as is discussed in Sec. 8.2.

The repump laser is used to repump any atoms that have been depumped into the $\left|6S_{1/2}, F = 3\right\rangle$ dark state back to the cooling transition. The repump laser is locked using polarisation spectroscopy to the cross-over transition between $\left|6S_{1/2}, F = 3\right\rangle \rightarrow \left|6P_{3/2}, F' = 2\right\rangle$ and $\left|6S_{1/2}, F = 3\right\rangle \rightarrow \left|6P_{3/2}, F' = 4\right\rangle$ which provides a better signal-to-noise ratio than locking to the $\left|6S_{1/2}, F = 3\right\rangle \rightarrow \left|6P_{3/2}, F' = 4\right\rangle$ transition. A double pass AOM operating at 88 MHz is in place to shift the frequency of the light back to the $\left|6S_{1/2}, F = 3\right\rangle \rightarrow \left|6P_{3/2}, F' = 4\right\rangle$ transition and is coupled into the same PM fiber as the main cooling light following combination on a 50:50 beam splitter.

The AOMs not only provide frequency control but also enable fast switching of laser pulses and are accompanied by mechanical shutters [121] in each laser path to prevent leakage light reaching the experiment. We have the ability to characterise the MOT using a CCD camera (DMK 335G445), where we measure $\sim 10^6$ atoms which is sufficient for loading an optical dipole trap - the main tool used in our experiments. After the atoms are loaded into the MOT, they are cooled to sub-Doppler temperatures using polarisation gradient cooling (PGC) [112]. To achieve this the cooling detuning is ramped to $\Delta = -15\Gamma_e$ for a period of 10 ms to decrease the temperature of the atoms from $T = 300$ μK to 10 μK.

7.2 Optical Dipole Trap

In the experiment described in this thesis, the atoms in the MOT must be transported over a distance of 30 cm to the science chamber. This is achieved using an

optical dipole trap (ODT) and a mechanical translation stage. Here we give a brief overview of optical dipole trapping and it's implementation in the experiment. A more detailed description of the optical dipole trap can be found in previous group theses [110, 111].

Optical dipole traps are produced by tightly focusing a (typically) red-detuned dipole beam at the centre of the MOT. By using a red-detuned beam the atom is drawn and trapped in a region of high intensity. The dipole light exerts a dipole force on the atoms creating a conservative potential [122],

$$U_{\text{dip}}(\boldsymbol{r}) = \frac{3\pi c^2}{2\omega_0^3}\frac{\Gamma}{\Delta}I(\boldsymbol{r}), \tag{7.2}$$

where $\Delta = \omega_0 - \omega$ is the detuning from the atomic resonance, ω_0 is the angular frequency of the atomic resonance, Γ is the decay rate from the excited state, $I(\boldsymbol{r})$ is the position dependent field intensity. The scattering rate from the trapping field is,

$$\Gamma_{\text{sc}}(\boldsymbol{r}) = \frac{3\pi c^2}{2\hbar\omega_0^3}\left(\frac{\Gamma}{\Delta}\right)^2 I(\boldsymbol{r}). \tag{7.3}$$

From these equations we can see that the dipole potential and scattering rate depend strongly on the laser's detuning and intensity therefore optical dipole traps are formed using large detuned and high-intensity beams to minimise scattering.

In practice atoms are multi-level; taking this into account the expression for the dipole potential for atoms in the ground state at the maximum intensity is,

$$U_0 = \frac{3\pi c^2}{2}\left(\frac{1}{3}\frac{\Gamma_{D_1}}{\omega_{D_1}^3\Delta_{D_1}} + \frac{2}{3}\frac{\Gamma_{D_2}}{\omega_{D_2}^3\Delta_{D_2}}\right), \tag{7.4}$$

where Δ_{D_1,D_2} are the effective detunings from the D_1 and D_2 lines of caesium respectively [122].

The dipole beam focused on an atom causes a spatially varying potential that is described by the intensity distribution of a Gaussian beam, i.e.,

$$I(r,z) = \frac{I_0}{1 + z^2/z_R^2}\exp\left(-2\frac{r^2}{w^2(z)}\right), \tag{7.5}$$

where $I_0 = 2P/(\pi w_0^2)$, $z_R = \pi w_0^2/\lambda$ is the Rayleigh length and w_0 is the $1/e^2$ intensity radius of the beam waist. The beam waist evolves along the axial direction

as $w(z) = w_0(1 + (z/z_R)^2)^{1/2}$, which gives the trapping potential for the Gaussian trapping beam,

$$U(r, z) = \frac{U_0}{1 + z^2/z_R^2} \exp\left(-2\frac{r^2}{w^2(z)}\right). \tag{7.6}$$

The trapping potential can be approximated as a harmonic oscillator with the oscillation frequencies of the trapped atoms given by

$$\omega_r = \sqrt{\frac{4U_0}{mw_0^2}} \quad \text{and} \quad \omega_z = \sqrt{\frac{2U_0}{mz_r^2}}, \tag{7.7}$$

for the radial and axial directions respectively. The Rayleigh length is larger than the beam waist such that $\omega_r \gg \omega_z$.

7.2.1 Experimental Implementation

We achieve optical dipole trapping using a 1064 nm Nd:YAG laser, providing 10 W of light and use an 80 MHz AOM for fast switching. The ODT is focused to a waist of 43 μm and overlapped with the MOT in the MOT chamber for 50 ms, loading 10^5 atoms into the ODT. The atoms in the ODT are then cooled to 10 μK by polarisation gradient cooling by applying the cooling beams for 20 ms, and are then transported 30 cm using a mechanical translation stage into the science chamber in 800 ms.

The ODT was characterised in previous group theses [110, 111] and the results are stated here for completeness: the atoms in the ODT have a lifetime of 4.9 s and the ODT has an axial trap frequency $\omega_z/2\pi = 8$ Hz and, a radial trap frequency $\omega_r/2\pi = 1.1$ kHz.

7.3 Single Atom Trapping and Imaging

In this experiment we require single atoms which we achieve by loading a microscopic tweezer trap from the ODT. This is implemented following the technique developed by Schlosser *et al.* [123] which uses light assisted collisions to expel pair of atoms from the microscopic tweezer trap.

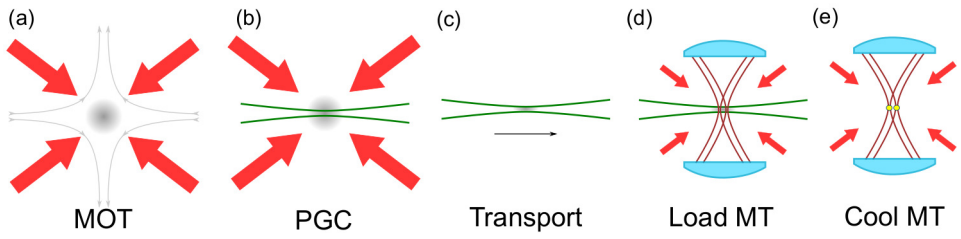

Figure 7.3: Atom loading sequence showing; (a) the MOT loading stage, the red arrows indicate the cooling and repump light, (b) polarisation gradient cooling (PGC) of the MOT and the overlap with the optical dipole trap (ODT) in green, (c) optical transport where the ODT is moved from the MOT chamber to the science chamber, (d) the ODT is overlapped with a pair of microscopic tweezer traps and (e) the atoms are cooled and pair of atoms are expelled from the microtraps by light assisted collisions (LAC) to achieve a single atom in each microtrap.

7.3.1 Single Atom Trapping

Following optical transport which brings the atoms into the science chamber, the ODT is overlapped with a pair of microscopic tweezer traps (microtraps) for a duration of 60 ms. The microtraps are formed using a Coherent 1064 nm Mephisto laser with two trapping sites created using PBS's to split and recombine the light with a waist of 1.85 μm. During the overlap stage, three pairs of cooling beams are applied with intensity $I = I_{\text{sat}}$ per beam and at a detuning $\Delta = -6\Gamma_e$, which enables loading of multiple atoms into each tweezer trap, as illustrated in Fig. 7.3(d-e).

The cooling light is modulated out-of-phase with the microtrap light at 1 MHz to minimise the differential AC Stark shift induced by the trapping light. Single atom loading is achieved using light assisted collisions (LACs) [123] with the cooling light detuned by $\Delta = -8\Gamma_e$ with intensity $I = 0.5I_{\text{sat}}$ per beam. The light assisted collisions cause pairs of atoms to be removed from the trap leaving only one or no atom present in each microtrap at the end of this stage with 50 % probability.

7.3.2 Single Atom Imaging

The single atoms in the microtraps are imaged using fluorescence collected from the atoms on a sCMOS camera (Andor Zyla 5.5 USB). The details of this can be found in Ref. [124] and will be summarised here.

To distinguish the presence of an atom from background light, the scattering rate from the trapped atom needs to be maximised. The scattering rate for a single atom is given by [75],

$$\Gamma_{\text{sc}} = \frac{\Gamma_e}{2} \frac{I/I_{\text{sat}}}{1 + I/I_{\text{sat}} + 4(\Delta/\Gamma_e)}, \tag{7.8}$$

where Δ is the detuning and I the intensity of the laser. This relation suggests that the greatest scattering rate is achieved on resonance however working in this regime causes heating, so that the atom will eventually be lost from the trap. To prevent this from happening, imaging is performed with $I = 0.5I_{\text{sat}}$ of cooling power at a detuning of $\Delta = -3\Gamma_e$ with the cooling light modulated out-of-phase with the microtrap light. This results in an effective photon scattering rate of $\Gamma_{\text{sc}} = 450$ photons/ms, with an expected flux of 15 photons/ms incident on the camera [124]. The scattered light is collected in a 3×3 pixel region of interest, centred on the atom, resulting in a binomial distribution of photon counts which detect the presence or absence of an atom. An example of this is shown in Fig. 7.4(a) and (b) which plots the histograms of each microtrap corresponding to background (BG) and single atom loading, showing that they are clearly distinguishable from each other.

In our experiments we take two images: the first image is taken after the LAC stage to verify if a single atom has been loaded into the microtrap and the second image is taken at a later stage after various pulse sequences have been applied, e.g. a Raman rotation. Fig. 7.4(c) shows a correlation between counts in the first image and the second image taken 50 ms later. We can clearly see two distinct clusters for each microtrap (trap 1 = blue, trap 2 = red); the top right quadrant counts atoms present in both images and the bottom left quadrant shows no atom

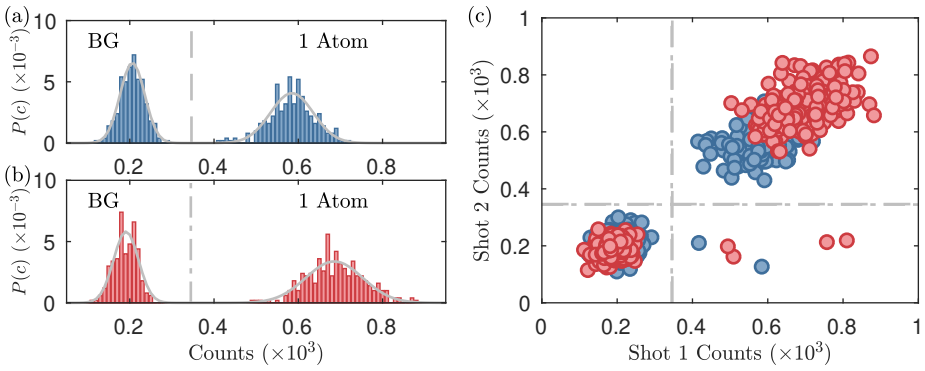

Figure 7.4: Probability distribution of counts from 250 measurements of (a) trap 1 and (b) trap 2, that distinguish background from a trapped atom within a set region of interest. (c) Correlation plot showing counts from a first image plotted against a second image taken some time later.

was detected in either image. The few points in the bottom right quadrant are atoms loaded in image one but lost from the microtrap by image two. Recording data in this way enables us to measure the probability to retain an atom after imaging, achieving a >98 % retention probability for both traps.

The characterisation of the microtraps is detailed in previous group theses [110, 111] and is summarised here. The lifetime of the microtrap is 8.7 s at a trap depth of $U_0 = 1$ mK and is mainly limited by background collisions [124]. The radial trapping frequencies are $\omega_r/2\pi = 23.7$ and 23.2 kHz which give waists of 1.88 μm and 1.81 μm for the microtraps. The temperature of the atoms in the microtraps is $T = 16$ μK which is measured using the release-recapture method [125, 126].

7.4 Summary

In this chapter we have given an overview of the core cold atom experiment that is used throughout this thesis. Laser cooling and trapping techniques are used to create a MOT loaded from background vapour caesium atoms, which are loaded into an optical dipole trap and transported 30 cm to a science chamber. The atoms are then loaded into a pair of microscopic tweezer traps and light assisted

collisions are used to ensure only one atom is loaded into each microtrap, with 50 % probability. The atoms are imaged by non-destructive fluorescence imaging on a sCMOS camera with a retention efficiency of > 98 %.

Chapter 8

Qubit State Preparation and Readout

To prepare the atoms in a state useful for performing quantum gates, we use the technique of optical pumping [86, 127]. This involves applying a magnetic field using coils placed around the experiment chamber to define a quantisation axis and to separate the hyperfine levels of the atom. Optical pumping light can then be applied along the quantisation axis to pump the atoms into a desired hyperfine level, in our case this is the state $|1\rangle = |F = 4, m_F = 0\rangle$.

For the results presented in this thesis, a new optical pumping laser was installed to enable optical pumping on the D_1 line of caesium, to improve the optical pumping efficiency compared to using the D_2 line. In this chapter we discuss our ability to prepare and measure the atoms in the desired qubit state, the detection methods used to distinguish between the qubit states $|1\rangle$ and $|0\rangle = |F = 3, m_F = 0\rangle$ and describe the optical pumping technique used experimentally, including a comparison of the optical pumping efficiency between the D_1 and D_2 lines of caesium.

8.1 Hyperfine State Discrimination

Our ability to determine which qubit state the atoms are in is crucial to performing rotations between the ground states $|1\rangle \rightarrow |0\rangle$. To do this we use a blow away beam which is sourced from the cooling laser (see Sec. 7.1) and use AOMs to shift the blow away light such that it is resonant with the $\left|6S_{1/2}, F = 4\right\rangle \rightarrow \left|6P_{3/2}, F' = 5\right\rangle$ transition. The blow away beam heats atoms in the $F = 4$ manifold out of the trap, which leaves only atoms in the $F = 3$ manifold.

The blow away light enters the vacuum chamber via the same path as the optical light as illustrated in Fig. 8.1 with a beam waist of 500 μm and a power of 20 μW corresponding to $\sim 2I_{\text{sat}}$. The microtrap light is chopped on and off at 1 MHz to minimise light shifts while the blow away light is applied. Using this blow away technique we can remove atoms from the microtrap in the $F = 4$ manifold with an efficiency $> 99\%$ [110].

The atoms are imaged in the $F = 4$ hyperfine level, meaning that to image atoms in the $F = 3$ hyperfine level we need to apply repump light (see Sec. 7.1.1). The repump light pumps the atoms into the $F = 4$ manifold, then fluorescence imaging (described in Sec. 7.3.2) is used to detect the presence of an atom. Using the blow away beam prior to imaging allows us to distinguish between atoms in the $F = 4$ and $F = 3$ hyperfine levels, and realise state sensitive readout.

8.2 Optical Pumping

To perform coherent operations it is essential to initialise the atoms in a given quantum state. This involves initialising the atoms in a specific Zeeman sub-level within the hyperfine manifold which we achieve by optical pumping.

There are two main ways in which atoms can be optically pumped; stretched state and clock state optical pumping. Clock state optical pumping - so called because this transition is used in optical clocks to define the second [83] - places

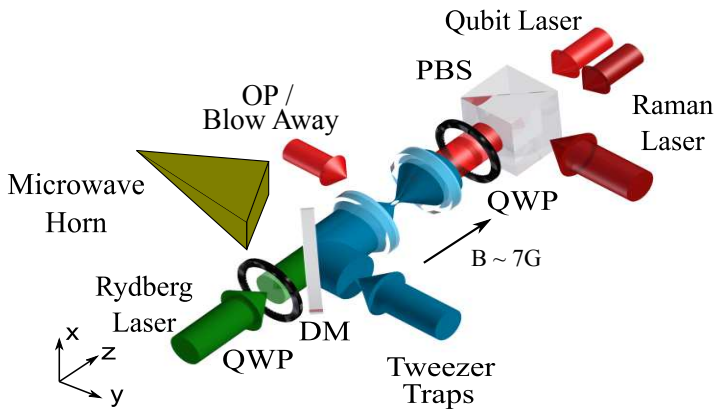

Figure 8.1: A schematic of the experiment set-up describing the blow away and optical pumping pathways along the y-axis. A 7 G bias field is applied along the z-axis to separate the hyperfine levels for qubit state preparation and the pathways for the Raman laser and microwave antenna are shown.

the atoms in the state $|F = 4, m_F = 0\rangle$ using π-polarised light. The dipole transition between $|F = 4, m_F = 0\rangle \rightarrow |F' = 4, m_F = 0\rangle$ is forbidden due to angular momentum selection rules, however spontaneous emission occurs randomly so that $\Delta m_F = \{-1, 0, +1\}$, allowing the atoms to accumulate in the dark state $|F = 4, m_F = 0\rangle$ as illustrated in Fig. 8.2(a). The clock state is magnetically insensitive which is advantageous as random fluctuations in the applied magnetic field do not couple into the experiment. We utilise clock state optical pumping in all the results presented in this thesis.

Stretched state optical pumping places the atoms in one of the extreme hyperfine levels, which for caesium are $|F = 4, m_F = \pm 4\rangle$, using $\sigma^{\pm}$-polarised light. The case of σ^{+}-polarised light is shown in Fig. 8.2(b) where all the atoms are optically pumped into the dark state $|F = 4, m_F = 4\rangle$.

Previously we have used the D_2 line for optical pumping [47] but an experimental upgrade now means we can apply optical pumping using the D_1 line of caesium. The advantage of using the D_1 line for optical pumping is that there are only two hyperfine levels associated with the $|6P_{1/2}\rangle$ level as shown in Fig. 8.3(a) and these are separated by ~ 1.1 GHz [89] which makes unwanted coupling between

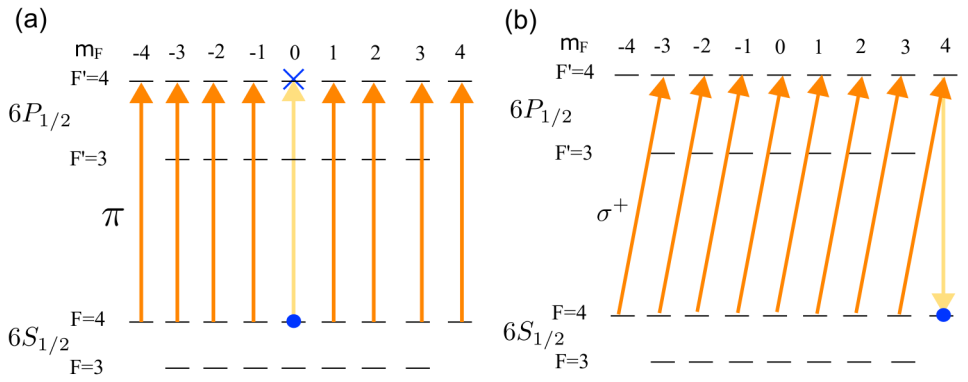

Figure 8.2: The possible optical pumping schemes are (a) clock state optical pumping using linearly polarised light and (b) stretched state optical pumping using circularly (σ^+ in this case) polarised light, shown here for the D_1 line. In each case the atoms accumulate in a dark state which is not coupled to the light fields due to angular momentum selection rules.

the hyperfine levels less likely to occur. On the other hand, the $|6P_{3/2}\rangle$ level of the D_2 line shown in Fig. 8.3(b), has four hyperfine levels separated by $\sim 150 - 250$ MHz [89] which makes off-resonant coupling more likely. This can reduce the effectiveness of the optical pumping beam so that the atoms are not be well-prepared in the desired hyperfine state and, ultimately, decrease the fidelity of the qubit rotations. To compare the effectiveness of each optical pumping laser we make a comparison of the two.

The source of the 852 nm light used to drive D_2 optical pumping comes from a pick-off on the cooling laser beam path. A double-pass AOM is used to shift the frequency of the light by 80 MHz to be resonant with the transition $|6S_{1/2}, F = 4\rangle \rightarrow |6P_{3/2}, F' = 4\rangle$ and is coupled into a polarisation maintaining fiber to be sent to the experiment. The 895 nm light for driving optical pumping on the D_1 line is provided by a home-built ECDL with a 895 nm diode (EYP-RWE-0920-04010-1500-SOT02-0000) and locked on the transition $|6S_{1/2}, F = 4\rangle \rightarrow |6P_{1/2}, F' = 4\rangle$ using polarisation spectroscopy [128]. This light passes through two double pass AOMs operating at 250 MHz to enable fast pulse switching and for possible future locking to the $|6P_{1/2}, F' = 3\rangle$ level. The D_1 light is also sent to the experiment

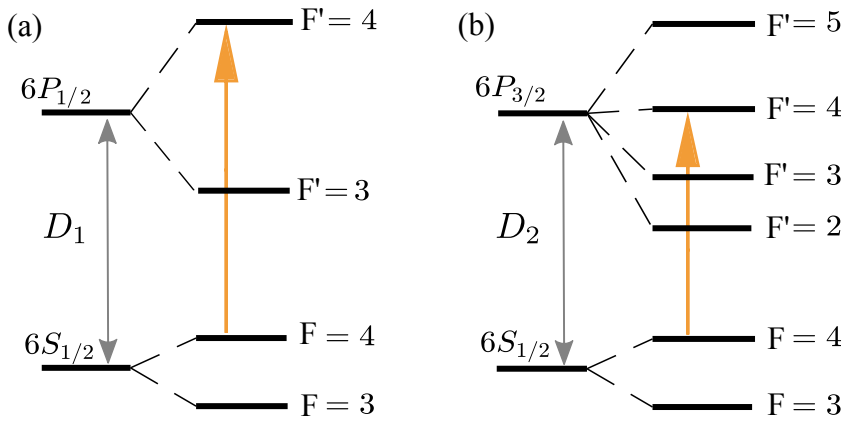

Figure 8.3: The optical pumping schemes for (a) D_1 line and (b) D_2 line, showing the hyperfine structure in each case.

using a polarisation maintaining fiber.

The light for both D_1 and D_2 optical pumping beams address the experiment along the same axis as shown in Fig. 8.1, by combining their light using a 50:50 fiber splitter. This gives both optical pumping beams the same fiber output therefore the same beam path to address the atoms. The optical pumping light passes through a Glann-Taylor polariser to achieve linearly (π) polarised light with high purity before entering the vacuum chambers. A 7.5 G bias field is applied along the y-axis of the experiment chamber to drive π-transitions with the optical pumping beams. During the optical pumping stage, repump light sourced from the molasses beams (see Sec. 7.1.1), is applied to repump atoms that fall into $F = 3$ back into the $F = 4$ manifold.

8.2.1 Optimisation of Optical Pumping

The fidelity of optical pumping can be measured using a depump method [129]. As illustrated in Fig. 8.4(a), this involves applying an optical pumping pulse with repump light to pump the atoms into the desired state, $|1\rangle = |F = 4, m_F = 0\rangle$. After this the optical pumping light is applied without repump for a variable duration so that the atoms will accumulate in the $F = 3$ manifold as the length of the pulse increases. Using the blow away pulse, the $F = 3$ and $F = 4$ levels can

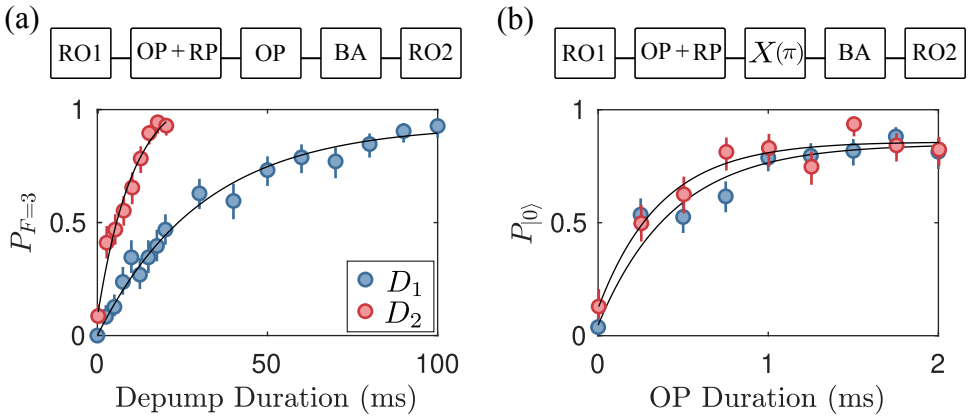

Figure 8.4: A comparison of the effectiveness of using the D_1 and D_2 lines for optical pumping. (a) The optical pumping light is applied without repump light for a variable time to measure the rate of depump from the $|F = 4, m_F = 0\rangle$ state for the D_2 (red) and D_1 (blue) lines with depump rates $\tau_{\mathrm{DP}}^{D_2} = 10$ ms and $\tau_{\mathrm{DP}}^{D_1} = 30.9$ ms respectively. (b) The effectiveness of each optical pumping line is compared by applying a $X(\pi)$-rotation as the optical pumping pulse duration is scanned. This gives an optical pumping rate of $\tau_{\mathrm{OP}}^{D_2} = 390$ μs and $\tau_{\mathrm{OP}}^{D_1} = 440$ μs for the D_2 (red) and D_1 (blue) lines respectively.

be distinguished allowing us to measure the rate of depump of the atoms from the $|1\rangle$ state. A longer depump rate, means more efficient optical pumping. To enable a fair comparison of the D_1 and D_2 lines, the power in each optical pumping beam is 20 μW and as they address the atoms via the same optical path after the fiber, all other beam parameters should be the same.

Using this depump method we compare the effectiveness of the D_1 and D_2 lines, when used for optical pumping. The data are plotted in Fig. 8.4(a) and are fit to a function of the form $-A\exp(-t/\tau) + B$, where τ is the decay rate for depump. From the fits, the depump decay rates are $\tau_{\mathrm{DP}}^{D_2} = 10$ ms and $\tau_{\mathrm{DP}}^{D_1} = 30.8$ ms showing a three-fold increase in efficiency when using the D_1 line for optical pumping.

To measure the optical pumping rate we use the sequence shown in Fig. 8.4(b), which allows us to directly measure the effectiveness of the optical pumping beam as a function of its duration. The optical pumping beam (with repump) is applied for a variable duration, this is followed by an $X(\pi)$ rotation (see Sec. 10.3) and

a blow away pulse which allows us to measure the effectiveness of the optical pumping beam by observing how quickly the atoms are transferred from $|1\rangle \rightarrow |0\rangle = |F = 3, m_F = 0\rangle$. The data for this measurement are presented in Fig. 8.4(b) for the D_2 (red) and D_1 (blue) optical pumping beams. The data are fitting with the same function as the depump scans, to give optical pumping rates $\tau_{\mathrm{OP}}^{D_2} = 360\ \mu s$ and $\tau_{\mathrm{OP}}^{D_1} = 440\ \mu s$.

The fidelity of optical pumping is calculated using [129],

$$\mathcal{F}_{\mathrm{OP}} = 1 - \frac{1}{\tau_{\mathrm{DP}}/\tau_{\mathrm{OP}}}, \tag{8.1}$$

which assumes there is an optical pumping rate τ_{OP} pumping atoms into $|1\rangle$, and a depumping rate τ_{DP} removing atoms from $|1\rangle$. This essentially normalises the power of the optical pumping laser. Using this relation gives fidelities $\mathcal{F}_{\mathrm{OP}}^{D_2} = 0.966$ and $\mathcal{F}_{\mathrm{OP}}^{D_1} = 0.986$ for D_2 and D_1 optical pumping respectively.

From the calculation of this fidelity we can see that there has been an improvement in the optical pumping efficiency by using the D_1 line, however there is still room for more improvement. The main issue with optical pumping in our experiment is the ability to set the polarisation due to access restrictions on the optics table. The optical pumping beams have their polarisation set before entering the MOT chamber, the light then passes through several windows including a low optical quality CF16 Kodial glass viewport, in the MOT and science chambers before it can be measured again. This means that there may be some distortion to the polarisation of the optical pumping beam so that it has a weak $\sigma^{\pm}$ component that causes leakage from the optical pumping state.

8.3 Summary

The pair of trapped atoms are addressed by an optical pumping beam which prepares the atoms in the qubit state $|1\rangle = |F = 4, m_F = 0\rangle$ and a blow away beam is used to distinguish between atoms in the $F = 4$ and $F = 3$ manifolds to enable state sensitive readout of the ground state hyperfine levels. We have compared the

efficiency of applying optical pumping using the D_1 and D_2 lines of caesium and found some improvement in using the D_1 line. There are however some experimental challenges associated with setting the polarisation of the optical pumping beam which impacts the fidelity of preparing the atoms $|1\rangle$ and subsequently qubit rotations we want to apply.

Chapter 9

Excitation Lasers and Microwave Antenna

In this chapter we describe the laser systems that are used to experimentally realise two-photon Rydberg excitations and Raman transfer. The key features are the installation of a SolsTiS ECD-X (MSquared) laser system, and the implementation of an optical phase-lock loop to the Raman laser. In addition, we describe the installation of a microwave antenna to realise ground state rotations.

A schematic of the arrangement of the Rydberg, Qubit and Raman lasers, and microwave horn with respect to the atoms is shown in Fig. 9.1. This addressing arrangement of the lasers and microwaves is used consistently throughout this thesis.

9.1 Qubit and Rydberg Lasers

The work presented in this thesis uses a two-photon ladder excitation scheme to excite to the Rydberg state $|r\rangle = \left|81D_{5/2}, m_j = 5/2\right\rangle$. The two-photon process is achieved using an 852 nm laser to provide the lower photon for excitation and one of two Rydberg lasers for the upper photon. Excitations to the Rydberg

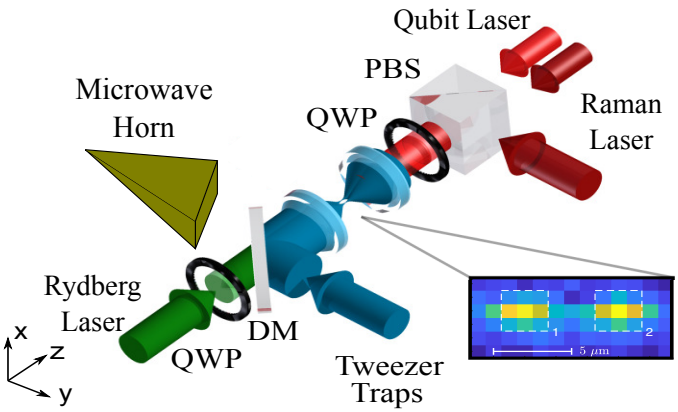

Figure 9.1: A schematic of the experiment set-up showing the position of the Rydberg (green), Qubit (red) and Raman lasers (brown) as the address the atoms. The position of the microwave horn is outside of the science chamber (not shown in the schematic) which is placed outside a viewport at 45° w.r.t. the z-axis.

state require narrow linewidth, well-stabilised lasers to minimise errors which we implement this using a high-finesse ultra-low expansion (ULE) cavity, achieving sub-kHz linewidth with a measured linear frequency drift of ∼1 Hz/s, details of which can be found in Refs. [111, 130]. The free spectral range of the ULE cavity is 1.5 GHz which puts a boundary on the detuning from the intermediate state and the possible Rydberg state [111, 130].

9.1.1 Qubit Laser

The Qubit laser is a home-built ECDL operating at 852 nm with an Eagleyard diode(EYP-RWE-0860-06010-1500-SOT02-0000), which has a maximum output power of 100 mW. The Qubit laser is locked to a cavity mode detuned from $\left|6P_{3/2}, F' = 5\right\rangle$ by +1.134 GHz using the Pound-Drever-Hall technique [131], with frequency and intensity control achieved using the -1 diffraction order of a double-pass AOM with a central frequency of 80 MHz to give a detuning at the atoms $\Delta_A/2\pi = +870$ MHz. A mechanical shutter is also used to prevent leakage light reaching the atoms. The light is coupled into a polarisation maintaining (PM) fiber and output to the experiment. Before entering the science chamber the polarisa-

tion is set to σ^+ circular polarisation and the beam is focused so that it addresses a single atom within the science chamber, with a $1/e^2$ beam waist of 3 μm.

The atom that the Qubit laser addresses in the science chamber is labelled the control atom as the atom is used as the control qubit in the demonstration of the CNOT gate in Chapter 11. The optimisation of the two-photon excitation to the Rydberg state on the control atom is presented in Sec. 10.4.

In addition to Rydberg excitation, the Qubit laser is used in an optical phase lock loop to stabilise the Raman laser (Sec. 9.2) and to enable single site sensitivity during a microwave rotation (Sec. 10.3).

9.1.2 Ryberg lasers

The two Rydberg lasers used to provide the upper photon for Rydberg excitation are a home-built ECDL with 1018 nm AR-coated laser diode (Sacher SAL-1030-060) and a SolsTiS ECD-X laser from MSquared. Both lasers are stabilised to the high-finesse ULE cavity with locking achieved using an electronic sideband technique described in [111, 130]. The relevant detail of the Rydberg laser locks for this thesis is that they are generated using an EOM which is controlled by a variable frequency input that we scan to find a particular Rydberg state. The ULE lock is used to achieve a linewidth that is narrow compared to the lifetime of the Rydberg state, typically 10-100 kHz [111, 130], allowing quantum gates to be performed.

Rydberg B

Our home-built Rydberg laser which we call Rydberg B, passes through a tapered amplifier to increase the power available and frequency doubled via cavity-enhanced second harmonic generation (SHG) [132] to obtain green light at 509 nm. The linewidth of this laser was measured to be $\sim$ 130 Hz at 509 nm [130]. The laser pulses are intensity controlled using an 80 MHz AOM and coupled into PM

fiber, giving $\sim$ 100 mW of available green light at the atoms with σ^+ circular polarisation. To increase the power available at the atoms we later removed the AOM and used only mechanical shutters to control the Rydberg laser pulses giving $\sim$ 140mW of green light at the atoms.

SolsTiS

The SolsTiS ECD-X laser is a commercial Ti:Sapph laser from MSquared and was installed to provide a well-stabilised narrow-linewidth laser with an increase of the power available at the atoms compared to Rydberg B. The main features of this laser are a Vedri V-18 (Coherent) pump laser, a SolsTiS module and an ECD-X frequency doubling module. The SolsTiS module is pumped with the Vedri V-18 laser to output a stable mode at 1018 nm which is frequency doubled to 509 nm by the ECD-X module. A pick-off from the SolsTiS module allows us to stabilise the laser to the ULE reference cavity giving a laser with a narrow linewidth and excellent frequency stability. The SolsTiS module inherently produces a linewidth $<$50 kHz without an external cavity, thus when coupled to the ULE cavity in our experiment, we expect a narrower linewidth compared to the home-built Rydberg B laser ($\leq$ 130 Hz), however we have not measured this directly.

The ECD-X module is used to improve the efficiency of frequency doubling by directing the fundamental laser beam into an enhanced cavity (in conventional methods of single pass frequency doubling using non-linear crystals the efficiency is very low, typically 0.01%). When the beam is correctly aligned the intensity of the fundamental beam increases inside the ECD-X module. The cavity mirrors, except the input coupler, are highly reflective at the fundamental mode such that this setup generates an approximate Fabry-Perot cavity. Control electronics are used to lock to the maximum intensity within the cavity, found by varying the cavity length through piezo modulation of a cavity mirror, to generate interference fringes. The ECD-X module uses the Hansch-Couillaud technique [128] to lock the enhanced cavity to the fundamental laser mode.

The laser is then controlled in the same manner as the Rydberg B laser. The light output from the ECD-X passes through an 80 MHz AOM to stabilise intensity noise and to act as a fast switch for generating pulses at the atoms. The light is coupled into a PM fiber and provides up to 190 mW of green light at the atoms with σ^+ circular polarisation. There is also a mechanical shutter after the PM fiber to prevent any leakage light reaching the atoms.

9.2 Raman Laser

Raman transitions between the qubit states $|1\rangle$ and $|0\rangle$ are achieved using an 852 nm home-built ECDL which we call the Raman laser, the schematic of which is shown in Fig. 9.2(a). The 852 nm diode (Eagleyard: EYP-RWE-0860-06010-1500-SOT02-0000) can output 100 mW of power and we generate sidebands using an electro-optic modulator (EOM). The EOM operates at ± 4.6 GHz, half the hyperfine ground state splitting, and uses a Haubrich-Dornseifer-Wynands (HDW) interferometer [133] to suppress the carrier and second order sidebands, resulting in the first order sidebands equally sharing $> 95\%$ of the amplitude, as shown in Fig. 9.2(b).

The light from the Raman laser is split into two optical paths using a beam splitter (BS); one for local addressing of the atoms and the other for global addressing. The local Raman beam has a $1/e^2$ beam waist 2.9 μm with pulse control provided by an -80 MHz AOM. The global Raman beam has a $1/e^2$ beam waist of 17 μm with an AOM modulated at +80 MHz to enable fast switching and to prevent coupling of the global beam to the EIT resonance in the demonstration of the CNOT gate (see Chapter. 11). Each beam path also has an independently controlled mechanical shutter in place to block any leakage light. The beams are coupled into polarisation maintaining fibers and the two paths are recombined on a polarising beam splitter (PBS) before passing through a waveplate entering the science chamber to address the atoms, giving the local Raman beam σ^+ circular polarisation and the global

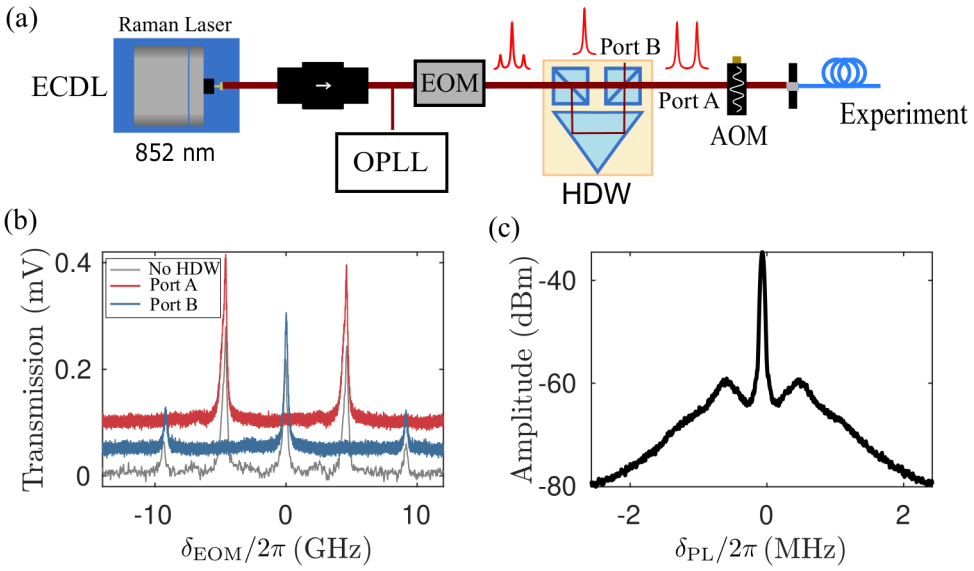

Figure 9.2: (a) A schematic of the Raman laser set-up, (b) the peaks generated by the EOM without the HDW lock (grey), the output at port A showing the first order sidebands with the carrier and second order sidebands filtered (red) and the output at port B showing the carrier and second order sidebands (blue), and (c) the frequency spectrum of the beatnote between the Raman and Qubit lasers.

σ^- circular polarisation.

The carrier of the Raman laser is stabilised using an optical phase-lock loop with the Qubit laser so that the detuning of the Raman laser at the atoms is $\Delta_A/2\pi = +870$ MHz from the $\left|6S_{1/2}, F = 4\right\rangle \rightarrow \left|6P_{3/2}, F' = 5\right\rangle$. The phase-lock enables the Raman laser to inherit the stability of the ULE cavity to which the Qubit laser is locked, and the absolute detuning from the transition, without the need to couple the Raman laser to the ULE cavity. This stability is crucial to perform the CNOT gate in Chapter. 11.

9.2.1 Optical Phase-Lock Loop

To perform the EIT based CNOT gate described in Sec. 6.2, the excitation lasers need a common detuning from the excited state $\left|6P_{3/2}, F' = 5\right\rangle$. The HDW lock on the Raman laser is not stable enough to ensure a constant detuning from the

$\left|6P_{3/2}, F' = 5\right\rangle$ state, but the ULE cavity is. We therefore use an optical phase-lock loop (OPLL) to generate feedback that enables the Raman laser to be phase-locked at a detuning equal to that of the Qubit laser. We use a design for the OPLL based on the design in Ref.'s [134, 135].

An optical phase-lock loop is a way to electronically control the optical phase difference between a 'slave' laser and a 'master' laser (sometimes called the local oscillator or reference laser) [136, 137]. The phase difference is converted in to a voltage difference and is used to generate an error signal to lock the slave laser thus generating a fixed phase relation between the two lasers.

By expressing the electric fields of the lasers, labelled A (Qubit) and B (Raman), as [136],

$$\boldsymbol{E}_A(t) = E_a e^{i(\omega_A t + \varphi_A(t))}, \tag{9.1}$$

$$\boldsymbol{E}_B(t) = E_b e^{i(\omega_B t + \varphi_B(t))}, \tag{9.2}$$

with field amplitudes $E_{a,b}$, oscillating frequencies $\omega_{A,B}$ and laser phase fluctuations $\varphi_{A,B}$ (which can be set to zero), the instantaneous phase of the lasers is,

$$\phi_A(t) = \omega_A t + \varphi_A(t), \tag{9.3}$$

$$\phi_B(t) = \omega_B t + \varphi_B(t). \tag{9.4}$$

This gives a frequency difference,

$$\Delta\omega = \frac{d}{dt}\Delta\phi = \frac{d}{dt}[\phi_A(t) - \phi_B(t)]] = (\omega_A - \omega_B) + [\dot{\varphi}_A(t) - \dot{\varphi}_B(t)]. \tag{9.5}$$

From this we can see that if there are no phase fluctuations between lasers A and B, the phase difference $\Delta\varphi(t) = \varphi_A - \varphi_B$, is constant leading to a fixed frequency difference between the lasers.

A typical set-up of an OPLL is shown in Fig. 9.3. For each laser, Qubit (master laser) and Raman (slave laser), ~1 mW of light is picked-off from the main experiment using a polarising beamsplitter (PBS). The beams are then overlapped on a 50:50 beam splitter (BS) and superimposed onto a photo-detector (Thorlabs DET08CFC/M) which converts the optical signal to an electronic one with

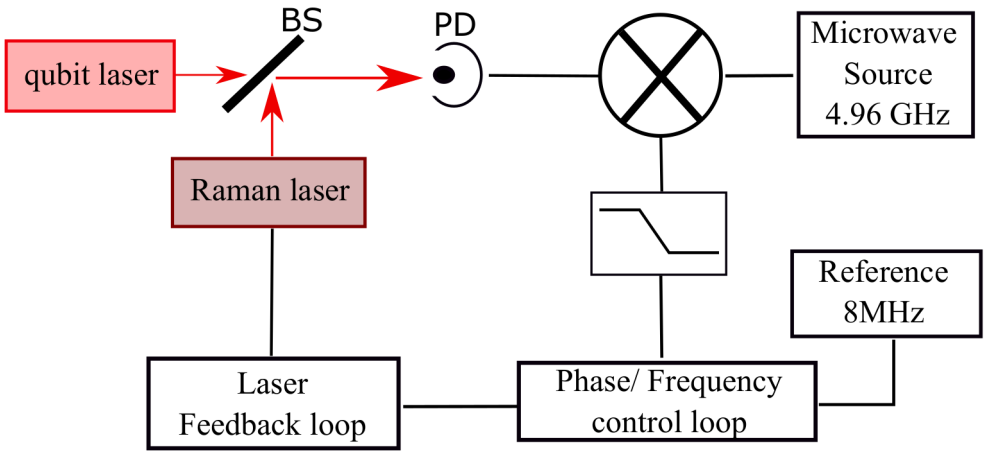

Figure 9.3: Schematic of the beat set-up used to phase lock the lasers. Light from the qubit and Raman lasers are combined on a beam splitter (BS) and converted to an electrical signal by the photodiode (PD). The electrical signal is mixed with a microwave reference and filtered through a low-pass filter. A phase-frequency control loop is used to generate an error voltage from which the Raman laser can be locked.

intensity,

$$I(t) = I_A + I_B + 2\sqrt{I_A I_B}\cos[(\omega_A - \omega_B) + (\dot{\varphi}_A(t) - \dot{\varphi}_B(t))]. \tag{9.6}$$

Using a spectrum analyser, a beatnote is observed with frequency

$$\nu_{\text{beat}} = \frac{\omega_A - \omega_B}{2\pi} = 4.52 \text{ GHz}. \tag{9.7}$$

This beatnote is then mixed with a stable microwave signal (HP 83731B) with frequency $\nu_{\mu\text{wave}} = 4.6$ GHz, generating the sum $(\nu_{\mu\text{wave}} + \nu_{\text{beat}})$ and difference $(\nu_{\mu\text{wave}} - \nu_{\text{beat}})$ frequencies of the mixed signal. These signals are filtered through a low-pass filter to remove the high frequency signal leaving only the low frequency signal at 80 MHz. This mixed 80 MHz signal is first sent through a prescaler that divides the frequency by an integer between 10 and 80, the value of which is set via three jumpers that control the voltage applied to three ports of the prescaler. In our case the prescaler divides the 80 MHz signal by 10 so that this frequency matches the 8 MHz reference signal provided by a signal generator (Rigol DS1054).

The beat and reference signals are digitised and sent through a digital phase/frequency

discriminator (PFD) chip (AD9901KQ) that detects the phase and frequency difference between them. The output generated by the PFD is split into fast and slow error signals, separated using high and low pass filters. The fast error signal is sent through a loop filter directly to the DC current modulation of the Raman laser (slave). The slow error signal is connected to a lock-box that is a standard PI controller, to give control over the grating piezo.

To lock the Raman laser, the fast error signal is passed through a feedback loop connected directly to the laser diode. The current passing to the laser diode is controlled by a n-type Junction-Field-Effect-Transistor (JFET) which enables us to control the frequency of the laser diode. The fast error input signal is attenuated by a variable resistor and is then applied to the gate of the JFET. When less current flows through the JFET, the gate current is low and more current flows through the laser diode resulting in an increase in frequency. We can use this feedback to lock the Raman laser frequency to the Qubit laser frequency with a constant phase relationship.

The frequency spectrum of the beatnote generated by the error signal is shown in Fig. 9.2(c) which has two distinct servo bumps indicating the bandwidth of the lock, where the feedback of the control loop is no longer very efficient due to a phase lag [134]. We calculate the linewidth of the beatnote to be 6.71 kHz which is limited by the bandwidth of the spectrum analyser.

9.3 Microwave Antenna

A microwave antenna was installed in the experiment to allow us to perform ground state rotations between the qubit states $|1\rangle \rightarrow |0\rangle$.

A schematic of the RF components to enable microwave addressing of the atoms is shown in Fig. 9.4. The microwave source is a HP 83624A and is set to $\nu_{\mu\text{wave}} = 9.192,645,490$ GHz to match the ground state hyperfine splitting of the caesium atom [89]. The microwave signal is amplified using two Kuhne Electronic

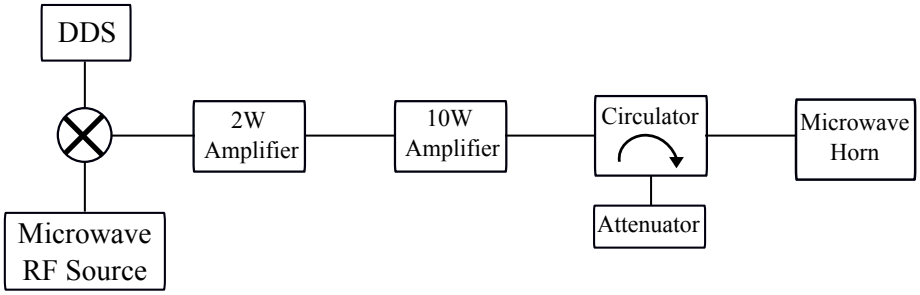

Figure 9.4: (a) Schematic showing the set-up of the RF microwave components leading to the microwave horn.

amplifiers; 2 W (KU PA 9001250 2A) and 10 W (KU PA 10001050-8B), which are connected to a circulator (Atlantic Microwave ACC-20220-SF-SF-SF) to prevent back reflection from the microwave horn. The signal is connected to a standard gain horn (Flann 16240) with 20 dB ($\approx$ 1W) gain via a waveguide to SMA coax adaptor (Flann 16094-SF40).

The microwave horn is placed outside of the science chamber, near a viewport 45° to the z-axis as shown in Fig. 9.1. The microwaves have a linear polarisation but due to the placement of the horn have a strong anisotropy. The microwave pulse is controlled using a DDS board such that the RF can be toggled on and off during an experiment sequence, enabling a microwave pulse with a controllable duration and, frequency control so that the microwave frequency can be scanned. The optimisation of the ground state microwave transitions is presented in Sec. 10.3.

9.4 Summary

This chapter describes the excitation lasers that are used in the experiment to drive excitations to the Rydberg state and Raman transitions between the ground states. We gave an overview of each laser system, highlighting the important features such as the ULE cavity used to stabilise the Qubit and Rydberg lasers, and introduced the OPPL that is used to stably lock the Raman laser with the same detuning from $\left|6P_{3/2}, F' = 5\right\rangle$ state as the Qubit laser.

We also discussed the installation of a microwave antenna to the experiment set-up which will be characterised in Sec. 10.3.

Part IV

Single and Two-Qubit Operations

Chapter 10

Single Qubit Operations

In this chapter we discuss the optimisation of the Rydberg, Raman and microwave excitation pulses in a single atom basis. In each case, the experiment sequence is as follows; the atoms are loaded and imaged in the microtrap to determine if an atom is initially present, and are then optically pumped into the state $\left|6S_{1/2}, F = 4, m_F = 0\right\rangle = |1\rangle$. Following this a series of pulses are applied relevant to the operation being performed, before a second image is taken to detect the presence of an atom in the microtrap at the end of the sequence. The presence or absence of the atom in the second image is dependent on the operation performed between images and is used to determine the success of the operation on the qubits up to a small loss error. The probability to lose an atom due to heating during the imaging process is < 2 %, however other losses may occur which are addressed in the following sections where relevant.

The single qubit operations that are optimised in this chapter form the basis of the two-qubit CNOT gate demonstrated in Chapter 11.

10.1 Zeeman splitting of the hyperfine levels

To find the resonance between the qubit states in the experimental setting, we need to consider the differential light shift due to the trapping light, and the quadratic Zeeman shift caused by the application of a magnetic field along quantisation axis.

Applying a magnetic field, B, lifts the degeneracy of the magnetic sublevels $|F, m_F\rangle$ in each hyperfine manifold. The shift of each sublevel can be calculated using the Breit-Rabi formula [86, 138]

$$\Delta E_{F,m_F} = -\frac{\Delta E_{\text{hfs}}}{2(2I+1)} - g_I \mu_B m_F B \pm \frac{\Delta E_{\text{hfs}}}{2}\sqrt{1 + \frac{4m_F}{2I+1}x + x^2}, \tag{10.1}$$

where $x = (g_J - g_I)\mu_B B/\Delta E_{\text{hfs}}$. For clock state transitions, represented in experiment notation as $|1\rangle$ and $|0\rangle$, the shift is second order and simplifies to

$$\Delta E_{|1\rangle\to|0\rangle} = \frac{(g_J - g_I)^2 \mu_B^2}{2\Delta E_{\text{hfs}}} B^2. \tag{10.2}$$

In our experiment, the B-field applied along the quantisation axis has magnitude $\sim$7.5 G and the pre-factor of eqn. 10.2 is 427 Hz/G^2 [89] for caesium. This gives an expected quadratic Zeeman shift of $\delta_B/2\pi = +24$ kHz from the centre of mass detuning between the hyperfine levels.

The differential AC Stark shift due to the trapping light comes from the fact that an atom in $F = 4$ experiences a slightly stronger light shift than an atom in $F = 3$, and is given by [82]

$$\hbar\delta_{\text{LS}} = U_0(\Delta_{\text{eff}}) - U_0(\Delta_{\text{eff}} + \delta_{\text{hfs}}), \tag{10.3}$$

where U_0 is the trap depth, Δ_{eff} is the effective detuning of the weighted contributions of the D_1 and D_2 lines and δ_{hfs} is the hyperfine splitting between the $F = 4$ and $F = 3$ levels. In the experiment, the trap depth $U_0 = 300$ μK which gives a calculated value of $\delta_{\text{LS}}/2\pi = 800$ Hz.

The atomic resonance frequency, w_0, between the qubit states $|0\rangle$ and $|1\rangle$ is modified according to

$$\omega_0 = \delta_{\text{hfs}} + \delta_{\text{LS}} + \delta_B + \delta' \tag{10.4}$$

where δ_{hfs} is the hyperfine splitting, δ_{LS} is the differential light shift, δ_B is the quadratic Zeeman shift and δ' includes all other unknown frequency shifts. This gives a total detuning $\Delta = \omega_0 - \omega$, where ω is the frequency of the exciting radiation - in this case either the Raman or the microwave pulse.

The value of $\delta_{\text{hfs}}/2\pi = 9.192,628,47$ GHz is set using a GPS reference which differs from the field-free caesium clock frequency by -3.3 kHz [89]. To find Δ using the Raman or microwave pulses experimentally, we set the value of $\delta_{\text{hfs}} = 0$ in the experiment frame allowing us to perform a spectroscopy measurement to find the exact resonance with respect to δ_{hfs}.

10.2 Raman Transitions

The Raman laser, as the name suggests, drives Raman transitions between the qubit states $|1\rangle \rightarrow |0\rangle = |F = 3, m_F = 0\rangle$, using the laser system is described in Sec. 9.2. The atomic configuration is described by the three-level Λ-system discussed theoretically in Sec. 4.1, which drives Raman transitions under the condition that the laser coupling $\Omega_p \ll |\Delta_A|$, where $\Delta_A = +870$ MHz is the detuning from the excited state $|P\rangle = \left|6P_{3/2}, F' = 5\right\rangle$ at the atoms, such that the system can be approximated as an effective two-level system, eliminating the dependence on the excited state.

To optimise the transfer of atoms between the qubit states $|1\rangle \rightarrow |0\rangle$, we performed a spectroscopy for the locally and globally addressing beams to find the two-photon resonance of each. The spectroscopy was followed by a Rabi flop to determine the Rabi frequency from which a π-pulse can be calculated to perform a full population inversion between $|1\rangle \rightarrow |0\rangle$. This π-pulse is equivalent to a X gate denoted $X(\pi)$.

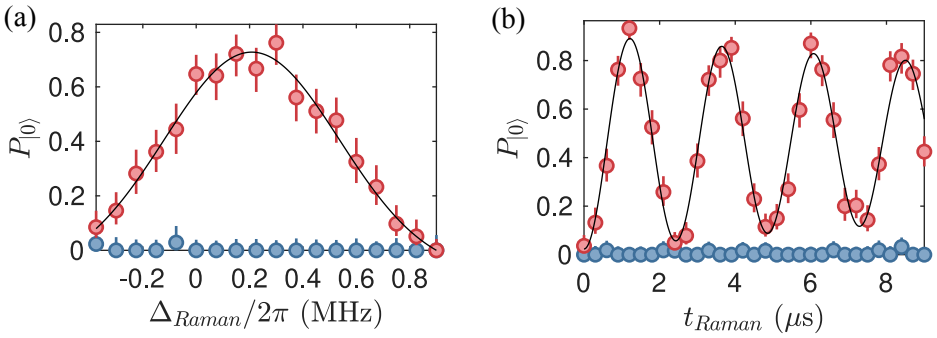

Figure 10.1: (a) Local Raman spectroscopy measured with respect to the hyperfine splitting δ_{hfs} to give an effective two-photon detuning $\Delta_{\text{Raman}} = 0.25(1)$ MHz. (b) Local Rabi flop with the detuning adjusted for the shift due to the trapping potential, giving $\Omega/2\pi = 0.43(1)$ MHz. In each case the local Raman beam effects only the target atom (red) leaving the control atom (blue) in its initial state, with an error < 1 %.

Local Raman Transitions

The locally addressing Raman laser has 65 nW of power with σ^+ circular polarisation and is focused with a $1/e^2$ beam waist of 3 μm to address the target atom only. The spectroscopy is performed by scanning the microwave frequency of the sidebands created by the EOM until maximum transfer is achieved corresponding to the two-photon resonance. The EOM is calibrated so that $\delta_{\text{hfs}} = 0$ in the frame of the experiment and the detuning is scanned w.r.t. δ_{hfs}. The AC Stark shift associated with the Raman light is much larger than any of the other shifts given by Eq. 10.4, and is dependent on the power of the beam. We use a spectroscopy measurement to find the two-photon resonance.

The pulse duration used during the spectroscopy is equivalent to that of area π which in this case is $t_\pi = 1.16$ μs. The data in Fig. 10.1(a) are fitted to the function (See Sec. 3.1)

$$P_{|0\rangle}(t_\pi) = \frac{\Omega^2}{\Omega^2 + \Delta^2} \sin^2\left(\sqrt{\Omega^2 + \Delta^2}\frac{t_\pi}{2}\right), \tag{10.5}$$

where Δ is the effective two-photon detuning. From this equation we extract the two-photon resonance at $\Delta/2\pi = 0.25(1)$ MHz w.r.t. δ_{hfs}.

To optimise the pulse area for maximum transfer between the qubit states $|1\rangle \rightarrow |0\rangle$

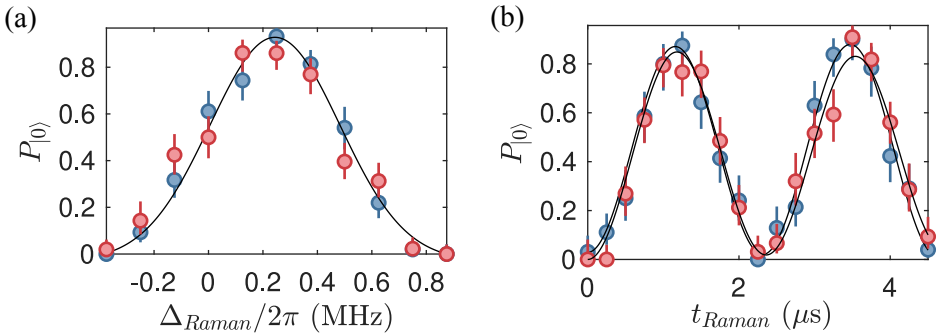

Figure 10.2: The Raman laser aligned equally on the atoms showing (a) global spectroscopy with two-photon resonance $\Delta_{\text{Raman}}/2\pi = 0.25(1)$ MHz and (b) global Rabi flop with Rabi frequencies $\Omega/2\pi = 0.43(1)$ and $0.42(1)$ MHz.

a Rabi flop is performed with the detuning set to the two-photon resonance. The local Raman pulse duration is scanned which maps out a Rabi oscillation as a function of the pulse duration as shown in Fig. 10.1(b) with fit given by Eq. 3.22 from which an effective Rabi frequency $\Omega/2\pi = 0.43(1)$ MHz is extracted. The Rabi frequency gives a full rotation from $|1\rangle \rightarrow |0\rangle$ for a local Raman pulse duration of 1.16 μs with this duration corresponding to the qubit gate $X(\pi)$.

Of particular note in Fig. 10.1 is that the local Raman beam only affects one atom (the target atom shown in red) and the effect on the other atom (control atom in blue) is < 1 % thus demonstrating excellent alignment of the local Raman beam on the desired atom. The alignment of the local Raman beam such that it effects the target atom but not the control atom is a key setting for the CNOT gate allowing the target atom to be well-defined.

Global Raman Transitions

Using the same procedure as in the local case, we scan the EOM sideband frequency to find the two-photon resonance with the global Raman beam and then perform a Rabi flop to get the Rabi frequency. There is 2.2 μW of power in the global beam which was chosen so that the two-photon resonance of the global beam matches that of the local. The $1/e^2$ beam waist of the global beam is 15 μm and is aligned

on the atoms such that both atoms are equally addressed.

The results of the global Raman spectroscopy are shown in Fig. 10.2(a) and fitted using Eq. 10.5 from which the two-photon detuning $\Delta/2\pi = 0.25(1)$ MHz is extracted for both atoms. The Rabi oscillations are shown in Fig. 10.2(b) fitted using Eq. 3.22 with Rabi frequencies $\Omega/2\pi = 0.43(1)$ and $0.42(1)$ MHz observed on the atoms. The almost equal Rabi frequency of each atom in response to the global Raman beam shows that the beam is well-aligned to address both atoms equally. The difference in Rabi frequency between the atoms is small enough that it does not effect the transfer between the qubit states on the time scales the experiments are carried out on. Using a global Raman pulse duration of 1.16 μs is equivalent to the gate rotation $X(\pi)$ for this beam.

The Raman transfer between $|1\rangle \rightarrow |0\rangle$ is only ~ 85 % efficient when optimised in both the local and global cases. This is primarily due to imperfect optical pumping and working with a relatively small detuning $\Delta_A/2\pi = +870$ MHz from the transition $\left|6S_{1/2}, F = 4\right\rangle \rightarrow \left|6P_{3/2}, F' = 5\right\rangle$ which may cause scattering and hence losses from the experiment basis. To try to overcome this problem we added a microwave antenna to the experiment. While this results in slower pulses, we do see an improvement in the transfer between $|1\rangle \rightarrow |0\rangle$ using microwaves compared to the Raman laser. The optimisation of the microwave pulses is presented Sec. 10.3.

10.3 Ground State Microwave Transitions

Microwave transitions between the qubit states $|1\rangle \rightarrow |0\rangle$ form a two-level system as described in Chapter 3, where the qubit states $|1\rangle$ and $|0\rangle$ represent the energy levels $|e\rangle$ and $|g\rangle$ respectively, and is schematically shown in Fig. 10.3(a). The microwaves due to their wavelength address both atoms equally with about 1 W of power.

Following Eq. 10.4, the shift of the microwave resonance $\Delta_{\mu\text{wave}}$ of the two-level system is dominated by the quadratic Zeeman shift δ_B, as δ_{hfs} deviates by -3.3 kHz

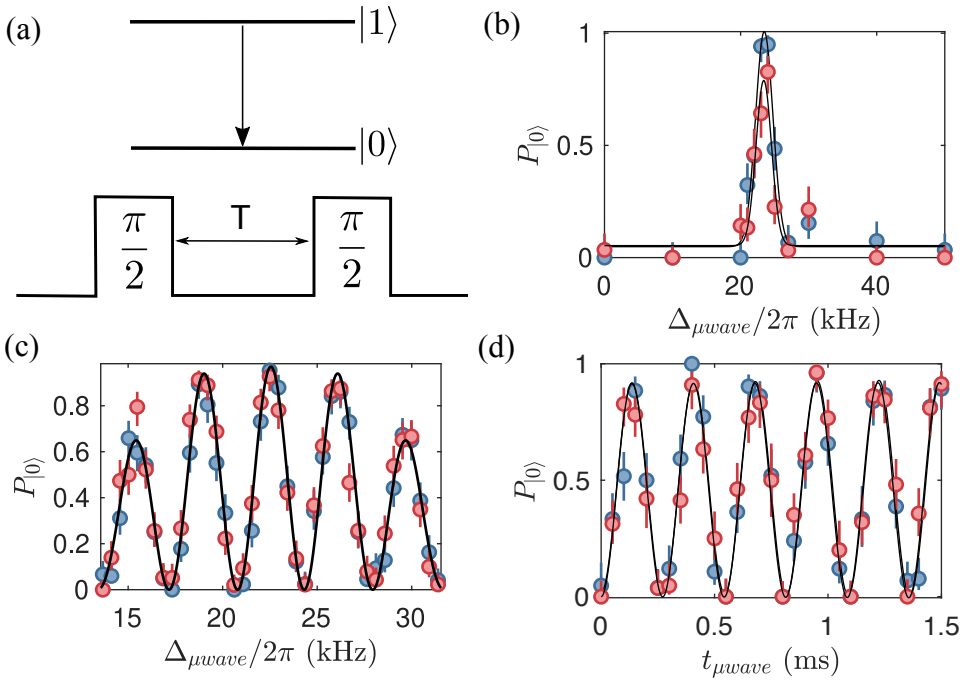

Figure 10.3: (a) Upper: Two-level energy level for microwave transitions between qubit states $|1\rangle \rightarrow |0\rangle$, Lower: Ramsey sequence used to fine tune the microwave transition. (b) Rabi sequence scanning the microwave detuning to find the resonance accounting for the Zeeman shift between the two qubit states. (c) Microwave Ramsey spectroscopy with gap time T = 200 μs scanning in the frequency domain, with a fixed microwave pulse duration and, (d) microwave Rabi flop with $\Omega/2\pi = 3.67(6)$ kHz.

from the standard resonance defining the second, $\delta_{LS}/2\pi = 800$ Hz and δ' is expected to be small, whereas $\delta_B/2\pi = +24$ kHz which is much larger than the other shifts. We use the calculated Zeeman shift $\delta_B/2\pi = +24$ kHz as a reference point from which to scan $\Delta_{\mu\text{wave}}$ to find the microwave resonance

In the first instance we apply a single microwave pulse for a duration of 1 ms to find a broad resonance centred around $\Delta_{\mu\text{wave}}/2\pi = +23.5$ kHz as shown in Fig. 10.3(b). To fine tune the microwave resonance we use Ramsey spectroscopy (see Sec. 3.5) scanning in the frequency domain to optimise the exact resonance of the microwave pulse. A schematic of the Ramsey sequence is illustrated in Fig. 10.3(a) where two microwave $X(\pi/2)$ rotations are applied separated by T= 200 μs to generate a Ramsey fringe which is fit to Eq. 3.28. Fig. 10.3(c) shows the resultant Ramsey

fringes which have a resonance $\Delta_{\mu\text{wave}}/2\pi = 23.2(1)$ kHz.

To optimise the transfer between $|1\rangle$ and $|0\rangle$, a Rabi flop is performed with the microwave detuning set to the resonance $\Delta_{\mu\text{wave}} = 23.2$ kHz. In this case a single microwave pulse is applied for a variable duration $t_{\mu\text{wave}}$. The resultant oscillation is shown in Fig. 10.3(d) and is fit to Eq. 3.22 from which the microwave Rabi frequency $\Omega/2\pi = 3.67(6)$ kHz is extracted. By iterating between Ramsey spectroscopy and Rabi flopping we optimise the microwave resonance and Rabi frequency to maximise the transfer between qubit states.

The optimised microwave pulses have a transfer efficiency of ∼95 % which is superior to that achieved with the Raman laser. The microwave pulses are however not 100 % efficient and we expect this is mainly due to the problem we have with imperfect optical pumping, which can cause off-resonant excitation to other m_F levels.

10.3.1 Local Microwave Operations

Using microwaves which have a wavelength $\lambda_{\mu\text{wave}}$ ∼1 cm to drive transitions between the qubit states $|1\rangle \rightarrow |0\rangle$ works well globally but cannot be used to locally address an atom in the experiment as they are only separated by $\sim 5\mu$m. To enable local addressing of an atom we use the Qubit laser (described in Sec. 9.1.1) to apply a local AC shift on the control atom to shift this atomic site out of resonance with the microwave rotation. This enables us to keep the control atom in it's initial state while the target atom undergoes a microwave rotation and is unaffected by the Qubit laser. We do this following the method of Xia *et al.* [139].

Applying the Qubit laser to the control site, essentially detunes the microwave resonance by a factor Δ equivalent to the AC Stark shift of the Qubit laser on the control atom. The detuning suppresses the microwave qubit rotation by a factor Ω^2/Δ^2, however there is a trade-off between the suppression of the microwave field for small values of Δ and, the excessive photon scattering from the Qubit laser at

large values of Δ.

The work presented by Xia *et al.* [139] shows that there is an optimal choice of Δ that minimises the off-resonant coupling to the target atom, therefore leaving the qubit state of the target atom unaffected by the AC Stark shift from the Qubit light. The optimal detuning to achieve this occurs when $\Delta = 4n\pi$, for an integer n. This means that for a resonant microwave rotation of area $\theta = \Omega t$, the minimal coupling to the target site occurs when

$$\frac{|\Delta|}{\Omega} = \sqrt{\frac{16n^2\pi^2}{\theta^2} - 1}. \tag{10.6}$$

The first local minimum occurs for a microwave $X(\pi)$ rotation with $\theta = \pi$, at $|\Delta| = \sqrt{15}\Omega$. For a microwave $X(\pi/2)$ rotation, $\theta = \pi/2$, has minimal coupling when $|\Delta| = \sqrt{63}\Omega$.

The measured microwave Rabi frequency is $\Omega/2\pi$ =3.67(6) kHz, substituting this into $|\Delta| = \sqrt{15}\Omega$ and $|\Delta| = \sqrt{63}\Omega$ gives $|\Delta|/2\pi = 14.21(7)$ kHz and $|\Delta|/2\pi = 29.13(7)$ kHz for microwave $X(\pi)$ and $X(\pi/2)$ rotations respectively. The rotation on the control atom induced by the Qubit laser is equivalent to a rotation $Z(\theta)$ where θ is the rotation angle described by the evolution around the Bloch sphere - in essence there is a phase accumulation on the control atom which can be measured by varying the time the control atom is exposed to the Qubit laser.

To calibrate the AC Stark shift induced by the Qubit laser, we use microwave Ramsey spectroscopy to generate an oscillation as a function of the AC shift on the control atom. The sequence used is shown in Fig. 10.4(a), where a microwave $X(\pi/2)$ rotation is applied followed by a fixed free evolution time T during which the Qubit laser applies a $Z(\theta)$ rotation on the control atom for variable time $0 \leq T_q \leq T$, then a final microwave $X(\pi/2)$ rotation is applied. By applying the rotation $Z(\theta)$ during the free evolution time the control atom accumulates a phase with respect to the target atom which is mapped out by the final $X(\pi/2)$ rotation. Fitting the resultant oscillation to $A\cos(\Delta T_q + \phi) + B$ for some amplitude A, phase off-set ϕ and off-set B, the AC Stark shift Δ induced by the $Z(\theta)$ rotation can be extracted.

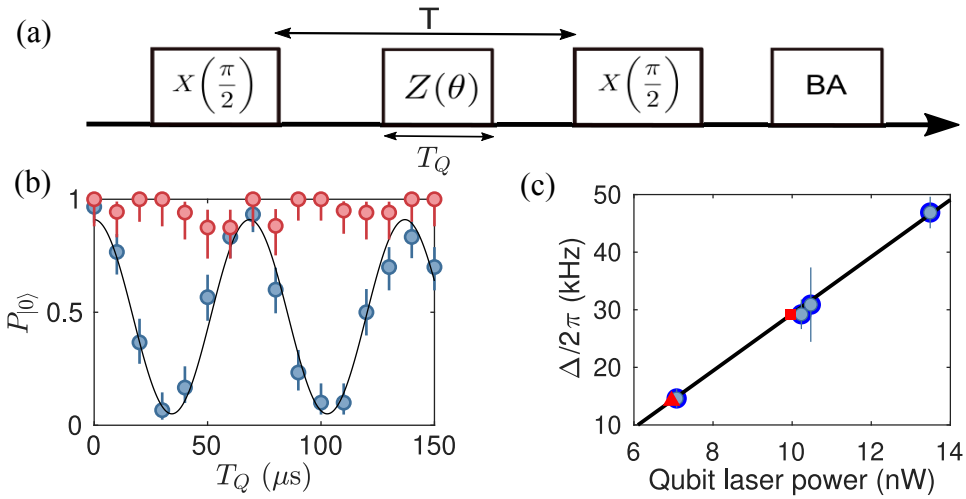

Figure 10.4: (a) Ramsey sequence used to measure the AC Stark shift Δ on the control atom, (b) the results of the Ramsey measurement for 7.1 nW of Qubit laser power and, (c) the measured AC Stark shift plotted against the power of the Qubit laser. The red triangle is the AC Stark shift for a $X(\pi)$ rotation and red square is for a $X(\pi/2)$ rotation.

The results of this are shown in Fig. 10.4(b) for 7.1 nW of Qubit laser power, from which we extract an AC Stark shift of $\Delta/2\pi = 14.6$ kHz, which closely matches the calculated value required for a microwave $X(\pi)$ rotation. In this figure there is no evidence of the Qubit laser affecting the target atom (red), with only the control atom (blue) oscillating as a result of the interaction with the Qubit laser, the fluctuations that are observed on the target atom are due to fluctuations in the rotation driven by the microwave pulse. In addition to choosing a detuning that minimises the effect of the AC Stark shift of the Qubit laser on the target atom, the Qubit laser is also focused so that it only addresses the control atom with an error of cross-talk < 1 %.

Repeating this modified Ramsey spectroscopy for different powers of the Qubit laser, we plot in Fig. 10.4(c), the extracted AC Stark shifts as a function of power. We find that Qubit laser powers of 7 nW and 9.9 nW give the appropriate shifts for microwave $X(\pi)$ and $X(\pi/2)$ rotations respectively. For microwave $X(\pi)$ and $X(\pi/2)$ rotations, the rotation of the control atom in the time that the AC Stark shift is applied is equivalent to a $Z(\pi)$ rotation.

10.4 Rydberg Excitations

In this section we discuss the optimisation of the two-photon excitation to the Rydberg state $|r\rangle = \left|81D_{5/2}, m_j = 5/2\right\rangle$ using the Qubit and Rydberg lasers described in Sec. 9.1. The Qubit laser is focused to a beam waist of 3 μm to address only the control atom such that the excitation to the Rydberg state only occurs on this atom, and no blockade effect is observed. The Qubit laser drives the lower photon of the excitation to $|r\rangle$ off-resonantly coupling the qubit state $|1\rangle$ and $|P\rangle = \left|6P_{3/2}, F' = 5\right\rangle$ at a detuning $\Delta_A/2\pi = +870$ MHz, as shown in Fig. 10.5(a). The upper photon comes from one of the Rydberg lasers, namely Rydberg B or SolsTiS, coupling from the detuned state $|P\rangle \rightarrow |r\rangle$. The Rydberg beam has a beam waist of 15 μm and is aligned to equally address both atoms.

We compare the difference in response of the atoms excited to $|r\rangle$ using the Rydberg B and SolsTiS lasers by finding the resonance of the two-photon excitation then optimising the transfer by observing a Rabi flop. From these measurements we can determine the Qubit laser pulse duration required to perform a pulse of area π to excite the control atom to the Rydberg state which will be used to influence the target atom when performing the CNOT gate in Sec. 11.5.

10.4.1 Rydberg State Detection

Detecting the Rydberg state of an atom in the experiment utilises the anti-trapping potential that a Rydberg atom experiences due to the dipole trapping beam. Excitations to the Rydberg state are performed with the trapping potential turned off, so that the rotations are performed on the atoms in free-space, then the dipole trapping light is reapplied and the Rydberg atoms are expelled from the trap. This enables us to distinguish between an atom in the Rydberg state and an atom in the qubit state $|1\rangle$.

To ensure this works efficiently the Rydberg lifetime τ_{Ryd} needs to be large compared to the time it takes for an atom to leave the trapping region τ_{t}. A Rydberg

state with a larger principal quantum number increases the detection efficiency as $\tau_{\mathrm{Ryd}} \propto n^2$. For $n > 50$ the error associated with the detection scheme is $\varepsilon_{\mathrm{D}} = \tau_{\mathrm{t}}/\tau_{\mathrm{Ryd}}$ [48].

This method of detecting the atom in the Rydberg state is indirect as experimentally we measure an atom in the state $|1\rangle$ and assume that the Rydberg population corresponds to $P_{|r\rangle} = 1 - P_{|1\rangle}$. Due to detection errors, imperfect optical pumping ($\varepsilon_{\mathrm{OP}}$) and false positive detections (ε_{F}, e.g. an atom is lost from the trap, not due to Rydberg excitation), the true Rydberg population ($P'_{|r\rangle}$) differs slightly. The detected Rydberg population has been estimated to relate to the true population according to [48]

$$P_{|r\rangle} = \varepsilon_{\mathrm{F}}\varepsilon_{\mathrm{OP}} + (1 - \varepsilon_{\mathrm{OP}}) \left[\varepsilon_{\mathrm{F}} P_{|1\rangle} + (1 - \varepsilon_{\mathrm{D}} + \varepsilon_{\mathrm{D}}\varepsilon_{\mathrm{F}}) P'_{|r\rangle}\right]. \tag{10.7}$$

Due to the cold atom temperature of 10 μK and good back-ground pressure $\varepsilon_{\mathrm{F}} < 0.01$, is small and from Sec 8.2 the optical pumping preparation error $\varepsilon_{\mathrm{OP}} = 1 - \mathcal{F} = 0.02$. The detection error $\varepsilon_{\mathrm{D}} \approx 0.05$ has been measured in previous work and gave a measured Rydberg population $P_{|r\rangle} = 0.9$ [110]. With the improvement in optical pumping efficiency by using the D_1 line, the work presented in this thesis is capable of measuring a Rydberg population $P_{|r\rangle} > 0.9$.

10.4.2 Rydberg Rotations

This initial experiment set-up for Rydberg excitation is the same as the previous sections: the presence of an atom in the microtrap is determined via fluorescence imaging, then the atoms are prepared in state $|1\rangle$ via optical pumping. The sequence then changes to enable Rydberg excitation and, importantly, Rydberg state detection.

The sequence of pulses used for Rydberg excitation are shown in Fig. 10.5(b). First the trapping light is turned off for a duration of 5 μs to prevent the atom excited to the Rydberg state being expelled from the microtrap. During this time the Rydberg laser is turned on for 5 μs and a Qubit laser pulse of variable duration

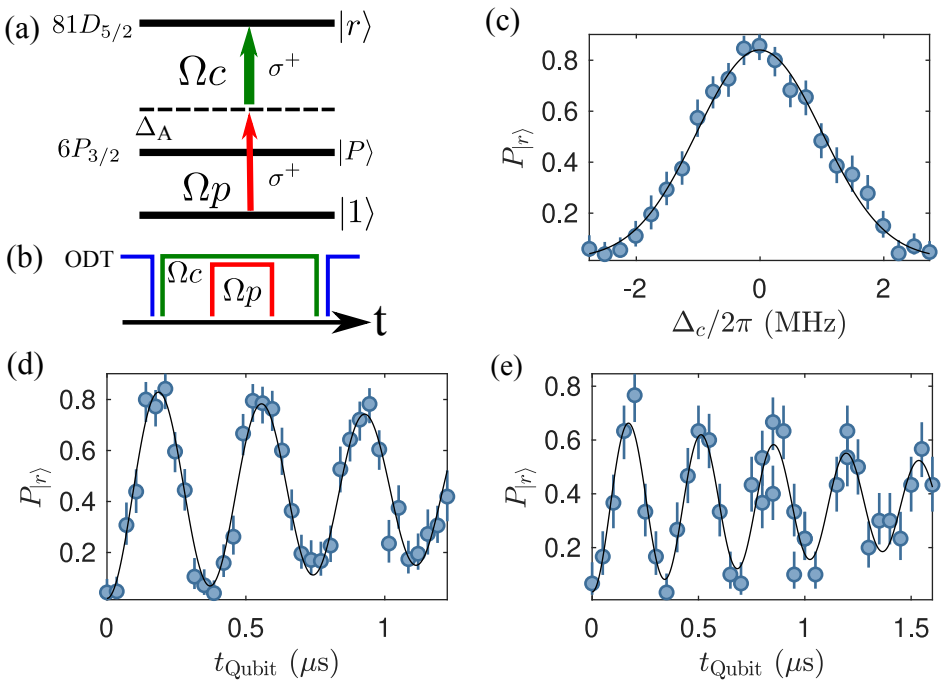

Figure 10.5: (a) Excitation scheme to the Rydberg level using the the ladder configuration with lower photon Ω_p provided by the qubit laser detuned from $|P\rangle$ by $\Delta_A/2\pi$ = 870 MHz and upper photon provided by the Rydberg laser with coupling Ω_c to the Rydberg state $|r\rangle$. (b) The pulses applied experimentally to drive a Rydberg excitation showing ODT (blue), Qubit (red) and Rydberg (green). (c) Rydberg spectroscopy achieved by scanning the sideband frequency of the Rydberg laser to find the two-photon resonance. Rabi oscillations are observed on the two-photon resonance with Ω_c provided by (d) the Rydberg B laser which has a Rabi frequency $\Omega/2\pi$ = 2.7 MHz, and (e) the SolsTiS laser with $\Omega/2\pi$ = 2.95 MHz.

is applied to excite the atom from $|1\rangle$ to $|r\rangle$. The trapping light is then re-applied to expel any atom in the Rydberg state. A second image of the atoms is then taken, with the loss of the control atom indicating excitation to $|r\rangle$.

To find the two-photon resonance we perform a spectroscopy by scanning the sideband frequency, Δ_c, of the Rydberg EOM until we see maximum loss of the atom indicating excitation to the Rydberg state. The Qubit laser is applied for a time corresponding to a π-pulse with a power of 218 nW. The spectroscopy is shown in Fig. 10.5(c) which is fit to Eq. 10.5 from which the two-photon resonance

is extracted. In this case we set the two-photon resonance Δ_c to zero when the resonance is found as the absolute value of the Rydberg EOM frequency changes at a rate of 1 Hz/s [130] in line with the ULE cavity lock drift.

Setting the Rydberg EOM frequency to the two-photon resonance we generate Rabi oscillations by varying the duration of the Qubit laser pulse and fit the oscillations to Eq. 3.22 to extract the Rabi frequency. The observed Rabi oscillation with Rydberg B is shown in Fig. 10.5(d) with Rabi frequency $\Omega/2\pi = 2.7$ MHz and a decay time $\tau = 2.24$ μs, achieved with 110 mW of Rydberg power and 218 nW of Qubit power. The Rabi oscillation with the SolsTiS laser is shown in Fig. 10.5(e) with Rabi frequency $\Omega/2\pi = 2.93$ MHz and a decay time $\tau = 1.69$ μs achieved with 170 mW of Rydberg power and 132 nW of power in the Qubit laser.

The Rabi frequencies for each laser are fairly similar but different Qubit laser powers have been used to achieve this. In addition for the Rydberg B results, the AOM had been removed to increase the power available at the atom which results in slower switching of the Rydberg pulses and presented some additional challenges in the experiments verifying the quantum nature of the gates.

The decay times in both cases are quite fast and can be attributed mainly the laser phase noise as a consequence of the ULE locks [48, 110]. Indeed reduction of the laser phase noise in Levine *et al.* [45] lead to an increase in the decay time of up to 27 μs. The CNOT gate demonstrated in Chapter 11 happens on a faster time scale than the decay time, so we do not address the laser phase noise on the experiment.

In general, the stronger coupling provided by the SolsTiS laser is favourable for working in the EIT regime when performing the CNOT gate, where it is essential that $\Omega_c \gg \Omega_p$ to maximise the EIT coupling. This laser provides more power and can be controlled on a fast timescale using an AOM, however technical issues with this laser lead to some measurements being performed with Rydberg B.

10.5 Conculsion

In this chapter we have described the experimental optimisation of single-qubit operations using microwave and optical pulses. We have achieved this by optically pumping the atoms into the qubit state $|1\rangle$ and used the state sensitive detection methods of applying a blow away pulse to distinguish between the qubit states $|0\rangle$ and $|1\rangle$ when performing ground state transitions, and used the anti-trapping potential of the Rydberg atoms to detect excitations to the Rydberg state.

Ground state rotations using microwave pulses were optimised using Ramsey spectroscopy to fine tune the microwave resonance and Rabi flopping to find the pulse duration corresponding to a $X(\pi)$ rotation. Single atom addressing of the microwave pulses is achieved by using the Qubit laser to provide an AC Stark shift on the control atom such that it is not resonant with the microwave pulse. An optical phase-lock loop was introduced to the Raman laser to provide a stable frequency reference between the Raman and Qubit lasers, which is a necessary component for the CNOT gate. The Raman laser pulse was optimised to maximise the transfer between $|1\rangle \rightarrow |0\rangle$. The Qubit and Rydberg lasers are stabilised to a high-finesse cavity and have been used to demonstrate two-photon excitation to the Rydberg state $\left|81D_{5/2}, m_j = 5/2\right\rangle$. We compared two lasers used to drive the upper photon of the Rydberg excitation one a home-built and the other a commercial which were optimised to have Rabi frequencies $\Omega/2\pi = 2.7$ MHz and 2.95 MHz respectively.

Chapter 11

Demonstration of a CNOT Gate

We demonstrate a CNOT gate based on the method detailed in Chapter 6 which was proposed by Müller *et al.* [52]. In our case we demonstrate the CNOT gate on a pair of trapped atoms separated by ~ 5 μm such that they are within the Rydberg blockade radius. As the CNOT gate is applied in the two-atom basis we only consider cases where both atoms are loaded into the microtraps in the first image. As a result of this each iteration of the experiment is the result of 200-500 measurements to build reliable statistics on which to base our results. These statistics are essential as the loading of the microtraps is stochastic which means an atom will load in a trap ∼50% of the time and we are only interested in cases when both atoms load which reduces the useful data collected to ∼25%.

The single qubit excitations optimised in Chapter 10 are the foundation of the excitation pulses that make up the CNOT gate. The control atom is addressed by the Qubit laser, the target atom is addressed by the local Raman laser and the Rydberg lasers are aligned globally on the atoms, as illustrated in Fig. 11.1(a). The Qubit laser drives the lower photon between $|1\rangle \rightarrow |r\rangle$ with strength Ω_A and detuning $\Delta_A/2\pi = +870$ MHz from the excited state $|P\rangle = \left|6P_{3/2}, F' = 5\right\rangle$. The Rydberg laser with coupling strength Ω_c provides the upper photon to complete the excitation to $|r\rangle$. Both the Qubit and Rydberg excitations are driven by σ^+ polarised light and the two-photon optimisation has been demonstrated in

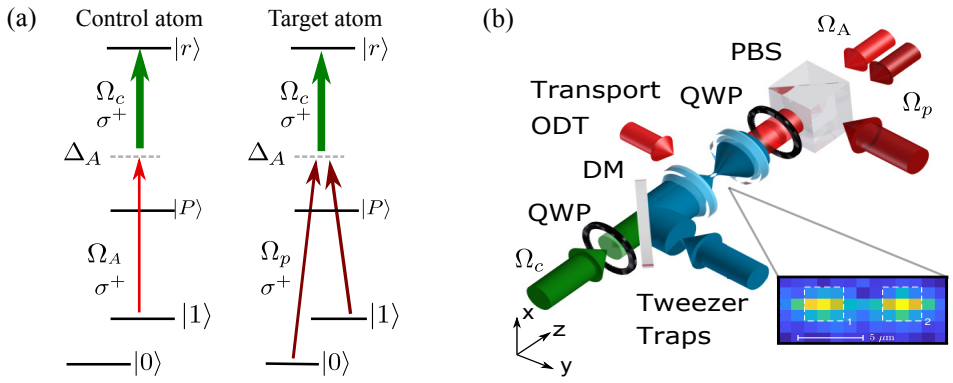

Figure 11.1: (a) Energy level excitation scheme used during the experimental implementation of the CNOT gate. The Qubit and Raman lasers with coupling strengths Ω_A and Ω_p respectively are detuned by Δ_A from the excited state $|P\rangle = \left|6P_{3/2}, F' = 5\right\rangle$, with the Qubit laser addressing only the control atom and the Raman laser addressing only the target atom. The Rydberg laser with coupling Ω_c, the Qubit laser and local Raman laser have σ^+ polarised while the global Raman laser has σ^- polarised light (b) Experiment set-up showing two atoms trapped in the optical dipole trap (ODT). The Qubit and local and global Raman lasers combine on a polarising beam splitter (PBS) and pass through a quarter waveplate (QWP) before entering the chamber. The trapping and Rydberg light are combined on a dichroic mirror (DM) before entering the chamber and counter-propagate with the direction of the Qubit and Raman lasers.

Sec. 10.4. The Rydberg level $|r\rangle = \left|81D_{5/2}, m_j = 5/2\right\rangle$ is chosen to maximise the angular matrix element for coupling between $|1\rangle$ and $|r\rangle$, and we use both the Rydberg B and SolsTiS lasers in separate demonstrations of the gate with varying results.

The Raman laser described in Sec. 9.2, drives Raman transitions between $|1\rangle \rightarrow |0\rangle$ and is detuned by $\Delta_A/2\pi = +870$ MHz from $|P\rangle$. The global Raman beam is aligned equally on both atoms and uses a square pulse controlled by an AOM and mechanical shutters to drive the Raman transition. The local Raman beam is aligned on the target atom and is used as a square pulse for state preparation and as the smooth pulse with coupling strength Ω_p to drive the qubit rotation $|1\rangle \rightarrow |0\rangle$. In the presence of the Rydberg laser with coupling strength Ω_c, the

coupling of the smooth and the Rydberg pulses is tuned to form a dark state such that EIT is observed. We discuss the characterisation of the smooth pulse and the tuning involved to find the EIT resonance in the next section.

The experiment set-up, including the alignment of the excitation pulses as they address the atoms is shown in Fig. 11.1(b). The Rydberg beam enters the chamber along the same axis as the microtrap light, which counter-propagate to the direction of the Qubit and Raman beams. The local and global Raman beams, and the Qubit beam combine on a polarising beam splitter (PBS) before entering the science chamber.

11.1 Smooth Pulse

The Raman laser described in Sec. 9.2 is used to apply the smooth pulse for the CNOT gate protocol which drives an adiabatic Raman transition between $|1\rangle \rightarrow |0\rangle$ in the absence of the Rydberg coupling Ω_c. The smooth pulse is generated using an arbitrary function generator (Rigol DG4162) connected to the AOM in the local Raman laser beam path to shape the pulse into a Gaussian shape rather than the typical square pulse. Fig. 11.2(a) shows the smooth pulse shape for pulse durations of 1.5 μs, 2 μs and 3 μs. The power of the smooth pulse is controlled by the amplitude of the DDS (direct digital synthesiser) which controls the AOM settings for the square pulse. We measure the instantaneous power of the smooth pulse using a fast photodiode and use the amplitude control of the smooth pulse to match the area under the smooth curve to that of a square π-pulse pulse simply by changing the amplitude on the DDS controller to rescale the shaped pulse power. The resulting scan for a 2 μs smooth pulse duration is shown in Fig. 11.2(b) where we see the area under the curve changes as a function of the amplitude from which the power of the smooth pulse can be extracted. The area under each curve for each amplitude setting is extracted and compared to the area of a square π pulse, finding that an instantaneous power of 14.5 nW has an area equal to π.

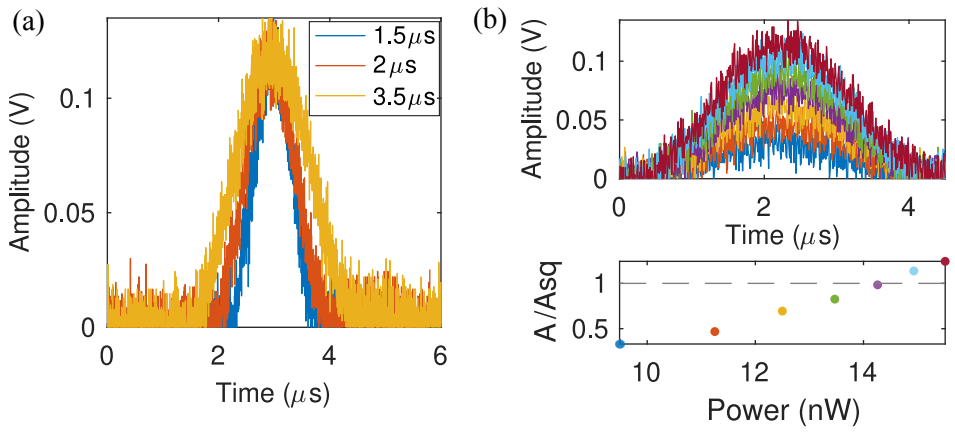

Figure 11.2: (a) Signals recorded on a photodiode of the smooth pulse shaped by a function generator for durations 1.5 μs, 2 μs and 3.5 μs. (b) The smooth pulse is applied for a duration of 2 μs and the amplitude of the AOM is scanned to measure the area under the curve. It is compared to that of a square π-pulse to extract the power.

The optimised settings for the smooth pulse are shown in Fig. 11.3 where we have chosen a 2 μs smooth pulse duration to allow an adiabatic transfer while still maintaining coherence of the Rydberg when performing the CNOT gate. The resulting Raman transfer as a function of the power is shown in Fig. 11.3(a) where we see around 85 % transfer, comparable to that achieved using the square pulse. At the optimised power setting a spectroscopy is performed finding the two-photon resonance at 0.25 MHz to match that of the local and global square Raman pulses. We also performed these measurements with smooth pulse durations ranging from 1.5 to 3.5 μs finding a duration of 2 μs was optimal for the EIT as will be discussed in the next section.

11.2 EIT on the Target Atom

A crucial element of the CNOT gate is being able to observe EIT on the target atom. The adiabatic transfer between the qubit states $|1\rangle \rightarrow |0\rangle$ was optimised in the previous section, so now we detail the steps taken to observe EIT on the target atom. To do this we apply the Rydberg laser and scan the detuning using

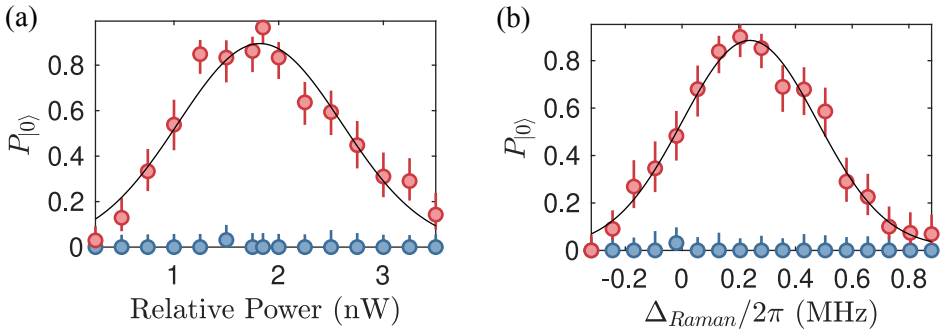

Figure 11.3: The optimisation of Raman transfer using the smooth pulse to maximise the transfer between $|1\rangle \rightarrow |0\rangle$ achieved by (a) scanning the power of the smooth pulse to have an area under the curve equal toπ, and (b) performing a spectroscopy to optimise the Raman transfer at 0.25 MHz.

the offset lock frequency sent to the EOM, in the same way as the single-qubit Rydberg excitations in Sec. 10.4, while applying the smooth pulse at the settings that will rotate the atoms between $|1\rangle \rightarrow |0\rangle$.

As before the atoms are optically pumped into the qubit state $|1\rangle$ and the dipole trapping light is turned off before the Rydberg light is applied. With the dipole trapping light off, the optimised smooth pulse is applied which will cause the qubit state to undergo the rotation $|1\rangle \rightarrow |0\rangle$ unless the EIT condition is satisfied, in which case the qubit will see a dark state and no rotation will take place. The Rydberg light is extinguished as the dipole trapping light is turned on then a blow away pulse is applied to remove any atom in the qubit state $|1\rangle$. In this way, when the EIT condition is satisfied the target atom will remain in $|1\rangle$ and be lost from the trap when the blow away pulse is applied, otherwise Raman transfer will occur and the atom will be rotated to $|0\rangle$ and remain in the trap.

We find the EIT resonance for smooth pulse durations ranging from 1.5 to 3.5 μs using the the Rydberg B and SolsTiS lasers in turn. In each case the Rydberg EOM frequency is scanned over a broad frequency range to map out the EIT resonances with 100 measurements taken per iteration.

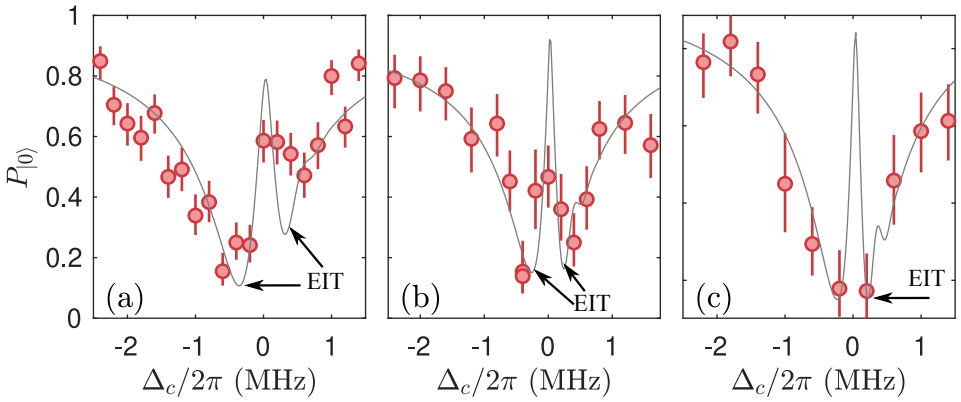

Figure 11.4: EIT data taken using the Raman and Rydberg B lasers compared to simulations using smooth pulses with durations (a) t = 2 μs, (b) t = 3 μs and (c) t = 3.5 μs.

11.2.1 EIT with Rydberg B

The first demonstration of EIT was achieved using Rydberg B with 73 mW of power available at the atoms. The resultant scans of the Rydberg EOM sideband frequency are shown in Fig. 11.4 for adiabatic pulse durations of 2 μs, 3 μs and 3.5 μs. The EIT resonances correspond to a minima in survival following blow away indicating the atom prepared in $|1\rangle$ has adiabatically followed the dark state during the smooth pulse evolution.

The data are compared to simulated results which are modelled using the the Hamiltonian given in Eq. 6.1 with experiment values used for the matrix elements. From the comparison there is a good correlation between the expected results and the observed data however it is clear there are some missing features in the observed data which we are unable to resolve experimentally. This is most likely due to the power in the Rydberg B laser which is quite low when trying to satisfy the condition $\Omega_c > \Omega_p$ that is required for optimal EIT. To improve the strong coupling, we switched to using the SolsTiS laser and repeated the measurements with a higher Rydberg coupling.

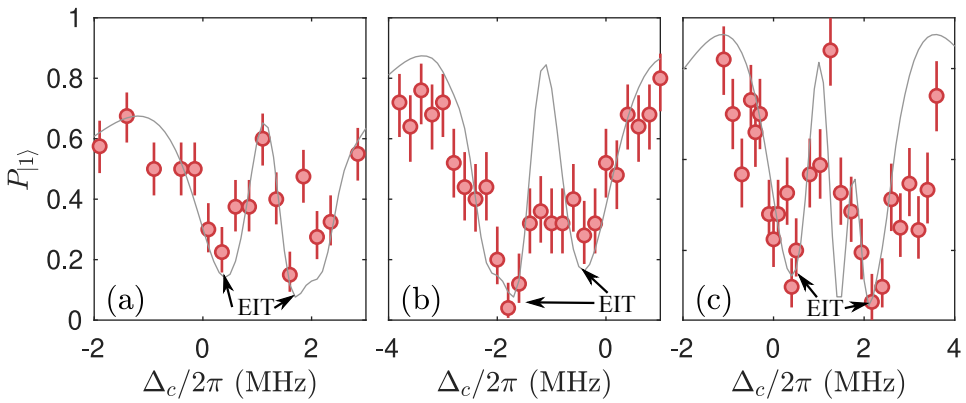

Figure 11.5: EIT data obtained with the Raman and SolsTiS lasers compared to simulations using adiabatic pulses of duration (a) t = 1.5 μs, (b) t = 2 μs and (c) t = 3 μs.

11.2.2 EIT with SolsTiS

The SolsTiS laser has a greater power capability than the Rydberg B laser with up to 190 mW available. The SolsTiS power on the day the EIT data presented here was taken was 170 mW which more fully satisfies the strong coupling $\Omega_c > \Omega_p$ required for EIT. We use Raman pulse durations of 1.5 μs, 2 μs and 3 μs and scan the Rydberg EOM sideband frequency to achieve the results shown in Fig. 11.5.

For each of the data sets there is a better match of the observed data to the simulated data, showing the effect of stronger coupling using the higher powered SolsTiS laser. We see that there are two well resolved dips for each Raman pulse duration indicating the EIT resonances with good contrast. In these data we also see more efficient EIT for longer Raman pulse durations due to the Raman pulse becoming more adiabatic as the pulse duration increases. The shortest pulse of duration 1.5 μs is too fast to efficiently couple to Ω_c, and a 3 μs pulse may be too slow to achieve a high-fidelity quantum gate as the longer the Raman pulse the longer the control atom remains in the Rydberg state, we therefore use a 2 μs pulse for the CNOT gate demonstration.

11.3 Two-Atom Readout

For neutral atom qubits, the dominant error in state detection is the inability to distinguish between an atom lost from the computational basis and an atom in state $|1\rangle$. As demonstrated by Gaetan *et al.* [140] it is possible to estimate the fidelity by extracting parameters from the statistics of two-atom survivals P_{00}, which is free from the errors due to loss, by careful analysis of the loss mechanisms of each atom. We consider two possible outcome states for the atoms: $\{x\}$ which contains atoms lost and those outside the computational basis, and $\{\bullet\bullet, \bullet\circ, \circ\bullet, \circ\circ\}$ corresponding to atom survival $\bullet$ and atom loss $\circ$. We can relate this new two-atom basis to measurements that can be performed with the state selective blow away pulse (A) or without (B).

When using the blow away beam, the measurement corresponds to the operators

$$A_{\bullet\bullet} = \sigma_{00}, \tag{11.1a}$$

$$A_{\bullet\circ} = \sigma_{01} + \sigma_{0x}, \tag{11.1b}$$

$$A_{\circ\bullet} = \sigma_{10} + \sigma_{x0}, \tag{11.1c}$$

$$A_{\circ\circ} = \sigma_{11} + \sigma_{1x} + \sigma_{x1} + \sigma_{xx}, \tag{11.1d}$$

and for the measurements without blow away,

$$B_{\bullet\bullet} = \sigma_{00} + \sigma_{01} + \sigma_{10} + \sigma_{11},, \tag{11.2a}$$

$$B_{\bullet\circ} = \sigma_{0x} + \sigma_{1x}, \tag{11.2b}$$

$$B_{\circ\bullet} = \sigma_{x0} + \sigma_{x1}, \tag{11.2c}$$

$$B_{\circ\circ} = \sigma_{xx}, \tag{11.2d}$$

where $\sigma_{ij} = |ij\rangle\langle ij|$ are the projection operators. From these equations we can see that $A_{\bullet\bullet}$ is not sensitive to single atom losses and provides a robust output measurement state.

As a result of this, when performing the CNOT gate measurements we rotate the atoms to the basis $|00\rangle$ before readout such that the measured output state is $A_{\bullet\bullet}$

when the blow away beam is applied. By repeating the measurements without the blow away pulse the measured output state is $B_{\bullet\bullet}$ which gives the normalisation for the total population remaining within the computational basis. Thus the corrected population in $|00\rangle$ is $P_{00}^{\text{cor}} = A_{\bullet\bullet}/B_{\bullet\bullet}$.

11.4 State Preparation

Before generating the CNOT gate matrix, we first measure how well the basis states can be prepared. We do this by applying a series of local and global rotations to the qubits following optical pumping to generate each of the two-qubit input states $|11\rangle, |10\rangle, |01\rangle$ and $|00\rangle$ in turn. We then leave the qubits in one of these states for a 5 μs trap drop to match the conditions that will be necessary when performing the CNOT gate, and again apply a series of local and global rotations to generate a state matrix. By turning off the trapping potential a fair comparison can be made between the state preparation fidelity and that achieved by the CNOT gate as the finite temperature of the atoms may results in unwanted losses or decay to states out of the computational basis. The state matrix can thus be used to provide an upper bound on the fidelity of the CNOT gate.

A state matrix is generated experimentally using two different techniques as illustrated in Fig. 11.6: Method A uses optical pumping to prepare the atoms in $|11\rangle$, and Method B follows optical pumping with a $X(\pi)$ rotation to put the atoms in $|00\rangle$ then a resonant blow away pulse is applied to remove any atom left in $|11\rangle$. Method B corrects for imperfect optical pumping by removing any atom outside the computational basis giving a purer state on which to perform the CNOT gate however the overall retention of the atoms is lower as a result. We find optical pumping polarisation purity is a problem in our experiment so using method B gives better results as it removes atoms outside of the computational basis.

After preparing the initial qubit state using method A or B, a series of X and Z gates are performed on the qubits to cycle through the two-qubit input states and

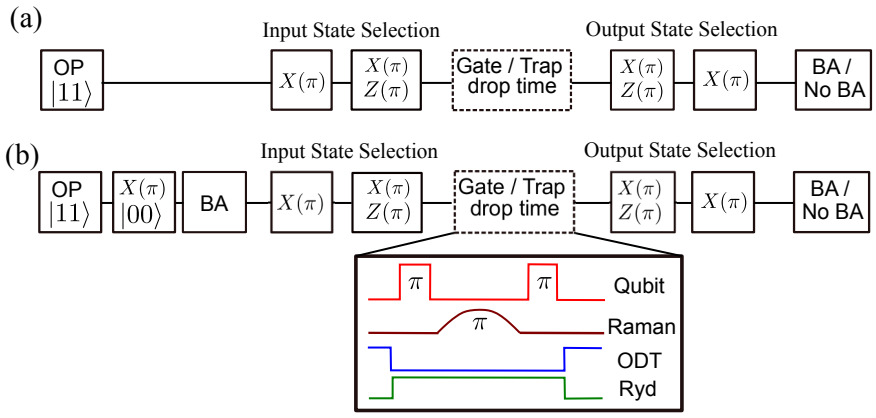

Figure 11.6: State preparation methods using optical pulses to prepare the states. (a) Method A - optical pumping only, (b) Method B - optical pumping followed by a global $X(\pi)$-rotation and blow away pulse. Inset gate sequence

then trapping light is then turned off for 5 μs. Next a second set of X and Z gates are performed to rotate the diagonal elements of the matrix into the two-qubit state $|00\rangle$ to allow a positive detection of the qubits rather than assigning loss to a particular state as is done in Rydberg detection. A final blow away pulse is applied to distinguish between the states $|1\rangle$ and $|0\rangle$ which gives us the measurement $A_{\bullet\bullet}$ for the state matrix. Repeating the state matrix without this final blow away pulse allows us to measure the atoms lost from the computational basis during the measurement, to give $B_{\bullet\bullet}$.

In addition to generating a state matrix using method A or B, we also have the choice of using optical or microwave rotations to perform the X and Z gates required cycle through each basis state. In the following sections we present the results of the state matrices prepared with optical and microwave rotations following methods A and B.

11.4.1 State Preparation with Optical Pulses

We generate a state matrix for each of the preparation methods A and B using optical input and output pulses sourced from the Raman laser. The Raman laser is applied locally to the target atom to perform a $X_{\text{local}}(\pi)$ rotation to switch between

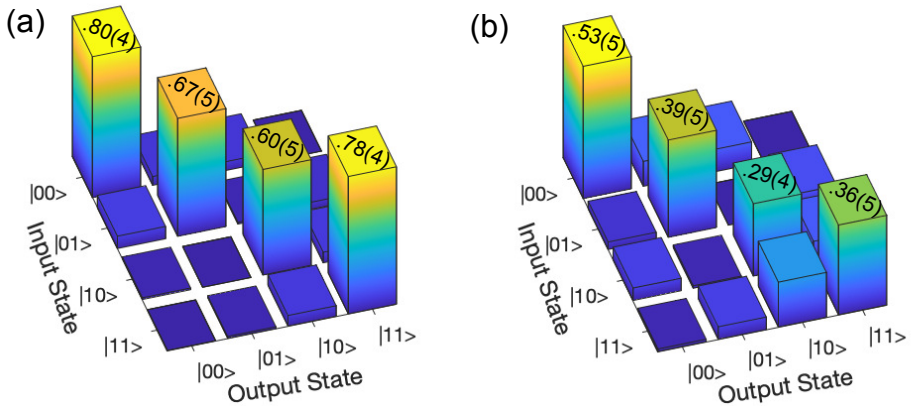

Figure 11.7: Uncorrected state matrix prepared using optical pulses for (a) method A - with optical pumping only with an uncorrected fidelity $\mathcal{F}^{\mathrm{A}}_{\mathrm{state}} = 0.71(2)$, and (b) with method B - optical pumping followed by a global rotation and blow away pulse which has an uncorrected fidelity $\mathcal{F}^{\mathrm{B}}_{\mathrm{state}} = 0.29(2)$.

the qubit states $|1\rangle \rightarrow |0\rangle$ as was shown in Sec 10.2. Similarly the global Raman pulse has been optimised to switch the qubit states of both atoms thus performing the rotation $X_{\mathrm{global}}(\pi)$ on the qubit states. Each of the desired two-qubit input states $|11\rangle$, $|10\rangle$, $|01\rangle$ and $|00\rangle$ can be realised by combining the rotations $X_{\mathrm{local}}(\pi)$ and $X_{\mathrm{global}}(\pi)$. The state matrices prepared using optical pulses only are shown in Fig. 11.7.

The state preparation matrix generated using method A shown, in Fig. 11.7(a), is

$$\mathrm{U}^{\mathrm{A}}_{\mathrm{state}} = \begin{pmatrix} 0.80(4) & 0.05(2) & 0.05(2) & 0.00(1) \\ 0.07(2) & 0.67(5) & 0.01(1) & 0.04(2) \\ 0.01(1) & 0.00(1) & 0.60(5) & 0.06(2) \\ 0.00(1) & 0.01(2) & 0.06(2) & 0.78(4) \end{pmatrix}, \tag{11.3}$$

where the value of each element is given by the log of the maximum likelihood estimate for the binomial distribution of the data taken in the two-atom basis and the errors given by the standard deviation of the elements. This state matrix has a fidelity $\mathcal{F}^{\mathrm{A}}_{\mathrm{state}} = \mathrm{Tr}\left(\mathrm{U}^{\mathrm{A}}_{\mathrm{state}}\mathrm{U}_{\mathrm{i}}\right) = 0.71(2)$, where U_{i} is the ideal state matrix and $\mathrm{U}^{\mathrm{A}}_{\mathrm{state}}$ is the measured state matrix. This matrix demonstrates how well the atoms can be rotated into the basis $|00\rangle$ before readout and gives an upper bound of

0.71(2) for the uncorrected fidelity of a CNOT gate prepared in this way.

Repeating the state matrix prepared using method A without the final blow away pulse so that all atoms in the qubit states $|00\rangle$ and $|11\rangle$ are detected in the final readout, allows us to correct the state matrix for losses of the qubits from the computational basis. Correcting the state matrix $\mathrm{U}^{\mathrm{A}}_{\mathrm{state}}$ for this loss gives a corrected state matrix,

$$\mathrm{U}^{\mathrm{A,cor}}_{\mathrm{state}} = \begin{pmatrix} 0.89(5) & 0.05(4) & 0.05(4) & 0.00(3) \\ 0.07(4) & 0.74(5) & 0.01(3) & 0.04(4) \\ 0.01(3) & 0.00(3) & 0.67(6) & 0.06(4) \\ 0.00(3) & 0.01(3) & 0.06(4) & 0.87(5) \end{pmatrix}. \tag{11.4}$$

The uncertainties of these corrected elements are calculated using the relation $\varepsilon = \sqrt{\varepsilon^2_{\mathrm{BA}} + \varepsilon^2_{\mathrm{noBA}}}$, where $\varepsilon_{\mathrm{BA}}$ and $\varepsilon_{\mathrm{noBA}}$ are the errors given by the standard deviation, on the individual elements for the data acquired with and without the final blow away pulse respectively. This results in a corrected fidelity of $\mathcal{F}^{\mathrm{A,cor}}_{\mathrm{state}} = 0.79(2)$ when compared to the ideal case.

Ideally the diagonal elements of the matrix should be 1 and off-diagonal elements 0 but we are limited by the efficiency of the optical state preparation pulses; optical pumping, $X_{\mathrm{local}}(\pi)$ and $X_{\mathrm{global}}(\pi)$, which are only 90 % efficient in the single qubit basis, which includes the error associated with imperfect optical pumping. This translates to the two-qubit basis as $(0.9)^2$ so that the highest achievable state preparation fidelity is 0.81. The difference of 0.02 between the expected result and the measured fidelity $\mathcal{F}^{\mathrm{A,cor}}_{\mathrm{state}}$ is most likely due to atoms being lost from the microtrap as a result of the finite temperature of the atoms during the trap drop stage.

Achieving only 90 % transfer in the single atom basis is likely due to imperfect optical pumping, to eliminate this we repeat the state matrix measurement using

method B. The uncorrected state matrix generated using method B is,

$$\mathrm{U}^{\mathrm{B}}_{\mathrm{state}} = \begin{pmatrix} 0.53(5) & 0.10(3) & 0.09(3) & 0.00(1) \\ 0.03(1) & 0.39(5) & 0.00(1) & 0.07(2) \\ 0.05(2) & 0.01(1) & 0.29(4) & 0.09(3) \\ 0.01(1) & 0.05(2) & 0.18(4) & 0.36(5) \end{pmatrix}, \tag{11.5}$$

and is shown in Fig. 11.7(b), with fidelity, $\mathcal{F}^{\mathrm{B}}_{\mathrm{state}} = 0.29(2)$. The overall retention of atoms in the two-qubit basis is lower in this case as expected since any atom not optically pumped in to qubit state $|1\rangle$ initially will be removed by the first blow away pulse. This combined with imperfect gate rotations and losses from the computational basis through decay or heating from the dipole traps contribute to the low fidelity obtained.

The fidelity is however much lower than expected and we repeat the state matrix prepared using method B without the final blow away pulse to quantify how much of the loss is due to imperfect optical pumping. The state matrix corrected for the losses associated with the initial preparation is

$$\mathrm{U}^{\mathrm{B,cor}}_{\mathrm{state}} = \begin{pmatrix} 0.83(8) & 0.15(7) & 0.14(7) & 0.00(6) \\ 0.05(7) & 0.67(8) & 0.00(7) & 0.12(7) \\ 0.09(7) & 0.02(7) & 0.56(8) & 0.17(7) \\ 0.01(7) & 0.08(7) & 0.31(8) & 0.62(8) \end{pmatrix}, \tag{11.6}$$

which has a corrected fidelity $\mathcal{F}^{\mathrm{B,cor}}_{\mathrm{state}} = 0.50(1)$. The corrected fidelity is still much lower than that achieved using method A suggesting that optical pumping is not the main source of error for this particular data.

In Fig. 11.7(b) we see that the off-diagonal elements are high which indicate that the two-qubit state preparation is not very good. The Raman laser which is used to provide the $X_{\mathrm{local}}(\pi)$ and $X_{\mathrm{global}}(\pi)$ rotations is sensitive to changes in laboratory conditions such as temperature and humidity and at the time these measurements were being performed the laboratory environment was unstable. This means that the pulse durations which correspond to $X(\pi)$ rotations were drifting throughout the day and were not always optimised. Additionally the detuning of the Raman

laser from the $|P\rangle$ is relatively small so that the transfer $|1\rangle \rightarrow |0\rangle$ may be effected by scattering. To try to circumvent problems associated with laser drifts and scattering we switched to a microwave antenna and use this to drive ground state rotations. As shown in Sec. 10.3, the microwave pulses are slower but much more stable due to using RF components.

11.4.2 State Preparation with Microwave Pulses

The state matrices generated using method A and B using a combination of microwave and optical pulses are shown in Fig. 11.8. As before, the microwave rotation is set so that a $X_{\mu\text{wave}}(\pi)$ rotation changes the qubit states from $|1\rangle \rightarrow |0\rangle$ with both atoms effected by the microwave pulse. As detailed in Sec. 10.3, we can use an AC Stark shift generated by the Qubit laser to satisfy a $Z_{\text{AC}}(\pi)$ rotation to shift the control atom out of resonance with $X_{\mu\text{wave}}(\pi)$ thus achieving single qubit state selection. Combining the $X_{\mu\text{wave}}(\pi)$ and $Z_{\text{AC}}(\pi)$ rotations we can realise each of the two-qubit states and use these to generate a state preparation matrix. Both state matrices generated using the microwave antenna to drive the qubit rotations have higher fidelities than those measured using the Raman laser, indicating that the Raman laser is indeed problematic.

We firstly measured the diagonal elements only of each state matrix prepared using methods A and B to get a comparison of the two methods, as typically the off-diagonal elements are very low. Only the diagonal elements were measured as a data run to measure the whole matrix with and without the final blow away pulse, takes over nine hours to complete. In the interest of time, measuring only the diagonal elements with each method allowed us to quickly compare the effectiveness of each method, and then measure a full state preparation matrix with method B as the fidelity was higher.

The state matrix diagonals prepared using method A, shown in Fig. 11.8(a), pro-

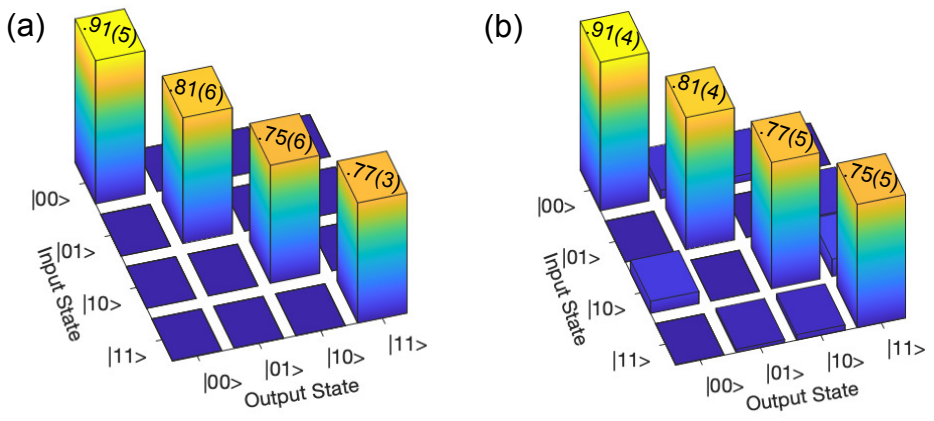

Figure 11.8: The uncorrected state matrix prepared using microwave $X_{\mu\text{wave}}(\pi)$ assisted by the $Z_{\text{AC}}(\pi)$ driven by the qubit laser for (a) method A - with optical pumping only achieving a fidelity $\mathcal{F}^{\text{A}}_{\text{state}}$= 0.81(2), and (b) with method B - optical pumping followed by a $X_{\mu\text{wave}}(\pi)$ rotation and blow away pulse with fidelity $\mathcal{F}^{\text{B}}_{\text{state}}$ =0.81(2).

duces an uncorrected state matrix with elements

$$\text{U}^{\text{A}}_{\text{state}} = \begin{pmatrix} 0.92(5) & 0.00 & 0.00 & 0.00 \\ 0.00 & 0.80(6) & 0.00 & 0.00 \\ 0.00 & 0.00 & 0.75(6) & 0.00 \\ 0.00 & 0.00 & 0.00 & 0.77(3) \end{pmatrix}, \tag{11.7}$$

where the unmeasured off-diagonal elements are set to zero. We compare the uncorrected state matrix to the ideal case and achieve a fidelity $\mathcal{F}^{\text{A}}_{\text{state}} = 0.81(2)$ which is higher than we achieved with when using optical pulses to prepare the atoms.

The measurement of the diagonal elements was repeated without the final blow away pulse and used to correct the state matrix $\text{U}^{\text{A}}_{\text{state}}$ to account for losses, giving a corrected state matrix

$$\text{U}^{\text{A,cor}}_{\text{state}} = \begin{pmatrix} 0.94(6) & 0.00 & 0.00 & 0.00 \\ 0.00 & 0.88(7) & 0.00 & 0.00 \\ 0.00 & 0.00 & 0.78(6) & 0.00 \\ 0.00 & 0.00 & 0.00 & 0.85(5) \end{pmatrix}, \tag{11.8}$$

with the off-diagonal elements again set to zero. The corrected state matrix fidelity

is $\mathcal{F}^{\mathrm{A,cor}}_{\mathrm{state}} = 0.87(2)$. Both $\mathcal{F}^{\mathrm{A}}_{\mathrm{state}}$ and $\mathcal{F}^{\mathrm{A,cor}}_{\mathrm{state}}$ may be higher in value than they would be if the entire state matrix had been measured as there will be some error associated with the off-diagonal elements which we have assumed to be zero here.

For method B, the initial $X_{\mu\mathrm{wave}}(\pi)$ rotation prior to blow away is implemented using the microwave antenna, and we measure the state matrix

$$\mathrm{U}^{\mathrm{B}}_{\mathrm{state}} = \begin{pmatrix} 0.91(4) & 0.05(3) & 0.04(2) & 0.00(1) \\ 0.00(1) & 0.81(4) & 0.00(1) & 0.04(2) \\ 0.07(3) & 0.00(1) & 0.77(5) & 0.10(4) \\ 0.00(1) & 0.02(2) & 0.03(2) & 0.75(5) \end{pmatrix}, \tag{11.9}$$

with an uncorrected fidelity $\mathcal{F}^{\mathrm{B}}_{\mathrm{state}}$=0.81(2) when overlapped with the ideal case. The data for the uncorrected state matrix is shown in Fig. 11.8(b) and we can see that the uncorrected data is better than the corrected data when using only optical pulses for preparation.

Then repeating without the final blow away pulse and applying this correction to the state matrix $\mathrm{U}^{\mathrm{B}}_{\mathrm{state}}$, we achieve a corrected state matrix

$$\mathrm{U}^{\mathrm{B,cor}}_{\mathrm{state}} = \begin{pmatrix} 1.00(6) & 0.05(5) & 0.05(5) & 0.00(6) \\ 0.00(6) & 0.92(7) & 0.00(3) & 0.05(5) \\ 0.09(5) & 0.00(6) & 0.91(7) & 0.12(6) \\ 0.00(6) & 0.02(6) & 0.04(5) & 0.82(7) \end{pmatrix}, \tag{11.10}$$

with a loss corrected fidelity $\mathcal{F}^{\mathrm{B,cor}}_{\mathrm{state}} = 0.91(1)$ showing a far superior result to any other method.

As a result, we proceed to use the method of preparing the atoms in the desired two-qubit states using optical pumping, a $X_{\mu\mathrm{wave}}(\pi)$ rotation and blow away, followed by a combination of $X_{\mu\mathrm{wave}}(\pi)$ and $Z_{\mathrm{AC}}(\pi)$ to apply the input and output state rotations when demonstrating the CNOT gate. Based on our ability to prepare the state matrix using this technique, we expect to prepare the CNOT gate with an upper bound on the achievable fidelity $\mathcal{F}_{\mathrm{CNOT}} \leq 0.91$.

11.5 Demonstration of a CNOT Gate

We demonstrate the CNOT gate based on the protocol described in Sec. 6.2 which uses the Rydberg blockade effect to condition EIT on a target atom. We demonstrate the CNOT gate by optically pumping the atoms into the qubit state $|11\rangle$, we then apply the rotation $X_{\mu\text{wave}}(\pi)$ using the microwave antenna and a blow away pulse to correct for imperfect optical pumping. We use $X_{\mu\text{wave}}(\pi)$ and $Z_{\text{AC}}(\pi)$ rotations to create each of the two-qubit basis states in turn which are applied as input before the CNOT gate pulses are applied. The pulses that make up the CNOT gate are global Rydberg light applied for 5 μs, a π-pulse applied to the control atom, an adiabatic pulse applied to the target atom for 2 μs and a second π-pulse applied to the control atom, as shown in the inset of Fig. 11.6. After the gate pulses, another sequence of $X_{\mu\text{wave}}(\pi)$ and $Z_{\text{AC}}(\pi)$ pulses are applied to cycle through the output basis states which rotate the two-qubit state to $|00\rangle$ and a final blow away pulse is applied to distinguish between the qubit states $|0\rangle$ and $|1\rangle$. By cycling through the input and output pulses we generate a CNOT gate matrix which displays the characteristic swapping of the target qubit when the control qubit is in state $|1\rangle$. As with the state matrix this allows us to measure in the basis $A_{\bullet\bullet}$ and correct for losses by measuring $B_{\bullet\bullet}$ without the final blow away pulse.

The measured CNOT gate using this preparation method is shown in Fig. 11.9(a), with matrix elements

$$\text{U}_{\text{CNOT}} = \begin{pmatrix} 0.64(5) & 0.07(3) & 0.06(3) & 0.00(1) \\ 0.06(3) & 0.65(5) & 0.04(2) & 0.01(1) \\ 0.05(2) & 0.07(3) & 0.05(2) & 0.49(6) \\ 0.00(1) & 0.06(3) & 0.42(5) & 0.10(3) \end{pmatrix}. \tag{11.11}$$

This CNOT matrix has fidelity $\mathcal{F}_{\text{CNOT}} = 0.55(2)$ when overlapped with the ideal case.

Repeating the CNOT gate matrix measurement without the final blow away pulse gives a measure of losses due to imperfect state preparation and qubits from the

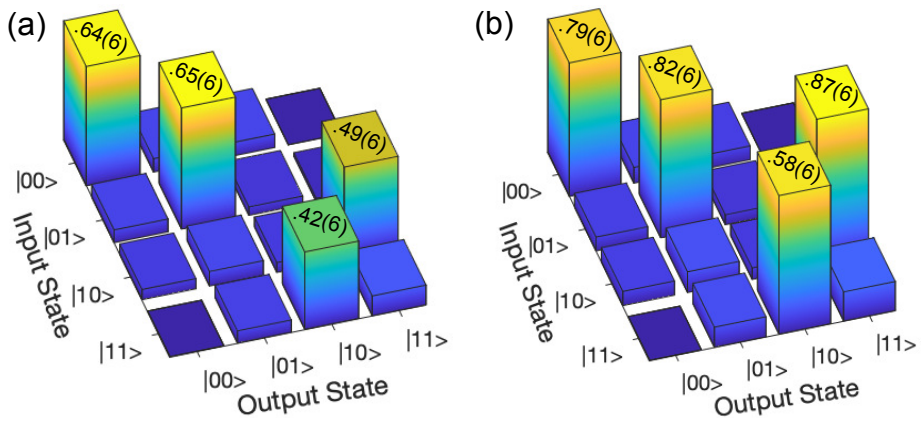

Figure 11.9: (a) The measured CNOT gate matrix uncorrected for losses from the computational basis with fidelity $\mathcal{F}_{\mathrm{CNOT}} = 0.55(2)$, (b) the corrected CNOT gate matrix with fidelity $\mathcal{F}^{\mathrm{cor}}_{\mathrm{CNOT}} = 0.84(2)$.

experiment basis. By correcting the CNOT gate matrix $\mathrm{U}_{\mathrm{CNOT}}$ for these losses we achieve a corrected gate matrix shown in Fig.11.9(b), with matrix elements

$$\mathrm{U}^{\mathrm{cor}}_{\mathrm{CNOT}} = \begin{pmatrix} 0.79(5) & 0.09(3) & 0.08(3) & 0.00(1) \\ 0.08(3) & 0.82(6) & 0.05(2) & 0.02(1) \\ 0.08(2) & 0.12(3) & 0.06(3) & 0.87(6) \\ 0.00(1) & 0.11(3) & 0.82(6) & 0.17(3) \end{pmatrix}, \tag{11.12}$$

which has fidelity $\mathcal{F}^{\mathrm{cor}}_{\mathrm{CNOT}} = 0.84(2)$ when overlapped with the ideal case.

The fidelity of the CNOT gate generated in this way is quite good but can be improved. In particular, the fidelity is 0.07 lower than predicted from the state matrix measured using the same method which placed an upper bound of $\mathcal{F}_{\mathrm{CNOT}} \leq 0.91$. Examining the individual elements of Fig. 11.9(a), we can determine where the main sources of error come from.

Considering the upper left-hand quadrant of the matrix, with input states $|01\rangle$ and $|00\rangle$, the dominant error is imperfect EIT which results in the target atom not fully following the dark state hence there is some probability that it undergoes Raman transfer. At the EIT resonance on the target atom, there is 5-10 % of the atomic population left in the qubit state $|1\rangle$ (see Fig. 11.5), leading to 5-10 % error on those gate elements. The experimental limitations on EIT are finite laser

power and fluctuations in the EIT resonance caused by frequency drifts of the ULE Rydberg laser locks, as discussed in Sec. 10.4.2.

The bottom right-hand quadrant of the gate matrix, with input states $|10\rangle$ and $|11\rangle$, are the cases where the control atom is excited to $|r\rangle$. The dominant error here is due to the loss of the control atom in the Rydberg state due to finite lifetime of the Rydberg state and dephasing effects reducing the recovery to $|1\rangle$ after the second π pulse on the control atom. As discussed in Sec. 10.4.2, the measured decay time of the Rydberg state is ~ 2.24 μs which is just greater than the 2 μs gap between the two π-pulses on the control atom. An independent measurement of the pulses on the control atom, showed that the control atom was returned to the qubit state $|1\rangle$ 80 % of the time. This means that 20 % of the control atoms decay from $|r\rangle$ before the gate operation is complete, thus potentially reducing the effectiveness of Rydberg blockade, which is crucial for controlling the CNOT operation.

By considering the errors on each of these quadrants, we can account for the reduced fidelity of the CNOT gate compared to that measured for the state matrix. If we consider the fidelity of the state matrix prepared using the same method is $\mathcal{F}_{\text{state}} = 0.91$ and compare this to the fidelity of the gate $\mathcal{F}_{\text{CNOT}} = 0.84$, then the gate operation is implemented with ~ 92 % efficiency.

11.6 Measuring Entanglement

To verify the quantum nature of the CNOT gate we generate entanglement by inputting a two-qubit mixed state and applying the CNOT gate operation on this state. In our case the target atom is prepared in $|0\rangle$ and the control atom in the superposition $(|1\rangle + |0\rangle)\sqrt{2}$ which under the CNOT gate leads to

$$\left(\frac{|1\rangle + |0\rangle}{\sqrt{2}}\right) \otimes |0\rangle \xrightarrow{\text{CNOT}} \frac{|11\rangle + |00\rangle}{\sqrt{2}}, \tag{11.13}$$

the maximally entangled Bell state $|\Phi^+\rangle$. As discussed in Sec. 2.3 the generic two-qubit density matrix is

$$\rho = \begin{pmatrix} P_{00} & a & b & c \\ a^* & P_{01} & d & f \\ b^* & d_2^* & P_{10} & g \\ c^* & f^* & g^* & P_{11} \end{pmatrix}, \tag{11.14}$$

and the Bell-state preparation fidelity for $|\Phi^+\rangle$ is

$$\mathcal{F}_{|\Phi^+\rangle} = \left\langle \Phi^+ \right| \rho \left| \Phi^+ \right\rangle = (P_{00} + P_{11})/2 + |c|. \tag{11.15}$$

This shows that to verify the preparation of an entangled state we need to measure both the diagonal populations and the off-diagonal coherence terms of the density matrix. As described in Sec. 2.3 we can measure the coherences using parity oscillations.

The parity analysis pulse that will allow us to measure the coherence term $|c|$ consists of a global phase shift $Z(\phi)$ followed by a global $X(\pi/2)$. When applying a global $X(\pi/2)$ rotation in the experiment using either Raman beams or microwaves we actually implement $R_\varphi(\pi/2)$ which introduces an additional phase factor φ. Applying these rotations to the generic density matrix given above and converting to parity as a function of phase accumulation ϕ gives a parity oscillation of the form

$$\Pi(\varphi, \phi) = 2\,\mathrm{Re}(d)\cos(\phi_d) - 2|c|\cos(2(\phi - \varphi) + \phi_c), \tag{11.16}$$

where $2\,\mathrm{Re}(d)$ is the coherence of the $|01\rangle$ and $|10\rangle$ states, ϕ_d is the phase of d, $|c|$ is the coherence of the $|00\rangle$ and $|11\rangle$ states, ϕ_c is the phase of c, ϕ is the phase accumulation prior to the $R_\varphi(\pi/2)$ pulse. This oscillation scheme is thus well suited for characterising the $|\Phi^\pm\rangle$ Bell states, with the parity only showing an oscillation at $\cos(2\phi)$ if the coherence term is non-zero, whilst for $|\Psi^\pm\rangle$ the parity simply gains a constant offset.

In practice, if the additional phase φ is not stable with respect to the other pulses and rotations in the experiment, then φ randomises over $0 - 2\pi$ for each experimental run [140], which is cycle averaged to zero over many experimental repeats.

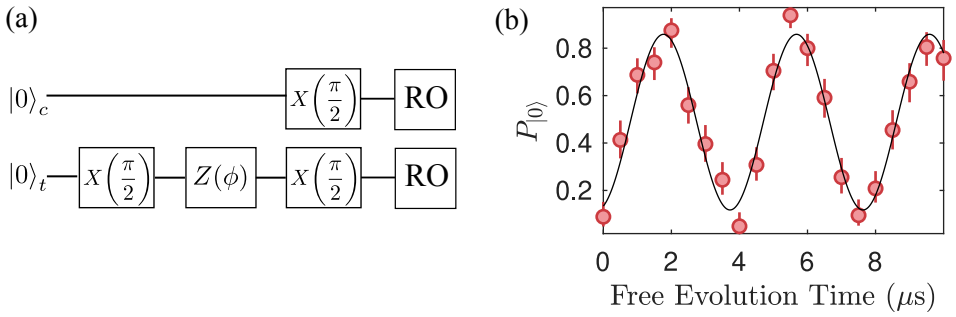

Figure 11.10: (a) Ramsey-type sequence used to prepare the control atom in the superposition $(|1\rangle + |0\rangle)/\sqrt{2}$ and the target atom in $|0\rangle$ using the local and global Raman beams to realise a phase gate $Z(\phi)$ dependent on the free evolution time between the pulses. (b) The results of the Ramsey-type sequence as the free-evolution time is scanned with phase $\phi/2\pi = 250$ kHz.

As a result of this we cannot use microwave pulses to perform either the parity analysis or the input state rotations as these are not phase-synchronous with respect to the Raman rotation pulse used during the CNOT gate. This issue arises due to the AC Stark shift term of the Raman beams with respect to the microwave pulses, leading to the microwave oscillator generating the Raman pulses operating at a detuning of 23.2 kHz from the unperturbed microwave resonance. As the experiment cycle is not triggered at integer multiples of this detuning, the effect is to introduce a random φ between Raman and microwave pulses within a given experimental run. For the data shown in Sec. 11.5 we used diagonal input states which are not sensitive to these phases.

For the Bell state preparation we therefore perform all state preparation and parity analysis using the Raman lasers which are phase-locked to the Rydberg excitation lasers and ensure all pulses are phase-synchronous when keeping the relative timing of each pulse fixed.

Generating a superposition state using the Raman laser introduces a new challenge as only the global Raman beam addresses the control atom in the experiment, which also effects the state of the target atom, and we want to prepare the atoms in different states. To achieve this we apply a Ramsey-type sequence on the target

atom using the Raman laser to apply $X_{\text{local}}(\pi/2)$ and $X_{\text{global}}(\pi/2)$ to the target atom, separated by a variable free-evolution time τ, as illustrated in Fig. 11.10(a). During the free-evolution time, the target atom accumulates a differential phase $\phi = \delta_{\text{AC}}\tau$ with respect to the Raman laser, that is caused by the AC Stark shift δ_{AC}. This results in a phase gate $Z(\phi)$ that is dependent on the free-evolution time. By scanning τ an oscillation that is sensitive to the phase of the state of the target atom is observed and is shown in Fig. 11.10(b). From the fit of this data the target atom is rotated to the qubit state $|0\rangle$ on the application of $X_{\text{global}}(\pi/2)$ when $\tau = 1.96$ μs with $\delta_{\text{AC}}/2\pi = 10.1$ kHz. This then places the control atom in the superposition $(|1\rangle + |0\rangle)\sqrt{2}$ and prepares the two-qubit input state $(|10\rangle + |00\rangle)/\sqrt{2}$ as desired.

We measure the populations and parity using method B to prepare the atoms then apply the input pulse sequence to create the mixed state $(|10\rangle + |00\rangle)/\sqrt{2}$, followed by the CNOT gate sequence to create the Bell state $|\Phi^+\rangle$. An analysis pulse is then applied on the Bell state, that depends on the measurement we want to make.

11.6.1 Population Measurement

To measure the populations we generate the Bell state $|\Phi^+\rangle$ as described above and apply an analysis pulse that allows us to measure to the populations in a basis that corresponds to $A_{\bullet\bullet}$. As illustrated in Fig. 11.11(a), to measure the population of P_{00} we apply no analysis pulse and for P_{11}, we apply $X_{\text{global}}(\pi)$ followed, in each case, with a blow away pulse to measure $A_{\bullet\bullet}$. The measurements are then repeated without the blow away pulse to measure $B_{\bullet\bullet}$ to give a correction on the total population remaining in the computational basis.

The populations P_{01} and P_{10} cannot be measured directly so we use the method employed in Ref. [30] to estimate a lower bound on these populations. The populations P_{01} and P_{10} can be expressed in terms of Eq's 11.1 and 11.2 as $P_{01} = A_{\circ\bullet} - (B_{\circ\bullet} - \sigma_{x0})$ and $P_{10} = A_{\bullet\circ} - (B_{\bullet\circ} - \sigma_{0x})$. Since we cannot independently measure each of these terms, we evaluate a lower bound for the populations given

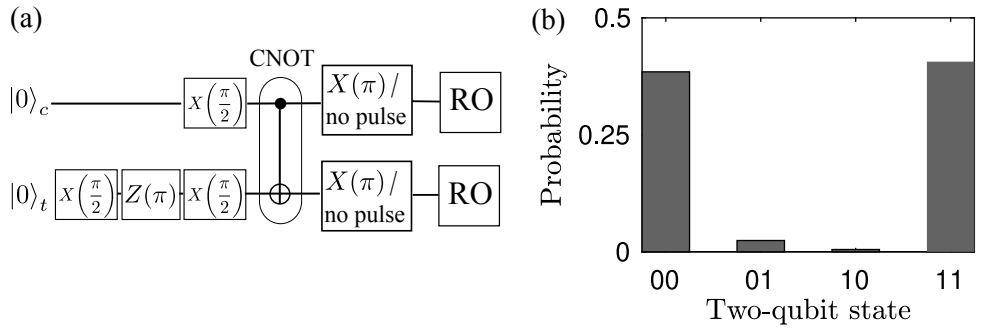

Figure 11.11: (a) Experiment sequence used to prepare and measure the Bell state $|\Phi^+\rangle$ with analysis pulses $X_{\text{global}}(\pi)$ and no pulses to measure the populations P_{00} and P_{11} respectively. (b) The populations P_{00} and P_{11} are measured directly from the data whilst P_{01} and P_{10} are estimates of the lower bound (see text for details).

by

$$P_{01} \geq A_{\bullet\circ} - B_{\bullet\circ}, \tag{11.17a}$$

$$P_{10} \geq A_{\circ\bullet} - B_{\circ\bullet}. \tag{11.17b}$$

From the measurement of the population P_{00}, we can extract the values of $A_{\bullet\circ}$, $A_{\circ\bullet}$, $B_{\bullet\circ}$, and $B_{\circ\bullet}$ to estimate a lower bound on the value of the populations P_{01} and P_{10}.

The corrected populations measured using these sequences are shown in Fig. 11.11(b) with values

$$\begin{pmatrix} P_{00} \\ P_{01} \\ P_{10} \\ P_{11} \end{pmatrix} \geq \begin{pmatrix} 0.385 \pm 0.03 \\ 0.024 \\ 0.005 \\ 0.406 \pm 0.03 \end{pmatrix}. \tag{11.18}$$

The total sum of the populations is ~ 0.82 which shows there is about 0.18 of the total population outside the computational basis. This value is consistent with the measured value of $B_{\bullet\bullet} = 0.85(3)$ when only the preparation method is applied, i.e. optical pumping, $X_{\mu\text{wave}}(\pi)$ and blow away. Additionally the measured value of $B_{\circ\circ} \approx 0.06$ for each population measurement showing that a small fraction of the atoms are lost from the microtraps which is most likely due to the finite temperature of the atoms during the trap drop.

11.6.2 Parity Oscillation

The full sequence used to measure the parity is shown in Fig. 11.12(a), where the atoms are prepared as before and the Bell state is probed using the analysis pulse $Z(\phi)$ and $X_{\text{global}}(\pi/2)$ to observe a parity oscillation. From Eq. 11.16, we can see that the parity will only oscillate when the Bell state $|\Phi^{\pm}\rangle$ is created. For the chosen analysis pulse, the parity of Bell states $|\Phi^{\pm}\rangle$ are independent of phase and have a constant value of $2\,\mathrm{Re}(d)$ and a statistical mixture shows no output oscillation under the phase accumulation.

To verify that there is no oscillation when the mixed state is used as the input, we apply the parity analysis pulses to the mixed state. The results are shown in Fig. 11.12(b) where we can see the data have no oscillation as expected for a state with no off-diagonal coherence. This means that when the Bell state $|\Phi^{+}\rangle$ is created any observed oscillation amplitude is related to the coherence term $|c|$.

The parity in the experimental basis is given by

$$\Pi = A_{\bullet\bullet} + A_{\bullet\circ} + A_{\circ\bullet} + A_{\circ\circ}, \tag{11.19}$$

and results in an oscillation with an additional offset compared to Eq. 11.16 due to losses of both atoms from the traps

$$\Pi(\phi, \varphi) = 2\,\mathrm{Re}(d)\cos(\phi_d) - |c|\cos(2(\phi - \varphi) + \phi_c) + \rho_{xx}. \tag{11.20}$$

This equation shows that the amplitude of the coherence term c is preserved even in the presence of loss and can be extracted directly from the fitted oscillation amplitude. The additional offset ρ_{xx} is equivalent to $B_{\circ\circ}$ in this basis and can be measured directly when repeating the parity measurement without the final blow away pulse.

The resulting parity oscillation is shown in Fig. 11.12(c) which is fit to Eq. 11.16, from which the coherence $|c| = 0.18(3)$ is extracted. The weighted average value of the parity measurement is 0.0055, shown as the solid grey line in Fig. 11.12(c), which has an error of 0.02 given by the standard deviation and shown by the

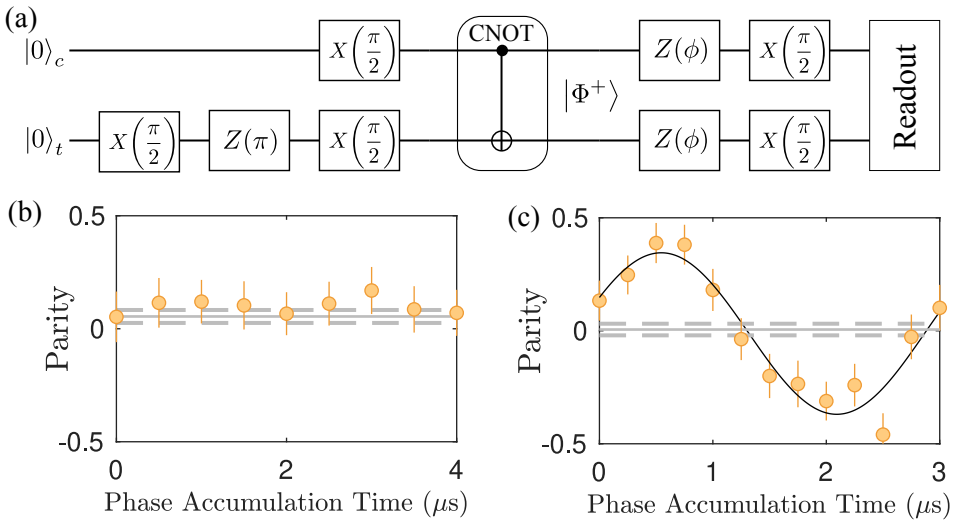

Figure 11.12: (a) Experiment sequence used to prepare and probe the Bell state $|\Phi^+\rangle$. The parity measurement is performed using the analysis pulse consisting of a global phase $Z(\phi)$ and global rotation $X(\pi/2)$. The results of the parity measurement for (b) an input mixed state $(|10\rangle + |00\rangle)/\sqrt{2}$ with no evidence of an oscillation, and (c) the Bell state $|\Phi^+\rangle$ showing a parity oscillation with respect to accumulated phase θ.

dashed grey line. This shows there is a very slight off-set to the parity result, which should be centred around zero.

From Eq. 11.20 this off-set is due to the terms $2\,\mathrm{Re}(d)\cos(\phi_d) + \rho_{xx}$, with $\rho_{xx} \equiv B_{\circ\circ} = 0.06(1)$ directly measured by repeating the parity measurement without the final blow away beam. The term $2\,\mathrm{Re}(d)\cos(\phi_d)$ is related to the unwanted Bell states $|\Psi^{\pm}\rangle$, which has a calculated value -0.055, to account for the additional off-set.

The measurement without the final blow away pulse also gives us $B_{\bullet\bullet} = 0.67(5)$, which allows us to correct for atoms lost from the computational basis. This gives a loss corrected coherence $|c|^{\mathrm{cor}} = 0.26(6)$. As stated earlier, the presence of an oscillation is a clear indicator of the coherence, which can only exist for the entangled Bell state and represents a non-factorisable coherence.

11.6.3 Bell State Fidelity

Using the uncorrected, measured values for the populations P_{00} and P_{11} and the coherence $|c|$, the measured fidelity of the Bell state is

$$\mathcal{F}_{|\Phi^+\rangle} = (P_{00} + P_{11})/2 + |c| \geq 0.44, \tag{11.21}$$

which is just below the threshold to prove entanglement. Using the loss-corrected values from each measurement gives a correct Bell state fidelity $\mathcal{F}^{\text{cor}}_{|\Phi^+\rangle} \geq 0.66$ which is above the threshold to prove entanglement. Importantly, the analysis method used to measure the parity exhibits no oscillation if an entangled state not created.

11.7 Analysis of the Losses

The method described in Sec. 11.3 enables us to perform a measurement on the atoms remaining at the end of the sequence, hence those that are in the correct measurement basis. From the measurement of $B_{\bullet\bullet}$ we get a two-atom survival of 0.67(5) which means 33 % of the atoms are lost from the microtrap from sources that do not contribute to the measurement. These losses can be evaluated by looking at the atoms separately following the discussion in Gaetan *et al.* [140].

The probability of losing an atom, independently of the other, is related to the mean value $\langle P_{c,t}(\phi)\rangle$ of the single atom survival for phase accumulation ϕ, via the relation

$$L_{c,t} = 1 - 2\langle P_{c,t}(\phi)\rangle. \tag{11.22}$$

This assumes that the mean value of the probability of an atom being measured in $|1\rangle$ at the end of the measurement is $1/2$, assuming there is no additional loss during the gate and analysis pulses. Using the mean values for each atom during the parity sequence, the loss probabilities of the control and target atoms are $L_c = 0.37(3)$ and $L_t = 0.12(4)$, respectively, which we can see are not equal.

The loss probabilities show that the control atom is more likely to be lost, which is not surprising as this atom is excited to the Rydberg state, which may decay

from $|r\rangle$ before the second π-pulse is applied or remain in the Rydberg state when the trapping light is re-applied. In either case the control atom would be lost from the trap and not contribute to the parity analysis pulses that follow the gate. The error associated with Rydberg excitation on the control atom is $\sim$ 20 %, which accounts for intensity fluctuations and spontaneous emission from $|r\rangle$, the finite temperature of the atoms during the trap drop accounts for about 5 % atom loss and the imaging accounts for $\sim$ 2 %. Imperfect optical pumping accounts for $\sim$ 10 % of the atom loss which couples to the loss channel $\{x\}$ by placing atoms in a state outside of the computational basis. In total, this accounts for the 37 % loss of the control atom.

The lower loss probability of the target atom is again unsurprising, as the target atom should always be in one of the qubit states $|1\rangle$ or $|0\rangle$ so that the main loss of this atom comes from the initial preparation pulse involving $X_{\mu\text{wave}}(\pi)$ followed by blow away which removes about $\sim$ 10 % of the atoms from the trap. This is close to the value of 12 % loss observed on the target atom.

The total probability of losing at least one of the atoms is given by

$$L_{\text{total}} = L_c + L_t - L_c L_t = 0.44(5). \tag{11.23}$$

This should be equivalent to the probability of losing an atom pair in the computational basis at the end of the sequence without the blow away pulse $1 - B_{\bullet\bullet} = 1 - 0.67(5) = 0.33$ but there is $\sim$ 10 % difference. This implies that $\sim$ 10 % of the atomic population is in the wrong state rather than lost from the trap as assumed when calculating L_{total}.

We can evaluate the contribution to loss as a result of the preparation of the wrong Bell state as this appears as an off-set to the parity oscillation. The off-set from the preparation of the wrong Bell state can be calculated from the the analysis of $A_{\bullet\bullet}$ averaged over ϕ,

$$\begin{aligned} \langle A_{\bullet\bullet}\rangle_\phi &= \frac{1}{4}\left(P_{00} + P_{01} + P_{10} + P_{11}\right) + \frac{1}{2}|d|\cos(\phi_d) \\ &= \frac{1}{4}B_{\bullet\bullet} + \frac{1}{2}|d|\cos(\phi_d), \end{aligned} \tag{11.24}$$

which gives $|d|\cos(\phi_d) = -0.05(6)$ which matches that deduced from the observed experimental off-set, showing there is a small proportion of the atoms in the wrong Bell state. This accounts for $\sim 5\%$ of the difference between the two loss calculations.

11.8 Outlook

The results presented in the preceding sections demonstrate that the novel protocol using EIT can produce a CNOT gate with $\mathcal{F}_{\text{CNOT}} \geq 0.84$, and be used to create a Bell state to prove the quantum nature of the gate with corrected fidelity $\mathcal{F} \geq 0.66$. Comparing this result to other demonstrations of a CNOT gate using Rydberg atoms, we observe that our gate has a lower fidelity than the best demonstrated which achieved $\mathcal{F}_{\text{CNOT}} \geq 0.97$ and $\mathcal{F}_{|\Phi^+\rangle} \geq 0.95$ [30]. The main limitation to the results presented in this thesis come from state preparation and laser phase noise which drastically reduce the fidelity of the gate operation being performed. If these issues were to be improved by, e.g. improving the optical pumping efficiency by replacing the Kodial glass viewport with high optical quality fused silica, we estimate that the fidelity of the CNOT gate based on EIT could achieve a similar fidelity to that presented in Ref. [30].

There are two main advantages to implementing the CNOT gate using the EIT-based protocol: firstly, multi-qubit gates can be achieved directly without the necessity to split the operations into pair-wise interactions and, secondly, the EIT based CNOT gate protocol also allows the direct implementation of a CNOT gate as most other Rydberg CNOT gates have been achieved by applying a controlled-phase (CZ) gate between two $X(\pi/2)$ rotations [17].

The next step would be to scale the experiment to more than one target atom, to measure the scalability and fidelity of the gate in this case, as it is the main advantage of implementing a CNOT gate using this protocol. To do this we would ideally introduce a third tweezer trap to the experiment, to create a three-atom

array, such that all atoms are within the Rydberg blockade radius. The use of an array is important as the atoms are confined in such a way that the interactions between target atoms can be neglected; if a target ensemble is used instead, the target-target interactions require a careful choice of Rydberg state to realise EIT on all target atoms. Due to the scalable nature of the gate protocol, the Rydberg, Qubit, Raman and microwave pulses utilised to perform the gate in Sec. 11.5 can be kept the same.

11.9 Conclusion

In this chapter we have demonstrated a new protocol for a CNOT gate based on EIT with a fidelity $\mathcal{F}_{\text{CNOT}} \geq 0.84$ and used the protocol to create a Bell state with corrected fidelity $\mathcal{F} \geq 0.66$. Whilst this fidelity is lower than expected for the fidelities obtained in simulations, these measurements represent data accumulated over 15 hours of measurements during which several critical parameters require periodic re-optimisation such as the EIT resonance which drifts as a result of the drift in the frequency of the Rydberg EOM frequency lock. The EIT resonance was particularly effected as it has a very narrow linewidth so a change of $\sim$10 kHz in the Rydberg EOM lock changes the EIT resonance. Even with interlacing recalibration, the extended measurements combined with relatively slow repetition rate ($<$1 Hz) makes these measurements challenging to improve without upgrades to the system including faster cycle times, improved optical pumping (for example by replacing the Kodial glass viewport with high optical quality fused silica) and increased Rydberg laser power.

As discussed in Sec. 10.4.2 another source of error is the laser phase noise from the ULE cavity which directly affects the Rydberg B, SolsTiS and Qubit lasers, which is then coupled into the Raman laser via the OPPL. To reduce the laser phase noise from the lock, we could use the light from the ULE cavity as a spectral filter to injection lock another laser diode as was done in [45] with great success. The

benefit of this would be to improve the decay time of the Rydberg excitations, therefore reduce the error associated with the control qubit decaying from the $|r\rangle$ before the gate sequence is complete.

Additionally, during the final parity measurements there was significant increase in mains electrical noise arising from building works in the neighbouring building that compromised laser lock stability and state preparation fidelity making these already challenging measurements substantially harder to obtain.

Part V

Conclusions and Outlook

Chapter 12

Conclusion

In this thesis we have described the experimental implementation of a CNOT gate using a new protocol that utilises EIT and Rydberg dipole blockade. To do this we have given an overview of the experimental set-up that allows us to optically trap and manipulate a pair of caesium atoms and discussed experimental upgrades that have been implemented to perform the CNOT gate.

The first experiment upgrade was to install an optical phase-lock loop between the Qubit and Raman lasers. The Qubit laser acts as a master laser to the Raman such that the Raman laser inherits the stability of the Qubit laser which is locked to a high-finesse ULE cavity. This gives both lasers an equal detuning from the intermediate state $\left|6P_{3/2}, F' = 5\right\rangle$ which is crucial for the implementation of the CNOT gate.

The second upgrade was to perform optical pumping using the D_1 line which enabled us to prepare the atoms in the state $|F = 4, m_F = 0\rangle$ with fidelity $\mathcal{F}_{\mathrm{OP}}^{D_1} = 0.986$, an improvement on that achieved using the D_2 line which has $\mathcal{F}_{\mathrm{OP}}^{D_2} = 0.966$. The main limitation we have in our ability to improve the optical pumping efficiency is the polarisation of the optical pumping beam which has a weak $\sigma^{\pm}$ component as a result of the beam passing through several windows before reaching the atoms.

The third experimental upgrade was to the Rydberg laser for excitation to the Rydberg state. A MSquared SolsTiS laser was installed to give an increase in power of light available at the atoms with more stability. We achieved Rydberg excitation using this laser with a Rabi frequency $\Omega/2\pi = 2.93$ MHz with a power of 170 mW which allowed us to perform controlled faster rotations to the Rydberg state than those achieved using the home-built laser. Due to technical issues we later reverted to using the home-built Rydberg B laser with the modification of removing an AOM to enable more power at the atoms however this removed finer control over the Rydberg pulse duration which was compensated to some degree by detuning the global Raman laser further from resonance and using mechanical shutters.

The final upgrade was the installation of a microwave antenna which allowed us to apply microwave pulses to drive rotations between the qubit states $|1\rangle \rightarrow |0\rangle$ more efficiently that using the Raman laser. Once optimised the microwave pulses reproducibly produced a transfer between the qubit states with an efficiency $>$ 95 %, an increase from the $\sim$ 85 % achieved with the Raman beams. We also optimised single-site selectivity using the Qubit laser to provide an AC Stark shift on the control atom so that the atom was not resonant with the microwaves pulse. This was also highly reproducible with an efficiency $>$ 95 %.

We optimised microwave and Raman transitions between the qubit states $|1\rangle \rightarrow |0\rangle$ for both local and global rotations, and optimised the two-photon excitation to the Rydberg state $\left|81D_{5/2}, m_j = 5/2\right\rangle$ using the Qubit and Rydberg lasers. These single qubit rotations are the basic building bocks on which the two-qubit CNOT gate can be implemented.

To perform the CNOT gate we characterised a smooth pulse with the local Raman laser so that it could drive a transition between the qubit states on a target atom. Then when the Rydberg laser was applied a dark state formed such that the target atom adiabatically followed this state, thus remaining in the qubit state it was prepared in. The effect of Rydberg blockade controlled this operation such

that when the control atom is prepared $|1\rangle$ the strong dipole interactions between the atoms shifted the target atom by an energy great enough to break the EIT condition. By preparing the control and target atoms in the states $|0\rangle$ and $|1\rangle$ in turn, we realised a CNOT gate matrix with a fidelity $\mathcal{F}_{\text{CNOT}} \geq 0.84$ when corrected for losses.

The CNOT gate protocol was then used to create the Bell state $|\Phi^+\rangle$, the quantum nature of which was measured using the parity. When correcting for losses the measured Bell state fidelity $\mathcal{F}_{|\Phi^+\rangle} \geq 0.66$ which verifies the quantum nature of the CNOT gate.

12.1 Outlook

The future direction of the project will involve a hybrid atom-superconductor system. The experiment set-up discussed throughout this thesis has been designed to allow integration of a superconducting microwave circuit into the science chamber and for a 4 K cryostat to be installed. At 4 K the quality factor, Q, of superconducting resonators is limited by quasi-particle excitation due to finite temperature effects [57], however using highly-excited Rydberg states overcomes the finite-temperature limitation to engineer long-distance entanglement that is independent of the thermal occupation and to achieve ground-state cooling of a mechanical oscillator [141].

The benefit of superconducting circuits are that they operate at a microwave frequency range that overlaps with the frequency range of highly excited Rydberg transitions [62, 142, 143]. The integration of the two technologies gives access to a range of potential applications such as quantum memories where the atomic qubit acts as a quantum memory, that can couple to the microwave mode of the superconducting circuit to realise long-distance entanglement [58, 144], ground-state cooling [145, 146] and opto-mechanical conversion of single photons from the optical to microwave domain [63, 147, 148].

In the first instance we aim to demonstrate ground-state cooling by coupling a Rydberg atom to a superconducting microwave circuit and probing the microwave field to demonstrate coherent atom-cavity dynamics [149]. This can be used to implement long-distance microwave communication which would allow coupling of distant qubits via a thermally excited waveguide by cooling the intermediate resonators which is required to perform high-fidelity state transfer [150, 151].

Bibliography

[1] *UK National Quantum Technologies Programme*, https://uknqt.ukri.org/

[2] *Quantum Computing: tomorrow's computing, today*, https://www.ibm.com/quantum-computing/

[3] F. Arute *et al.*, *Quantum supremacy using a programmable superconducting processor*, Nature **574**, 505–510 (2019)

[4] *Honeywell Quantum Solutions*, https://www.honeywell.com/us/en/company/quantum

[5] A. Browaeys and T. Lahaye, *Many-body physics with individually controlled Rydberg atoms*, Nature Phys. **16**, 132–142 (2020)

[6] Y.I. Manin, *Classical computing, quantum computing and Shor's factoring algorithm*, Asterisque **266**, 375–404 (2000), arXiv:9903008 [quant-ph]

[7] P. Benioff, *The computer as a physical system: A microscopic quantum mechanical Hamiltonian model of computers as represented by Turing machines*, J. Stat. Phys. **22**, 563–591 (1980)

[8] P. Benioff, *Quantum Mechanical Models of Turing Machines That Dissipate No Energy*, Phys. Rev. Lett. **48**, 1581–1585 (1982)

[9] D. Deutsch, *Three state quantum cryptography*, Proc. R. Soc. Lond. A **400**, 97–117 (1985)

[10] D. Deutsch, *Quantum computational networks*, Proc. R. Soc. Lond. A **425**, 73–90 (1989)

[11] L. K. Grover, *Quantum mechanics helps in searching for a needle in a haystack*, Phys. Rev. Lett. **79**, 325–328 (1997)

[12] I.L. Chuang, M.A. and Nielsen, *Contemporary Physics*, Vol. 52 (Cambridge University Press, 2000)

[13] R. P. Feynman, *Simulating physics with computers*, Int. J. Theor. Phys. **21**, 467–488 (1982)

[14] G. Semeghini *et al.*, *Probing Topological Spin Liquids on a Programmable Quantum Simulator*, 1–21(2021), arXiv:2104.04119

[15] A. Cao, Y. and Romero, J. and Aspuru-Guzik, *Potential of quantum computing for drug discovery*, IBM Journal of Research and Development **62**, 1–20 (2018)

[16] A. Acín *et al.*, *The quantum technologies roadmap: A European community view*, New J. Phys. **20**, 080201 (2018)

[17] M. Morgado and S. Whitlock, *Quantum simulation and computing with Rydberg-interacting qubits*, AVS Quantum Science **3**, 023501 (2021)

[18] D.P. DiVincenzo, *Two-bit gates are universal for quantum computation*, Phys. Rev. A **51**, 1015–1022 (1995)

[19] M. Saffman, *Quantum computing with atomic qubits and Rydberg interactions: Progress and challenges*, J. Phys. B: At. Mol. Opt. Phy **49**, 202001 (2016)

[20] L. M.K. Vandersypen *et al.*, *Experimental realization of Shor's quantum factoring algorithm using nuclear magnetic resonance*, Nature **414**, 883–887 (2001)

[21] L. M. K. Vandersypen and I.L. Chuang, *NMR techniques for quantum control and computation*, Rev. Mod. Phys. **76**, 1037–1069 (2005)

[22] C. J. Ballance *et al.*, *High-Fidelity Quantum Logic Gates Using Trapped-Ion Hyperfine Qubits*, Phys. Rev. Lett. **117**, 1–6 (2016)

[23] J. P. Gaebler *et al.*, *High-Fidelity Universal Gate Set for Be 9 + Ion Qubits*, Phys. Rev. Lett. **117**, 1–5 (2016)

[24] M. Kjaergaard *et al.*, *Superconducting Qubits: Current State of Play*, Annu. Rev. Condens. Matter Phys. **11**, 369–395 (2020)

[25] A. Aspuru-Guzik and P. Walther, *Photonic quantum simulators*, Nature Phys. **8**, 285–291 (2012)

[26] D. E. Chang, V. Vuletić, and M. D. Lukin, *Quantum nonlinear optics - Photon by photon*, Nature Photon. **8**, 685–694 (2014)

[27] I. Bloch, J. Dalibard, and S. Nascimbène, *Quantum simulations with ultracold quantum gases*, Nature Phys. **8**, 267–276 (2012)

[28] E. Altman *et al.*, *Quantum Simulators: Architectures and Opportunities*, PRX Quantum **2**, 1–19 (2021)

[29] Y. Alexeev *et al.*, *Quantum Computer Systems for Scientific Discovery*, PRX Quantum **2**, 1 (2021)

[30] H. Levine *et al.*, *Parallel Implementation of High-Fidelity Multiqubit Gates with Neutral Atoms*, Phys. Rev. Lett. **123**, 1–16 (2019)

[31] D. Jaksch *et al.*, *Fast quantum gates for neutral atoms*, Phys. Rev. Lett. **85**, 2208–2211 (2000)

[32] M. D. Lukin *et al.*, *Dipole blockade and quantum information processing in mesoscopic atomic ensembles*, Phys. Rev. Lett. **87**, 037901 (2001)

[33] C. S. Adams, J. D. Pritchard, and J. P. Shaffer, *Rydberg atom quantum technologies*, J. Phys. B: At. Mol. Opt. Phys. **53**, 012002 (2020)

[34] Y. Miroshnychenko *et al.*, *An atom-sorting machine*, Nature **442**, 151 (2006)

[35] D. Barredo *et al.*, *An atom-by-atom assembler of defect-free arbitrary two-dimensional atomic arrays*, Science **354**, 1021–1023 (2016)

[36] D. Barredo *et al.*, *Synthetic three-dimensional atomic structures assembled atom by atom*, Nature **561**, 79–82 (2018)

[37] S. Ebadi *et al.*, *Quantum Phases of Matter on a 256-Atom Programmable Quantum Simulator*, 1–20(2020), arXiv:2012.12281

[38] K.N. Schymik *et al.*, *Enhanced atom-by-atom assembly of arbitrary tweezer arrays*, Phys. Rev. A **102**, 63107 (2020)

[39] P. Scholl *et al.*, *Programmable quantum simulation of 2D antiferromagnets with hundreds of Rydberg atoms* **16**, 1–16 (2020), arXiv:2012.12268

[40] M. Saffman, T. G. Walker, and K. Mølmer, *Quantum information with Rydberg atoms*, Rev. Mod. Phys. **82**, 2313–2363 (2010)

[41] A. M. Kaufman *et al.*, *Entangling two transportable neutral atoms via local spin exchange*, Nature **527**, 208–211 (2015)

[42] T. F. Gallagher, *Rydberg atoms*, Rep. Prog. Phys. **51**, 143–188 (1988)

[43] Y. Y. Jau *et al.*, *Entangling atomic spins with a Rydberg-dressed spin-flip blockade*, Nature Phys. **12**, 71–74 (2016)

[44] Y. Zeng *et al.*, *Entangling Two Individual Atoms of Different Isotopes via Rydberg Blockade*, Phys. Rev. Lett. **119**, 1–5 (2017)

[45] H. Levine *et al.*, *High-Fidelity Control and Entanglement of Rydberg-Atom Qubits*, Phys. Rev. Lett. **121**, 1–9 (2018)

[46] T. M. Graham *et al.*, *Rydberg-Mediated Entanglement in a Two-Dimensional Neutral Atom Qubit Array*, Phys. Rev. Lett. **123**, 1–11 (2019)

[47] C. J. Picken, R. Legaie, K. McDonnell, and J. D. Pritchard, *Entanglement of neutral-atom qubits with long ground-Rydberg coherence times*, Quantum Sci. Technol. **4**, 015011 (2018)

[48] S. De Léséleuc *et al.*, *Analysis of imperfections in the coherent optical excitation of single atoms to Rydberg states*, Phys. Rev. A **97**, 1–9 (2018)

[49] I. S. Madjarov *et al.*, *High-Fidelity Control, Detection, and Entanglement of Alkaline-Earth Rydberg Atoms*(2020), arXiv:2001.04455

[50] M. Ebert, M. Kwon, T. G. Walker, and M. Saffman, *Coherence and Rydberg Blockade of Atomic Ensemble Qubits*, Phys. Rev. Lett. **115**, 1–8 (2015)

[51] I. I. Beterov *et al.*, *Coherent control of mesoscopic atomic ensembles for quantum information*, Laser Physics **24**, 074013 (2014)

[52] M. Müller *et al.*, *Mesoscopic Rydberg gate based on electromagnetically induced transparency*, Phys. Rev. Lett. **102**, 1–4 (2009)

[53] C. Maccormick *et al.*, *Supraclassical measurement using single-atom control of an atomic ensemble*, Phys. Rev. A **93**, 1–9 (2016)

[54] J. M. Auger, S. Bergamini, and D. E. Browne, *Blueprint for fault-tolerant quantum computation with Rydberg atoms*, Phys. Rev. A **96**, 1–6 (2017)

[55] J. D. Pritchard *et al.*, *Hybrid atom-photon quantum gate in a superconducting microwave resonator*, Phys. Rev. A **89**, 1–5 (2014)

[56] S. D. Hogan *et al.*, *Driving Rydberg-Rydberg transitions from a coplanar Microwave Waveguide*, Phys. Rev. Lett. **108**, 1–5 (2012)

[57] M. A. Beck *et al.*, *Optimized coplanar waveguide resonators for a superconductor-atom interface*, Appl. Phys. Lett. **109**, 092602 (2016)

[58] D. Petrosyan *et al.*, *Reversible state transfer between superconducting qubits and atomic ensembles*, Phys. Rev. A **79**, 1–4 (2009)

[59] D. Petrosyan and M. Fleischhauer, *Quantum information processing with single photons and atomic ensembles in microwave coplanar waveguide resonators*, Phys. Rev. Lett. **100**, 1–4 (2008)

[60] J. M. Raimond, M. Brune, and S. Haroche, *Colloquium: Manipulating quantum entanglement with atoms and photons in a cavity*, Rev. Mod. Phys. **73**, 565–582 (2001)

[61] S. Haroche, *Nobel Lecture: Controlling photons in a box and exploring the quantum to classical boundary*, Rev. Mod. Phys. **85**, 1083–1102 (2013)

[62] M. Kaiser *et al.*, *Cavity driven Rabi oscillations between Rydberg states of atoms trapped on a superconducting atom chip*, 1–12(2021), arXiv:2105.05188

[63] B. T. Gard, K. Jacobs, R. McDermott, and M. Saffman, *Microwave-to-optical frequency conversion using a cesium atom coupled to a superconducting resonator*, Phys. Rev. A **96**, 1–10 (2017)

[64] L. Sárkány, J. Fortágh, and D. Petrosyan, *Faithful state transfer between two-level systems via an actively cooled finite-temperature cavity*, Phys. Rev. A **97**, 1–6 (2018)

[65] P. Lambropoulos and D. Petrosyan, *Fundamentals of Quantum Optics and Quantum Information* (Springer, 2007)

[66] M. Krumm and M. P. Müller, *Quantum computation is the unique reversible circuit model for which bits are balls*, npj Quantum Inf. **5**, 7 (2019)

[67] M. Fox, *Quantum Optics* (Oxford University Press, 2006)

[68] A. Einstein, B. Podolsky, and N. Rosen, *Can quantum-mechanical description of physical reality be considered correct?*, Phys.Rev. **47**, 777–780 (1935)

[69] J. S. Bell, *on the Einstein Podolsky Rosen Paradox*, Physics **1**, 195–200 (1964)

[70] K. Vogel and H. Risken, *Determination of quasiprobability distributions in terms of probability distributions for the rotated quadrature phase*, Phys. Rev. A **40**, 2847–2849 (1989)

[71] M. Cramer *et al.*, *Efficient quantum state tomography*, Nat. Commun. **1**, 149 (2010)

[72] C. A. Sackett *et al.*, *Experimental entanglement of four particles*, Nature **404**, 256–259 (2000)

[73] A. Gaëtan *et al.*, *Observation of collective excitation of two individual atoms in the Rydberg blockade regime*, Nature Phys. **5**, 115–118 (2009)

[74] E. Urban *et al.*, *Observation of Rydberg blockade between two atoms*, Nature Phys. **5**, 110–114 (2009)

[75] C. J. Foot, *Atomic Physics* (Oxford University Press, 2005)

[76] L. Allen and J. H. Eberly, *Optical resonance and two-level atoms* (Wiley: Interscience, New York, 1975)

[77] J. Dalibard and C. Cohen-Tannoudji, *Dressed-atom approach to atomic motion in laser light: the dipole force revisited*, J. Opt. Soc. Am. B **2**, 1707 (1985)

[78] S. H. Autler and C. H. Townes, *Stark Effect in Rapidly Varying Fields*, Phys. Rev. **100**, 703 (1955)

[79] R. Loudon, *The Quantum Theory of Light*, 3rd ed. (Oxford University Press, USA, 2000)

[80] C. Cohen-Tannoudji, J. Dupont-Roc, and G. Grynberg, *Atom-Photon Interactions* (Wiley: Interscience, New York, 1998)

[81] W.H. Zurek, *Decoherence and the transition from quantum to classical - Revisited* (Birkhäuser Basel, Basel, 2007) pp. 1–31

[82] S. Kuhr *et al.*, *Analysis of dephasing mechanisms in a standing-wave dipole trap*, Phys. Rev. A **72**, 1–13 (2005)

[83] A. D. Ludlow *et al.*, *Optical atomic clocks*, Rev. Mod. Phys. **87**, 637–701 (2015)

[84] H. S. Margolis, *Optical frequency standards and clocks*, Cont. Phys. **51**, 37–58 (2010)

[85] N. F. Ramsey, *Experiments with separated oscillatory fields and hydrogen masers*, Science **248**, 1612–1619 (1990)

[86] D. A. Steck, *Quantum and Atomic Optics*, 0th ed. (2007) p. 835, `http://steck.us/teaching`

[87] E. Brion, K. Mølmer, and M. Saffman, *Quantum computing with collective ensembles of multilevel systems*, Phys. Rev. Lett. **99**, 1–4 (2007)

[88] R. Han, H.K. Ng, and B.G. Englert, *Raman transitions without adiabatic elimination: A simple and accurate treatment*, J. Mod. Opts. **60**, 255–265 (2013)

[89] D. A. Steck, *Cesium D Line Data* (2019), `http://steck.us/alkalidata`

[90] G. Lindblad, *On the generators of quantum dynamical semigroups*, Commun. Math. Phys. **48**, 119–130 (1976)

[91] M. Weissbluth, *Atoms and Molecules* (Academic Press, 1978)

[92] D. M. Brink and Satchler G. R., *Angular Momentum* (Oxford, 1962)

[93] N Bohr, *On the constitution of atoms and molecules*, Phil. Mag. **26**, 13–33 (1913)

[94] A. Browaeys and T. Lahaye, *Interacting cold Rydberg atoms: A toy many-body system*, Seminar Poincare XVII, 125–144(2013)

[95] J. D. Pritchard, *Cooperative Optical Non-Linearity in a Blockaded Rydberg Ensemble* (Springer-Verlag, Berlin, 2012)

[96] P. Goy, J. M. Raimond, G. Vitrant, and S. Haroche, *Millimeter-wave spectroscopy in cesium Rydberg states. Quantum defects, fine- and hyperfine-structure measurements*, Phys. Rev. A **26**, 2733–2742 (1982)

[97] K.-H. Weber and C.J Sansonetti, *Accurate energies of nS, nP, nD, nF, and nG levels of neutral cesium*, Phys. Rev. A **35**, 4650–4660 (1987)

[98] W. Li, I. Mourachko, M. W. Noel, and T. F. Gallagher, *Millimeter-wave spectroscopy of cold Rb Rydberg atoms in a magneto-optical trap: Quantum defects of the ns, np, and nd series*, Phys. Rev. A **67**, 7 (2003)

[99] J. Deiglmayr *et al.*, *Precision measurement of the ionization energy of Cs I*, Phys. Rev. A **93**, 1–7 (2016)

[100] I. I. Beterov, I. I. Ryabtsev, D. B. Tretyakov, and V. M. Entin, *Quasiclassical calculations of blackbody-radiation-induced depopulation rates and effective lifetimes of Rydberg nS, nP, and nD alkali-metal atoms with $n<80$*, Phys. Rev. A **79**, 1–11 (2009)

[101] N. Šibalić, J. D. Pritchard, C. S. Adams, and K. J. Weatherill, *ARC: An open-source library for calculating properties of alkali Rydberg atoms*, Computer Physics Communications **220**, 319–331 (2017)

[102] T. G. Walker and M. Saffman, *Consequences of Zeeman degeneracy for the van der Waals blockade between Rydberg atoms*, Phys. Rev. A **77**, 1–18 (2008)

[103] S. Ravets *et al.*, *Measurement of the angular dependence of the dipole-dipole interaction between two individual Rydberg atoms at a Förster resonance*, Phys. Rev. A **92**, 1–5 (2015)

[104] A. Reinhard, T. C. Liebisch, B. Knuffman, and G. Raithel, *Level shifts of rubidium Rydberg states due to binary interactions*, Phys. Rev. A **75**, 1–12 (2007)

[105] R. Heidemann *et al.*, *Evidence for coherent collective rydberg excitation in the strong blockade regime*, Phys. Rev. Lett. **99**, 1–4 (2007)

[106] T. A. Johnson *et al.*, *Rabi oscillations between ground and Rydberg States with dipole-dipole atomic interactions*, Phys. Rev. Lett. **100**, 2–5 (2008)

[107] L. Isenhower, M. Saffman, and K. Mølmer, *Multibit CkNOT quantum gates via Rydberg blockade*, Quantum Inf. Process **10**, 755–770 (2011)

[108] M. Khazali and K. Mølmer, *Fast Multiqubit Gates by Adiabatic Evolution in Interacting Excited-State Manifolds of Rydberg Atoms and Superconducting Circuits*, Phys. Rev. X **10**, 21054 (2020)

[109] M. Fleischhauer, A. Imamoglu, and J. P. Marangos, *Electromagnetically induced transparency: Optics in coherent media*, Rev. Mod. Phys. **77**, 633–673 (2005)

[110] C.J Picken, *Experimental demonstration of high-fidelity entanglement via Rydberg blockade*, Phd thesis, Univeristy of Strathclyde (2019)

[111] R. Legaie, *Coherent control of Rydberg atoms using sub-kHz linewidth excitation lasers Coherent control of Rydberg atoms using sub-kHz linewidth excitation lasers Rémy Legaie*, Ph.D. thesis, University of Strathclyde (2019)

[112] J. Dalibard and C. Cohen-Tannoudji, *Laser cooling below the Doppler limit by polarization gradients: simple theoretical models*, J. Opt. Soc. Am. B **6**, 2023 (1989)

[113] D.S. Weiss *et al.*, *Optical molasses and multilevel atoms: experiment*, J. Opt. Soc. Am. B **6**, 2072 (1989)

[114] P.D. Lett *et al.*, *Observation of atoms laser cooled below the doppler limit*, Phys. Rev. Lett. **61**, 169–172 (1988)

[115] W.D. Phillips, *Laser cooling and trapping of neutral atoms*, Rev. Mod. Phys. **70**, 721–741 (1998)

[116] C. S. Adams and E. Riis, *Laser cooling and trapping of neutral atoms*, Prog. Quant. Electron. **21**, 1–79 (1997)

[117] E. L. Raab *et al.*, *Trapping of Neutral Sodium Atoms with Radiation Pressure*, Phys. Rev. Lett. **59**, 2631–2634 (1987)

[118] A. M. Steane and C. J. Foot, *Laser cooling below the doppler limit in a magneto-optical trap*, EPL **14**, 231–236 (1991)

[119] A. S. Arnold, J. S. Wilson, and M. G. Boshier, *A simple extended-cavity diode laser*, Review of Scientific Instruments **69**, 1236–1239 (1998)

[120] C. P. Pearman *et al.*, *Polarization spectroscopy of a closed atomic transition: Applications to laser frequency locking*, J. Opt. Soc. Am. B **35**, 5141–5151 (2002)

[121] C. D. Colquhoun, A. Di Carli, S. Kuhr, and E. Haller, *Note: A simple laser shutter with protective shielding for beam powers up to 1 W*, Rev. Mod. Phys. **89**, 1–4 (2018)

[122] R. Grimm, M. Weidemuller, and Y. B. Ovchinnikov, *Optical dipole traps for neutral atoms*, Adv. At. Mol. Opt. Phys. **42**, 95–170 (2000)

[123] N. Schlosser, G. Reymond, and P. Grangier, *Collisional Blockade in Microscopic Optical Dipole Traps*, Phys. Rev. Lett. **89**, 1–4 (2002)

[124] C. J. Picken, R. Legaie, and J. D. Pritchard, *Single atom imaging with an sCMOS camera*, Appl. Phys. Lett. **111**, 164102 (2017)

[125] J. Beugnon *et al.*, *Two-dimensional transport and transfer of a single atomic qubit in optical tweezers*, Nature Physics **3**, 696–699 (2007)

[126] C. Tuchendler *et al.*, *Energy distribution and cooling of a single atom in an optical tweezer*, Phys. Rev. A **78**, 3 (2008)

[127] B. Gao, *Effects of Zeeman degeneracy on the steady-state properties of an atom interacting with a near-resonant laser field: Probe spectra*, Phys. Rev. A **49**, 3391–3395 (1994)

[128] T W Hansch and B Couillaud, *Laser frequency stabilisation by polarisation spectroscopy of a reflecting reference cavity*, Opts. Commu. **35**, 441–444 (1980)

[129] T. G. Walker and M. Saffman, *Entanglement of Two Atoms Using Rydberg Blockade*, Adv. At. Mol. Opt. Phys. **61**, 81–115 (2012)

[130] R. Legaie, C. J. Picken, and J. D. Pritchard, *Sub-kHz excitation lasers for Quantum Information Processing with Rydberg atoms*, J. Opt. Soc. Am. B **35**, 892–898 (2017)

[131] R.W.P Drever *et al.*, *Laser phase and frequency stabilization using an optical resonator.*, Appl. Phys. B **31**, 97–105 (1983)

[132] A. Hemmerich, D. H. McIntyre, C. Zimmermann, and T. W. Hänsen, *Second-harmonic generation and optical stabilization of a diode laser in an external ring resonator*, Opt. Lett. **15**, 372–374 (1990)

[133] D. Haubrich, M. Dornseifer, and R. Wyanands, *Lossless beam combiners for nearly equal laser frequencies*, Review of Scientific Instruments **71**, 338 (2000)

[134] A. Omran, *Excitation of Ultracold Rydberg Atoms in Optical Lattices*, Ph.D. thesis, Max-Planck-Institut für Quantenoptik (2011)

[135] J.G. Hinney, *A phase-locked laser system for two-photon transitions in ultracold atoms* (2013)

[136] R. Wynands and A. Nagel, *Precision spectroscopy with coherent dark states*, Appl. Phys. B **68**, 1–25 (1999)

[137] G. Santarelli, A. Clairon, S. N. Lea, and G. M. Tino, *Heterodyne optical phase-locking of extended-cavity semiconductor lasers at 9 GHz*, Opts. Commu. **104**, 339–344 (1994)

[138] G. Breit and I. I. Rabi, *Measurement of nuclear spin*, Phys. Rev. **38**, 2082–2083 (1931)

[139] T. Xia *et al.*, *Randomized benchmarking of single-qubit gates in a 2D array of neutral-atom qubits*, Phys. Rev. Lett. **114**, 1–5 (2015)

[140] A. Gaëtan *et al.*, *Analysis of the entanglement between two individual atoms using global Raman rotations*, New J. Phys **12**, 065040 (2010)

[141] F. Bariani, J. Otterbach, Huatang Tan, and P. Meystre, *Single-atom quantum control of macroscopic mechanical oscillators*, Phys. Rev. A **89**, 011801 (2014)

[142] H. Hattermann *et al.*, *Coupling ultracold atoms to a superconducting coplanar waveguide resonator*, Nat. Commun. **8**, 1–16 (2017)

[143] A. A. Morgan and S. D. Hogan, *Coupling Rydberg Atoms to Microwave Fields in a Superconducting Coplanar Waveguide Resonator*, Phys. Rev. Lett. **124**, 193604 (2020)

[144] L. Sárkány, J. Fortágh, and D. Petrosyan, *Long-range quantum gate via Rydberg states of atoms in a thermal microwave cavity*, Phys. Rev. A **92**, 030303 (2015)

[145] A. D. O'Connell *et al.*, *Quantum ground state and single-phonon control of a mechanical resonator*, Nature **464**, 697–703 (2010)

[146] J. D. Teufel *et al.*, *Sideband cooling of micromechanical motion to the quantum ground state*, Nature **475**, 359–363 (2011)

[147] R. W. Andrews *et al.*, *Bidirectional and efficient conversion between microwave and optical light*, Nature Phys. **10**, 321–326 (2014)

[148] L. Tian, *Optoelectromechanical transducer: Reversible conversion between microwave and optical photons*, Annalen der Physik **527**, 1–14 (2015)

[149] L. F. Keary and J. D. Pritchard, *Strong coupling and active cooling in a finite temperature hybrid atom-cavity system*(2021), arXiv:/arxiv.org/abs/2108.01386 [https:]

[150] Z. L Xiang, M. Zhang, L. Jiang, and P. Rabl, *Intracity quantum communication via thermal microwave networks*, PRX **7**, 011035 (2017)

[151] B. Vermersch, P. O. Guimond, H. Pichler, and P. Zoller, *Quantum State Transfer via Noisy Photonic and Phononic Waveguides*, Phys. Rev. Lett. **118**, 133601 (2017)